FEMTOSECOND LASER PULSES TO MODEL AND TREAT BRAIN DISEASES

A Dissertation

Presented to the Faculty of the Graduate School

of Cornell University

In Partial Fulfillment of the Requirements for the Degree of

Doctor of Philosophy

by

John Nguyen

August 2011

© 2011 John Nguyen

FEMTOSECOND LASER PULSES TO MODEL AND TREAT BRAIN DISEASES

John Nguyen

Thesis Advisor: Chris B. Schaffer

Cornell University 2011

Tightly focusing femtosecond laser pulses into bulk media, such as brain tissue, can generate high intensities within the focal volume. With sufficient laser energies, nonlinear absorption of femtosecond laser pulses by the media can take place. This thesis takes advantages of these nonlinear processes to image the cortical vasculature in live anesthetized rodent, and induce localized tissue disruption. We used two-photon excited fluorescence (2PEF) microscopy to image fluorescently labeled cortical vasculature *in vivo*. In this technique, two-photons are simultaneously absorbed to generate fluorescence that is localized within the focal volume, where intensity is greatest. Scanning the focus enables three-dimensional imaging since out-of-focus fluorescence is not generated. Higher-order nonlinear absorption processes that lead to plasma and cavitation bubble formation are used to induce localized tissue disruption. Together these nonlinear tools enable fine-detailed studies of the cortical vasculature and precise ablation of tissue.

To understand the potential role of small venule strokes in the development of cognitive disorders, we investigated the blood flow and vascular effects in individual vessels after inducing single venule occlusions using femtosecond laser ablation. To better understand the blood flow and metabolic responses during an epileptic seizure, we use a several optical

techniques to investigate the neurovascular and neurometabolic activity during pre-ictal and ictal phases of focal seizures. Using 2PEF microscopy we reveal the presence of vasoconstriction in arterioles surrounding the focus prior to seizure onset. The deposition of energy within the focal volume can also used to make incisions in bulk brain to disrupt tissue. Using our laser scalpel, we produced sub-surface cortical incisions and characterized the cut width and depth as a function of different laser energies. We then employed this cutting technique to determine the efficacy of sub-surface cuts in stopping seizure propagation. We then showcased a technique to produce welds at the unexposed interface between two pieces of glass and characterized their size as a function of multiple experimental parameters. Joint strength of the fused glass was tested in addition to investigating the changes in optical properties induced by the weld. Lastly, future experiments and advantages of nonlinear optical techniques are discussed.

BIOGRAPHICAL SKETCH

John was born at the Santa Barbara Cottage Hospital, in southern California. At the ripe age of two, John started his formal education at the Isla Vista Children Center, a daycare located near the University of California Santa Barbara. For three years, he battled gravity on the swings and friction on the slides, but later moved on to building impenetrable fortresses out of cardboard bricks. His one-year stint in kindergarten mainly consisted of chasing bees and staying awake during naptime. With grades one through six came John's love for basketball and growing interest in the math and sciences. His mom purchased a lot of baking soda, vinegar, and food coloring during his elementary years. John's enthusiasm for the sciences continued to peak in junior high and it became clear that he was headed for the technical field after he finished high school. At UCLA, John pursued a degree in mechanical engineering, but probably spent too much time at the beach, tailgating football games, or playing golf, instead of hitting the books and studying for his exams. Ironically, John did not see graduate school as an option after completing his degree at UCLA, but found himself working towards a master of engineering degree across the country at Cornell University one year later. It was the winter semester of 2006 when John began to work with Chris Schaffer and Nozomi Nishimura, and *most* of what happened in the next five and a half years as he worked towards his Ph.D. is documented in the following pages.

For my family.

ACKNOWLEDGEMENTS

Where do I even start? I guess with Chris. Before I get into the wonderful things about Chris, I first have to thank him for taking a chance on me. I still don't know what he saw in me as an M.Eng. student that made him offer me the coveted position as "his first" graduate student. But in all seriousness, I have been very fortunate to have Chris as my mentor over the last five years. He has provided me so many opportunities – ones that will have a lasting effect on my life. One of Chris' best attributes is his patience and understanding that he displays when working with all of his students. Prior to joining Chris' lab, I had never touched a mirror mount. Yet he spent countless hours with me in the laser room, essentially teaching me everything I now know about lasers. Chris is always willing to spend the extra time to answer my questions not only about lasers, but anything else that was on my mind. Chris placed a lot of emphasis on presentations, for which I am grateful. His method for presenting data and ideas is something that I hope to emulate as I move on with my career. Some people may not know this, but I worked with Chris and Nozomi for about eight months in 2006 before I decided to stay and work with him for the next five years – in Ithaca. It wasn't the fancy lasers that made me stay – it was the opportunity to work with Chris and Nozomi, and how well I got along with the both of them that ultimately swayed my decision. Chris' lab could have focused on the cremaster muscle, and I still would have stayed (doesn't that prove how awesome they are?). Chris, thanks for everything. I had a great time working with you and I truly appreciate everything you have done for me. Ok, enough of this – I'll talk to you later.

My guess is that incoming or current graduate students will peruse this dissertation as a scientific resource, but will also, inevitably, read this section.

So I thought it would be nice to provide some tips on how to deal with Chris. He accepts pastries and/or alcohol in exchange for time away from lab. If you find yourself in Boston, you have to come back with cannoli from Mike's Pastry. One time, I brought back only one delicious, chocolate-filled cannolo from Mike's Pastry, and proceeded to eat it in front of him during lab meeting. I believe the vile words that spewed from his mouth were, "You're a bastard." It was the most delicious and satisfying cannolo I ever had. If you find the time to go on a wine tour, not in the Finger Lakes, but in Sonoma or Napa Valley, you have to bring back a bottle of wine, and nothing cheap despite your salary. And try not to go to Vegas shortly after your wine trip. If you decide to do the AIDS ride with him around Cayuga Lake, let him and his old pal, John Parker, cross the finish line before you. If you ever find yourself driving Chris' future Corvette, Lotus, or RS4, try to minimize the redline accelerations because when it unavoidably breaks, you'll be left wondering if it was partly your fault. When Chris wears his orange polo, tell him he looks nice. If he asks you to pick him and Nozomi up from their house during the winter months – DON'T! And when he starts talking about how much weight he can lift, never make it known that you can lift more than him. If you find yourself out drinking with Chris, expect the unexpected. In fact, I encourage all of his students to take Chris out for drinks – he's fun to drink with, but just don't ask him what Nozomi sees in him. Never call him Ace or Boss, and always side with Nozomi. For the future gentlemen in the lab, join the watch club – girls love nice watches. Following these simple suggestions will get you out of the lab in 10 years. Oh yeah, eat, breath, and sleep Apple.

I want to thank my wonderful committee members, Joe Fetcho and Warren Zipfel. Despite Warren's request, I was unable to restrict my dissertation to

less than 30 pages. Warren played large part in my outreach efforts, by giving me a small amount of dye. He suggested the use of Nile Red for one of my experiments and it brought cohesiveness to my entire curriculum. The kids had a really fun time *learning* about fluorescence and its applications. I ransacked Warren's lab ~~a couple~~ many times when I couldn't find what I needed in my lab, and I want him to know that I put it back where I found it. For those who knew Warren back in his Clark Hall days, his lab was a mess. It looked like an air tank exploded in his lab. His lab space is much more organized now, but I wouldn't hesitate to place a bet that it's not going to last too much longer. I still have yet to meet another professor who tries to fix 20-year old, obsolete confocal microscopes or comes in on the weekend to do experiments. And Joe, – first, I need to thank him for raising his son, Rob, to be such an intelligent and self-motivated student. I guess in this case, the apple did fall far from the tree! I kid, I kid. Joe has helped me lose sleep by suggesting impossible experiments. Thanks Joe! Like Warren, I would ~~take~~ borrow certain items from Joe's lab, but I knew if I asked him to borrow it enough times, he would eventually give it to me. And of course, the Schaffer lab now has an electronic stimulator. Warren and Joe, I've had a blast interacting and talking with you over the years. Thank you for supporting my research and putting up with a graduate student like myself.

And now, Nozomi, aka "N^2", aka "NozomO", aka "the girl who once pondered about her cremaster muscle." Anybody familiar with our lab knows how big a role she has played in our lab. There isn't anything she can't do. Although, perhaps she could change the gas tanks by herself if she just went to the gym more often. From day one and even till now, she has been a wonderful resource for pretty much anything – surgical procedures, Matlab,

important manuscripts, imaging problems, swapping PMTs, swapping more PMTs, Jeep Wranglers, Jeep Wrangler forums, how to raise a Jeep Wrangler, and what the appropriate tire sizes are for a raised Jeep Wrangler. And dogs. Nozomi, I can't even imagine where I would be if you weren't in the lab, so thank you for everything you have taught me. You were always willing to listen to whatever stupid or mundane thing I had to say or wanted to talk about, so thank you for humoring me. But I think a small part of you will miss my random outbursts. I am extremely thankful that you and Chris have had this ongoing "collaboration" throughout my graduate work. And one last thing for future Schaffer lab members. While I will not provide an in-depth "Nozomi Guide," I will say that she will always drink "The Three Wise Men" if you order it for her at a bar. It's her favorite!

I had the opportunity to collaborate with some wonderfully smart and talented people. Costantino Iadecola, sometimes referred to as "The Godfather," provided extremely helpful and constructive feedback for the venule stroke study. I had a great time working with Ted Schwartz. He was always thinking ten experiments ahead of the current experiment – doctors. Mingrui Zhoa, a postdoc in Ted's lab, taught me all the technical aspects on how to induces seizure in our rat model and recording electrophysiology. We always seemed to get good data when he came to visit the Cornell campus. Shatha Saqqa, David Huland, and Jan Ma did some preliminary work on the brain cutting and Jillian Ferdman was a tremendous asset on the characterization study. For the glass welding studies, I had the privilege of working with Alan Arai. I always enjoyed talking to Alan about the next big thing to come from Apple.

I need to thank the other Schaffer lab members that I have spent so much

time with (in no particular order). Flor, mi hermana, I had such a good time sitting next to you these last couple of years and practicing my Spanish. You have such a big heart, and I promise I will try and find a girlfriend that won't take all my money. You still owe me lots, and lots, of food by the way. And for the last time, I'm not Mexican! Puifai, you truly are one of a kind. I enjoyed hanging out with you, drinking and making food – well you made the food, but I really enjoyed eating it. Thanks for making Ithaca a bit more exciting these last couple of years. I have some advice for you. Don't ride your bike on gravel or at night. And always be sure to check the laser schedule because everyone is responsible for his or her own experiment. Matt, thanks for all your help. I have to say, I loved your rants. They were always on point, and so very entertaining. I have some advice for you too: sand plus water does not equal a beach. Nate, I still think you cheated during those cooking contests. There is no way someone who eats boiled chicken and overcooked broccoli for lunch everyday can prepare food that delicious for our competitions. Poornima, turn off the lasers. Liz, for the right price, I will delete those photos. Chatty Cathy, in the short time that you've been in the lab, you're definitely deserving of that nickname. Undergrads, you're all over achievers and FYI, the world will not end if you get a B in a class. Ida B! Your chocolate chip cookies are delicious. Darcy, stick to three meals a day – you'll save time. Jonathan, take the cooking class that is offered at Cornell. Tilley, you're the man. Fetcho, you've done well. You get an A+ in my book, and a gold star.

Contrary to what some may believe, I did have a life outside of the lab, and there are plenty of people who can attest to that. Joey (voice), do you want the mustard on the ham or the bread? It was great living with you for these last three years. Thanks for putting up with me, my flatulence, and Dewey and

Lulu. We need to open up an Italian/Vietnamese/Mexican fusion restaurant. Tony and Donna, you've seen me at my worst. Thank you for all your love and support. I appreciate everything you two have done for me. Marty, thanks for being such a good friend, roommate, and landlord. Bruuuke, thanks for coming over to cook with Joe, and providing me with sustenance – you two as well, Casey and Jason. Johnny, the Magellan is a hit, but the Lavender Lady will always be number one. Ballyns, thanks for the culture shock. My Boston peeps – Brian, Bina, and Cory. I think it's time we drive over that watch.

I would be foolish not to thank to all my friends back at home in California for all their support. Chris (Tarui, not Schaffer), we'll be back in the same city at some point in the future. In the meantime, enjoy the snow. E, B, F, D – we will strive for 34 lbs of carne asada and tailgate UCLA games like kings. My two favorite girls in San Diego – Christen and Nikki – again, sorry about Philly. And the Torrance crew. I know my arrival was always short-noticed, but this will soon change. Jeff, my fellow Ph.D. – we need to start a clique within our clique.

Ma, Ba, James – thank you.

TABLE OF CONTENTS

LIST OF FIGURES

Chapter 3: Optical-based techniques and general procedures

Chapter 4: The impact of single venule occlusions

Chapter 5: Pre-ictal and ictal neurovascular and metabolic coupling

Chapter 6: Laser cuts in rat cortex

Chapter 7: Halting seizure propagation with a laser scalpel

Chapter 8: Glass welding

Chapter 9: GK-12 curriculum development

LIST OF TABLES

Chapter 8: Glass welding

Chapter 9: GK-12 curriculum development

LIST OF ABBREVIATIONS

AV	ascending venule
CBF	cerebral blood flow
CBV	cerebral blood volume
$CMRO_2$	cerebral metabolic rate of oxygen
DAB	3,3-diaminobenzidine
fMRI	functional magnetic resonance imaging
H&E	hematoxylin and eosin
IOS	intrinsic optical signal
LDF	laser Doppler flowmetry
LFP	local field potential
MCA	middle cerebral artery
PA	penetrating arteriole
PET	positron emission topography
RBC	red blood cell
SEM	scanning electron microscopy
SV	surface venule
2PEF	two-photon excited fluorescence microscopy

Chapter 1
Introduction

The emergence of the femtosecond laser (pulsed light as opposed to continuous wave) in the neurological field has completely changed how we see things. The femtosecond laser pulse offers a number of advantages that make it an ideal tool for studying the brain. Laser sources output light in the near-infrared spectrum, which means brain tissue is nearly transparent since absorption at these wavelengths is negligible. However, because the pulse duration is so short (~10^{-13} s), high peak intensities can be achieved within the focal volume by tightly focusing the light, which can drive nonlinear absorption of the laser energy. Furthermore, due to small focal volumes (~0.1 μm^2) and extremely short dwell times, photodamage is nonexistent, *assuming appropriate light intensities*. Taken together, tightly focusing femtosecond laser pulses enables localized deposition of laser energy into bulk material that can be confined to the focal volume. This thesis takes advantage nonlinear absorption of photons to excite fluorescent dyes and proteins and to disrupt tissue in the rodent brain.

One of the most common nonlinear imaging techniques used to study the brain is two-photon excited fluorescence (2PEF) microscopy. In this technique, the excitation of a fluorophores occurs through the simultaneous absorption of two photons. Since this nonlinear interaction occurs only at the focus where intensities are the highest, no out-of-focus fluorescence is generated, making the collection of emitted photons relatively simple and efficient. Scanning the focus can generate high-resolution, three-dimensional images of the biological sample. In the following chapters, 2PEF microscopy is used to map the cortical vasculature in rodent brain, and is also used to measure blood flow speed and

vessel diameters.

While femtosecond laser pulses allow for high-resolution imaging, they can also be used to disrupt brain tissue or melt glass. Through femtosecond laser induced damage, many photons (≥5) are absorbed by single molecules at the focus, leading to ionization of the material and generation of plasma within focal volume. This can lead to the formation of a propagating shock wave that can disrupt brain tissue or produce molten glass through heat accumulation of femtosecond pulses. In this thesis, this method used to develop a model of venules stokes, produce subsurface cuts that halt seizure propagation, or fuse two pieces of glass together.

The major theme throughout my research has been the used of nonlinear optical techniques to image and manipulate biological systems. Almost all the studies included in this dissertation involve 2PEF microscopy and tissue manipulation of the brain. While the application of this technology may seem a bit segmented (stroke and epilepsy, and glass welding), my hope is that the reader truly appreciates the powerfulness and advantages of nonlinear optical techniques, and how they enable extremely novel studies. Below is a brief description of the chapters that make up my thesis.

Chapter 2 – A prelude to small stroke and epilepsy: The two clinical realms in which this thesis ventures into are stroke and epilepsy. The purpose of this chapter is to provide a brief introduction to each disorder.

Chapter 3 – Optical-based techniques: This chapter provides an introduction to the methods and techniques used in my work and most applicable to chapters four through seven, although mechanisms related to chapter eight

are discussed. I have broken down this chapter into three main sections: fluorescence imaging, nonlinear photo-damage, and surgical and optical setup.

Fluorescence imaging. Being able to visualize biological structures that are invisible to the naked eye providing a tool that allows us to study and answer scientific inquiries. This section compares and contrasts fluorescence imaging techniques, and highlights the advantages of nonlinear imaging modalities.

Nonlinear photo-damage. Nonlinear absorption of high-energy, femtosecond lasers pulses into bulk media can result in some very interesting interactions. In this section, two modes of nonlinear photo-damage are discussed. The difference between the two techniques is largely dependent on the repetition rate of the femtosecond pulse train. In one, at low repetition rates, damage is largely due to the formation of a cavitation bubble and a subsequent shock wave that literally rips material apart. In the second regime, using high-repetition rates, damage is produced by heat accumulation from the absorption of consecutive pulses.

Surgical and optical setup. The majority of the work in this thesis involves *in vivo* studies of the brain in rodents. This section describes the general surgical procedures that were performed on rodents and the optical systems used to image and locally disrupt brain tissue.

Chapter 4 – Impact of single venule occlusions: There is a growing body of

clinical evidence supporting the idea that "silent" or small strokes play a key role in the development of cognitive disorders in the elderly. Previous work in the rodent brain has studied the effects of small stroke in the arterial system and capillary network. This chapter is an extension of that work where single downstream venules are occluded. The blood flow and vascular effects following single venule occlusion are studied and an in-depth investigation into the role of vascular topology on blood flow deficits is conducted. Results show that single venule occlusions may lead to pathological disorders that can potentially contribute to neurodegeneration.

Chapter 5 – Vascular responses associated with focal cortical seizures: Focal seizures lead to a large increase in cerebral blood flow to the epileptic focus. However, recent studies have shown decreases in cerebral blood flow in regions surrounding the focus, but reasons for this phenomenon are largely unknown. This chapter investigates the coupling between neuronal activity and metabolism. We show for the first time, that vasoconstriction of surface arterioles occurs prior to seizure onset, and would therefore imply that the decrease in flow in the surrounding regions is due to active shunting of blood.

Chapter 6 – Laser cuts in the rat cortex: Previously**,** in chapter four, energy was deposited below the brain surface through nonlinear absorption of the laser light, allowing targeted ablation of individual vessels. In this chapter, we use the laser as a light scalpel to produce sub-surface brain cuts. Cut width and maximum depth of the incisions made with different laser energies were characterized. By quantifying the laser incisions, a model was generated that allowed for predicting cut widths for a given laser energy and depth.

Chapter 7 – Halting seizure propagation: The work in the previous chapter led to the development a laser scalpel that allowed us to produce cuts below the brain surface. In this chapter we attempt to stop seizure propagation by producing cuts around the epileptic focus. In doing so, neural connections are severed disrupting processes that would otherwise assist in the propagation seizure activity. Presented here are preliminary data showing that subsurface cuts can acutely stop seizure propagation.

Chapter 8 – Glass welding: Focusing a high-repetition, femtosecond pulse train into bulk glass can lead to molten areas beyond the focal region. Translating the focus between two pieces of glasses can, in effect, produce a weld at the unexposed interface. This chapter discusses work that characterizes the weld properties produced using various laser and experimental parameters and investigates the strength of welds formed between two pieces of glass.

Chapter 9 – Grades K-12 curriculum development: I had the privilege of working Jacaranda "Jackie" Henkel, a seventh grade teacher at Eagle Hill Middle School just outside of Syracuse, over the course of the 2009-2010 academic year. This chapter presents the curriculum that she, Chris, and I developed that introduced students to fluorescence techniques and blood flow in the brain. Using a maple leaf as a model of the cerebral vasculature, the students investigated transport in a normal and injured (diseased) state to model a stroke. The perspective from which this chapter is written is much different that the previous chapter. The reader will notice that text is written in

a way to guide other teachers to replicate the curriculum activities.

Chapter 10 – Conclusions and the future… : In this chapter, I will provide some last remarks about my work and provide my perspective on the future of nonlinear optical techniques in the biomedical field and clinical setting.

Chapter 2

A prelude to small stroke and epilepsy

This chapter provides a brief introduction to the two diseases that I have mainly studied during my graduate work: stroke and epilepsy. While each chapter has its own introduction, the goal of this chapter is to provide a broad overview for readers who may be unfamiliar with the subject matters.

2.1 Stroke

Blood flow to the brain is delivered and removed by an extremely complex and intricate system of interconnected vessels. A stroke occurs when a vessel becomes obstructed or ruptures, leading to disruption of normal patterns of blood flow Unfortunately, this disease is one of the leading causes of death [1] in the United States and worldwide [2], and is a major cause of disabilities [3].

Vascular anatomy. The cerebrovasculature is an extremely vast, complex, and highly regulated system. Yet, its basic function is to serve as a conduit for blood flow that supplies nutrients and gases, and removes waste metabolites. In the human cerebrovascular system, blood from the heart is pumped through the carotid arteries (these run up along the neck) that feed the Circle of Willis (located at the base of the brain), which is comprised of a number of large interconnected arteries that branch out to deliver blood to the brain. In this thesis, all brain studies are conducted in the parietal cortex, which is largely fed by the middle cerebral artery (MCA). This large artery traverses over the brain surface, and branches off to form smaller branches called surface arterioles. These surface arterioles continue to branch off and form penetrating arterioles, vessels that radially plunge into the brain. As the vessel

dives down, capillaries branch off the arterial trunk and begin to form a dense and intricate capillary network. Downstream, the capillaries finally connect to ascending venules, i.e. a vessel that drains blood upward to the brain surface, which feed into surface venules. These vessels then drain blood into the superior sagittal sinus and eventually back to the heart.

Types of strokes. A stroke occurs when a vessel becomes blocked or ruptures, interrupting normal blood flow patterns. As a result, the regulated balance between supply and removal becomes compromised, and can lead to disastrous neurological deficits. These strokes can manifest in two distinct ways: ischemic and hemorrhagic. Ischemic strokes occur when the vessel becomes blocked, either by the stenotic growth of the vessel or by an embolus that dislodged upstream from the occlusion location. This type of stroke is the most frequent, occurring in approximately 80% of all stroke incidences. Vessels that rupture, which lead to blood perfusion into the brain tissue, are characterized as hemorrhagic strokes. In addition to disrupting flow, plasma and red blood cells perfusing into the parenchymal tissue can lead to further tissue damage. According to the World Health Organization, approximately about 5.7 million people died from stroke in 2004, and are projected to increase to almost eight million by 2030. These data are most likely associated with strokes that occur in large vessels, such as a large arteriole branch stemming from the MCA or a large draining vein.

Causes of strokes. Events that lead to stroke vary, and mainly depend on the stroke type. In ischemic stroke, vessels can become blocked by the build up of fatty deposits in the vessel lumen. An atherosclerotic plaque can develop as

the deposits accumulate, which can lead to complete stenosis of the vessel. If a vessel is injured, platelets can become activated and initiate the formation of a thrombus. An embolism can also lead to an ischemic clot. In this scenario, vascular debris such as thrombus or plaque fragments, can become dislodge and occlude a downstream vessel. Hemorrhagic stroke is mostly associated with increased intraluminal pressure. An ischemic clot can potentially lead to increased intraluminal pressure that can cause the occluded vessel to rupture, and vice versa, an injured vessel that resulted in parenchymal hemorrhaging can lead to thrombus formation and produce an ischemic clot. Futhermore, head trauma can injure vessels and lead to the formation of both types of strokes. The causes of stroke are numerous and range from congenital factors to physical trauma, and can manifest in many ways.

Stroke therapies. Despite our increased understanding of mechanisms of stroke and resulting pathophysiology, the treatment of this disease has not progressed in a similar manner. One of the most common treatments is tissue plasminogen activator (tPa), a drug that dissolves clots. This therapy is only administered to patients who have suffered from an ischemic stroke, and is most effective when given within 5 hours of the onset of symptoms. For patients that have suffered a hemorrhagic stroke, intracranial brain pressure and symptoms (headache, seizures, nausea) are monitored and if their condition worsens, surgical intervention is most likely be needed.

Small stroke versus large strokes. Unlike large strokes that present immediate clinical symptoms, small strokes are asymptomatic and have been referred to as “silent” stroke. However, there is a growing body of clinical

evidence the correlates the development cognitive disorders and the accumulation of small strokes [4-6] and have shown that these types of strokes are five times more prevalent than symptomatic strokes [7]. Despite this increased prevalence, the role of these microvascular insults in the development cognitive disorders is largely unknown.

Animal models of small stroke. As a result of these clinical studies, there has been an effort to try and understand the effects of small strokes through the use of animal models. The majority of these studies have mainly focused on the arterial side of the cerebrovasculature [3,8-10] largely neglecting the venous system, despite its clinical relevance [11]. There have been several studies that have investigated the effects of venous occlusions, but have focused mainly on large cortical veins or sinuses [12,13]. In contrast, I study occlusions of much smaller vessels. Chapter 4 investigates the effects of single venule occlusions and sheds light on their potential role in the development of neurodegenerative diseases.

2.2 Epilepsy

Epilepsy is a highly prevalent and devastating neurological disorder, which affects approximately 50 million people in the world. This condition is characterized by the onset of *recurrent* seizures, in which the neural activity of a population of cells burst in a hypersynchronous, high-frequency pattern. The following sections will review some of the more common types of epilepsies and current therapies to treat the neurological disorder.

Types of epilepsy. Epilepsy can be classified into two main groups:

generalized and partial. Generalized epilepsy involves simultaneous activity from both hemispheres, while partial, or focal, epilepsy originates from discrete locations in the brain. Partial seizures can be further broken down into two more subclasses: simple and complex, where "simple" refers to the patient maintaining consciousness and "complex" means that consciousness was impaired or lost during the seizure. The period during seizure activity is termed the "ictal" phase and the time period after the epileptic episode is referred to as the "post-ical" phase.

Simple partial seizures. This type of seizure causes motor, psychic, sensory, and autonomic symptoms without an overt loss or impairment of consciousness. For instance, if the seizure were to arise in the motor cortex responsible for hand control, the person may experience involuntary movement during the epileptic episode, which will last for a short period of time (~1-2 minutes).

Complex partial seizures. Typically, with this type of seizure, the person will abruptly switch from normal activity to behavioral arrest or a motionless stare (loss of consciousness). Involuntary lip smacking, swallowing, and small hand motions are often seen with these types of seizures. Afterwards, the person may be confused for a couple of minutes, and even up to an hour, during the post-ictal phase.

Generalized absent seizure (Petit-mal). In this type, the person loses consciousness for only a few seconds, without the loss of postural control or confusion. In addition to the momentary lapse of consciousness, patients

also exhibit subtle, bilateral movements, such as rapid eye blinking or clonic (repetitive extension/flexion) motion of the hands.

Generalized tonic-clonic (Grand mal). While this is the most common form in epileptic patients, most people associate "seizure" with this type of epilepsy because of prolonged, abrupt nature of the clinical symptoms. These seizures abruptly start with a tonic (muscle-stiffening) phase, where respiration becomes impaired and secretions begin to pool. This phase usually transitions into a clonic phase within several minutes, and eventually transitions into the end of the ictal phase, where the seizure ceases and the person begins to relax. Consciousness can be regained within a couple minutes, but can take up to several hours, and will often be impaired. People will often complain of headaches and muscle aches, and will suffer from confusion and fatigue.

Epileptogenesis. Like many other diseases, the development of epilepsy can stem from many different sources. Generalized seizures are usually associated with cellular and biochemical abnormalities, which are diffuse throughout the brain and are most likely responsible for global seizures associated with this type of epilepsy. These types of epilepsies can derive from abnormalities in neural development, which cause an imbalance in neural homeostasis or genetic disorders, such as channelopathies, can lead to hyperexcitability. For instance, mutations in Na^+ channels can allow for greater flux of the ion into the cell, resulting in increased activity, and ultimately more susceptibility to seizures [14]. Partial seizures are mostly attributed to local structural abnormalities in the brain that result from head trauma and congenital

malformations, as it can lead to long-term structural changes and remodeling in neural networks. These alterations can lower the threshold for local excitation and result in hyperexcitability [15]. Additionally, strokes and brain tumors can also lead to long-term structural changes and the development of epilepsy [16].

Treatment of epilepsy. For most patients with generalized epilepsy, antiepileptic drugs (AED) are successful in curing their epilepsy or reducing seizure frequency. However, approximately 20% of epileptic patients are medically intractable [17]. For instance, patients with focal neocortical epilepsy respond poorly to AEDs, leaving surgery as one of the few last options. While this method is usually successful in treating the condition, the procedure is not without risk, especially when the epileptic focus is near regions responsible for high-order processing. An alternative option to removing tissue is a procedure called multiple subpial transections (MST). In this procedure, a small blunt hook is used to make vertical incisions into the cortical tissue, potentially disrupting neural connections that would otherwise help the propagation of seizure activity [18]. However, this technique is a bit unsophisticated as the incisions are produced by hand. In Chapter 7, we use an optical-based technique to produce precise and controlled, sub-surface cuts in the rodent brain, in an attempt to stop seizure propagation.

References

1. Heron M, Hoyert DL, Murphy SL, Xu J, Kochanek KD, Tejada-Vera B. Deaths: final data for 2006. Natl Vital Stat Rep 2009; 57(14):1-134.
2. Murray CJL, Lopez AD. Mortality by cause for eight regions of the world: Global Burden of Disease Study. Lancet 1997; 349(9061):1269-1276.
3. Jorgensen HS, Nakayama H, Raaschou HO, Vivelarsen J, Stoier M, Olsen TS. Outcome and Time-Course of Recovery in Stroke .1. Outcome - the Copenhagen Stroke Study. Arch Phys Med Rehab 1995; 76(5):399-405.
4. Kovari E, Gold G, Herrmann FR, Canuto A, Hof PR, Michel JP, Bouras C, Giannakopoulos P. Cortical microinfarcts and demyelination significantly affect cognition in brain aging. Stroke 2004; 35(2):410-414.
5. Mok VC, Wong A, Lam WW, Fan YH, Tang WK, Kwok T, Hui AC, Wong KS. Cognitive impairment and functional outcome after stroke associated with small vessel disease. J Neurol Neurosurg Psychiatry 2004; 75(4):560-566.
6. Vermeer SE, Prins ND, den Heijer T, Hofman A, Koudstaal PJ, Breteler MM. Silent brain infarcts and the risk of dementia and cognitive decline. N Engl J Med 2003; 348(13):1215-1222.
7. Vermeer SE, Hollander M, van Dijk EJ, Hofman A, Koudstaal PJ, Breteler MM. Silent brain infarcts and white matter lesions increase stroke risk in the general population: the Rotterdam Scan Study. Stroke 2003; 34(5):1126-1129.
8. Nishimura N, Schaffer CB, Friedman B, Lyden PD, Kleinfeld D. Penetrating arterioles are a bottleneck in the perfusion of neocortex. Proc Natl Acad Sci U S A 2007; 104(1):365-370.
9. Li P, Murphy TH. Two-Photon Imaging during Prolonged Middle

Cerebral Artery Occlusion in Mice Reveals Recovery of Dendritic Structure after Reperfusion. Journal of Neuroscience 2008; 28(46):11970-11979.

10. Shih AY, Friedman B, Drew PJ, Tsai PS, Lyden PD, Kleinfeld D. Active dilation of penetrating arterioles restores red blood cell flux to penumbral neocortex after focal stroke. J Cerebr Blood F Met 2009; 29(4):738-751.
11. Black S, Gao F, Bilbao J. Understanding white matter disease: imaging-pathological correlations in vascular cognitive impairment. Stroke 2009; 40(3 Suppl):S48-52.
12. Nakase H, Kempski OS, Heimann A, Takeshima T, Tintera J. Microcirculation after cerebral venous occlusions as assessed by laser Doppler scanning. J Neurosurg 1997; 87(2):307-314.
13. Ungersbock K, Heimann A, Kempski O. Cerebral blood flow alterations in a rat model of cerebral sinus thrombosis. Stroke 1993; 24(4):563-569; discussion 569-570.
14. Chang BS, Lowenstein DH. Mechanisms of disease - Epilepsy. New Engl J Med 2003; 349(13):1257-1266.
15. Dichter MA. Emerging Concepts in the Pathogenesis of Epilepsy and Epileptogenesis. Arch Neurol-Chicago 2009; 66(4):443-447.
16. Herman ST. Epilepsy after brain insult - Targeting epileptogenesis. Neurology 2002; 59(9):S21-S26.
17. National-Institutes-of-Health Consensus Development Conference Statement - Surgery for Epilepsy March 19-21, 1990. Epilepsia 1990; 31(6):806-812.
18. Morrell F, Kanner AM, de Toledo-Morrell L, Hoeppner T, Whisler WW. Multiple subpial transection. Adv Neurol 1999; 81:259-270.

Chapter 3
Optical-based techniques and general procedures

The feasibility of my research is largely dependent on light-matter interactions. The advantages of nonlinear optical techniques allowed me to investigate the deep portions of the rodent cortex and induce damage at specific locations. This chapter first discusses light-matter interactions in the context of fluorescence imaging. More widely used fluorescence imaging techniques are discussed and as a comparison, I then present the advantages of nonlinear microscopies and how they bypass limitations associated with more traditional techniques and enable me to conduct my research. Additionally, two methods for femtosecond laser-induced damage in bulk media are introduced and compared. And lastly, the surgical procedures and general optical techniques used in the majority of my experiments (Chapters 4-7) are presented.

3.1 Laser-brain tissue interactions

The principal interactions between light and tissues are reflection, refraction, absorption and scattering, and the respective contribution of each depends on the material's optical properties. In many cases, optical properties can be simplified by analyzing major constituents of the tissue. For instance, in brain tissue, deoxyhemaglobin (HbR), oxyhemaglobin (HbO), and water are its major absorptive components [1]. HbR and HbO have relatively high absorption coefficients in the visible sprectrum, but their absorption values significantly drop in the infrared (IR) region (Figure 3.1) and thus provide an optical window between 700 – 1000 nm.

In this optical window, attenuation of focused light into brain tissue is

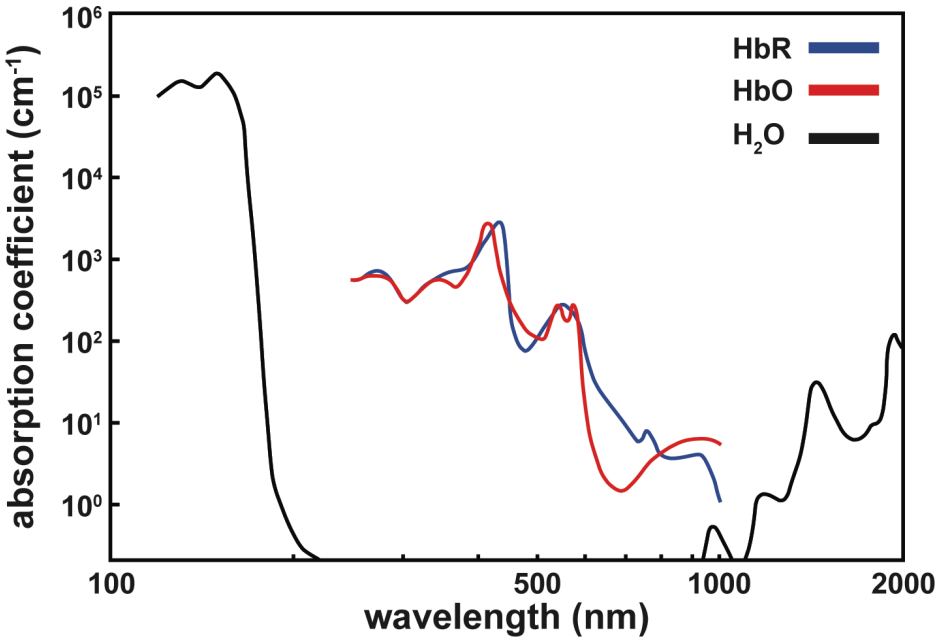

Figure 3.1 Absorption of primary light absorbers in brain tissue. Absorption coefficients for deoxyhemaglobin (HbR), oxyhemaglobin (HbO), and water as a function of light wavelength. The relatively lower absorption values between 700 and 1000 nm provide an "optical window" into the brain. Reprinted with permission from [20]

dominated by scattering and not absorption. As light travels through the tissue, photons encounter a combination of molecules and cellular structures, often deflecting from their original path. As a result, the amount of light that reaches the focus exponentially decreases with increasing depth and can be described using the following equation:

$$I(z) = I_i \exp\left(\frac{-z}{l_s}\right) \quad \text{(Eq. 3.1)}$$

where I_i is the incident laser intensity, z is the depth into the tissue, and l_s is the scattering length [2]. The scattering length describes the average distance a photon travels before experiencing another scattering event, which increases with longer wavelengths and value of 200 μm is generally used for brain tissue at 800-nm light [3]. At longer wavelengths the scattering length increases and allows for greater penetration depth into brain tissue (Figure 3.2) [4], which ultimately permits optical access to deeper structures.

3.2 Fluorescence imaging

Fluorescence imaging has become an essential tool in the biological field. Its main advantage over bright field imaging techniques is that it allows for visualization of structures that are normally invisible to the naked eye, enabling, but not limited to, studies that investigate structural morphology or localization of specific proteins. The principle reaction for fluorescence requires the absorption of a photon, or photons, by a fluorescent molecule. This absorption of energy excites the molecules to a higher energy electronic state, where it then quickly relaxes to its ground state, and in doing so, loses energy in the form of an emitted a photon. With the appropriate filters and

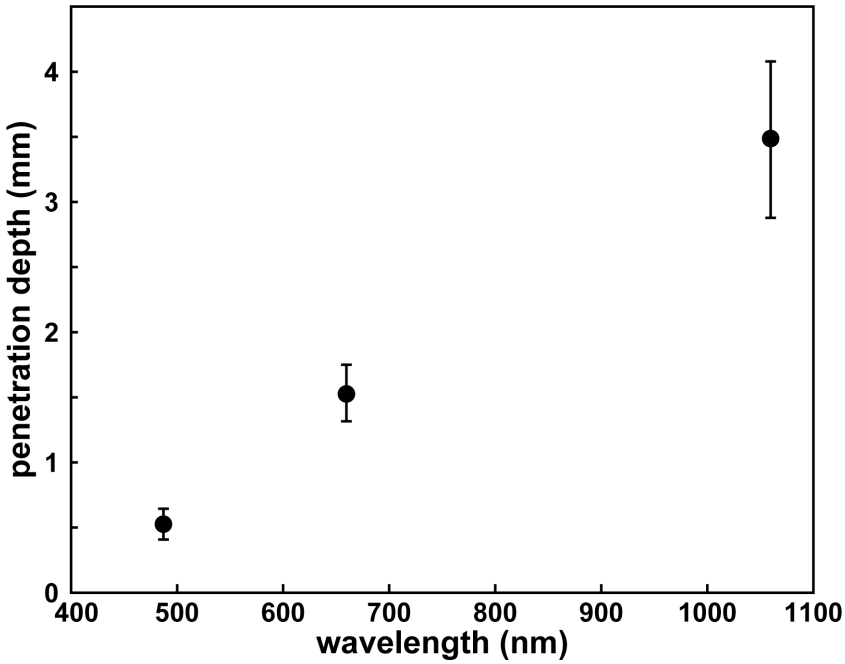

Figure 3.2 Light penetration into brain tissue. The penetration depth of 488 nm, 660 nm, and 1060 nm were measured in brain tissue (1-2 days post-mortem) from patients with ages between 67 and 84 year old. Note that the penetration depth increases with longer wavelength, which can be attributed longer scattering lengths. Error bars represent standard devation. Data taken from [4].

optical setup, emitted photons can be detected to form a fluorescent image of the sample. Standard, or the most commonly used, techniques will be discussed in the next sections, highlighting the major advantages of fluorescence imaging.

3.2.1 Exogenous labeling of biological structures

With standard fluorescence techniques, fluorescent probes with specific chemical affinities are often introduced to their sample, which are then illuminated to measure the fluorescence signals. One of the most common methods for fluorescently tagging structures is through the use of antibodies and stains. For instance, the left panel in Figure 3.3A shows a phase image of endothelial cells. In this image, cell borders can be easily discerned, but the internal structures are difficult to visualize. However, after incubating the cells with fluorescently tagged antibodies that have a chemical specificity for VE-cadherin (cell-cell adhesion proteins, red) and actin (largely responsible for cell structure, green), the structures of interest are now visible when the cells are illuminated with the appropriate light. Additionally, DAPI (4',6-diamidino-2-phenylindole) staining of the cells reveal the locations of their nuclei (Figure 3.3B). With the appropriate techniques, fluorescence imaging is a powerful tool that enables visualization of structures that are normally invisible to the eye.

3.2.2 Linear excitation modalities

After samples have been stained or tagged with the appropriate labels, the fluorescent probes must be illuminated with the appropriate light in order to excite the fluorescent molecules. In a linear process, a fluorescent molecule

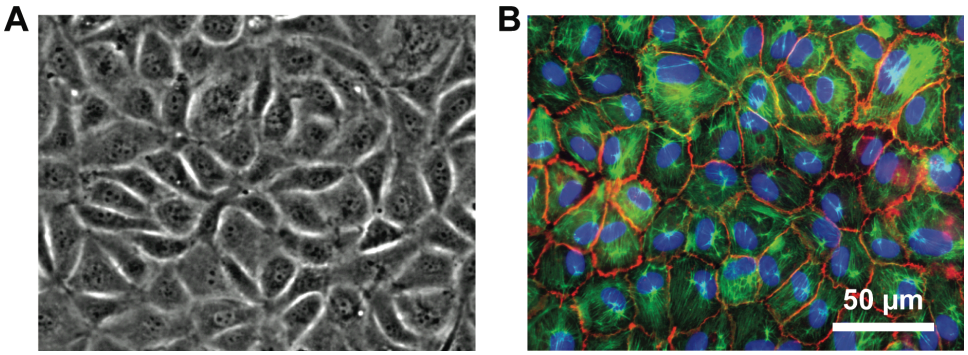

Figure 3.3 Fluorescence imaging of biological structures. A) Phase image of bovine aortic endothelial cells (BAEC). **B)** Fluorescent images of BAEC cells, stained for actin (green), VE-cadherin (red), and the nuclei (blue). Images courtesy of Joseph P. Califano.

absorbs a *single* photon and is excited to a higher energy electronic state. The molecule then relaxes (on the order of nanoseconds), and loses energy in the form of an emitted photon (Figure 3.4A). Using the same example from Figure 3.3, visualization of the three separate structures were performed using three different continuous wave light sources (UV light for DAPI, blue light for actin, green light for VE-cadherin). Most standard fluorescence microscopes are now equipped with multiple light sources and software that enables easy switching between different color illumination lights and emission filters, making multi-spectral imaging simple and very user friendly.

In this example, and most standard techniques, linear excitation works extremely well for thin samples, such as cell monolayers, but is not ideal for thicker samples, due to potential out of plane signals. Assume a fluorescently labeled sample with a structure of interest below its surface. Imaging through the sample will not only excite fluorescence at the focus, but in the tissue above due to linear absorption by the fluorophores. To bypass these problems, image sections can be acquired by using confocal microscopy. With this method, out of plane fluorescence is blocked by a pinhole, collecting light that is only generated in the focal plane. This technique works well for samples that are nearly transparent, but issues arise when samples are light-scattering, such as brain tissue [2]. Previous studies have used confocal microscopy studies to study the brain vasculature, but have been limited to depths of approximately 250 μm below the brain surface [5]. However, imaging deeper into the brain introduces a couple issues. Because the brain tissue is highly scattering, the energy at the focus decreases with increasing depth (Eq. 3.1), and in order to compensate for that loss, the laser energy needs to increase. This can potentially lead to photodamage of the tissue due to linear absorption

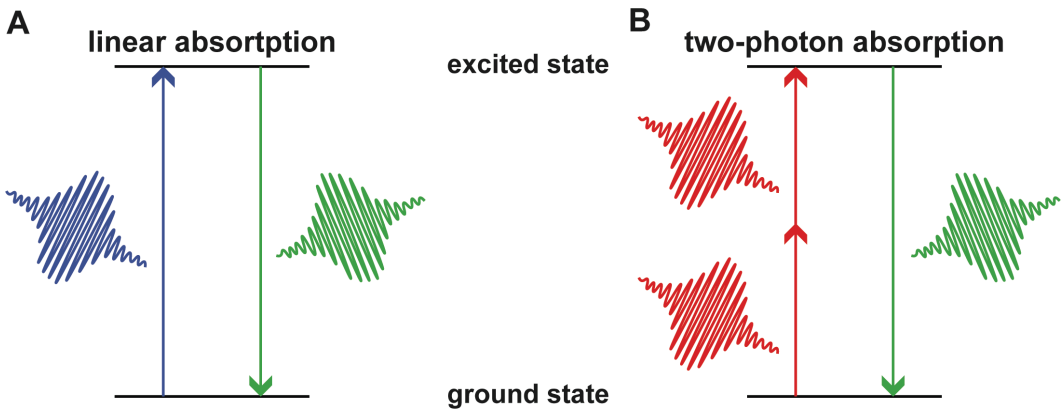

Figure 3.4 Jablonski diagrams of linear and 2PEF excitation A) Schematic of the linear excitation of a fluorescent molecule. In this case, one photon is absorbed and the fluorescent molecule is driven to an excited state. The molecule then relaxes and loses energy in the form of an emitted photon. **B)** Schematic of two-photon absorption. Unlike the linear process, the absorption of two photons must be absorbed to drive the fluorescent molecule to the excited state.

by the tissue. Additionally, light emission will also scatter back through the brain tissue and so while the confocal pinhole is designed to block out-of-plane light, photons from two different planes can scatter into similar acceptance angles to the objective, generating misleading fluorescence intensities and images. The development of nonlinear imaging techniques have helped bypass many of the limitations associated with linear excitation modalities.

3.3 Nonlinear imaging techniques

Multiphoton microscopy in academic research has been exponentially increasing since the 1990s [6]. This is primarily associated with the advent of femtosecond pulse laser systems. For all nonlinear microscopy techniques, pulsed laser systems, as opposed to continuous wave lasers, provide sufficient photon densities to drive multiphoton absorption by fluorescent molecules. Additionally, the excitation light is shifted from the visible spectrum to the near-IR region. As mentioned previously, IR light is not strongly absorbed by endogenous molecules, has longer scattering lengths, and is therefore able to penetrate deeper into tissues [7]. The signal generated is proportional to photon density to the n^{th} order process (I^n). As a result, the absorption of photons occurs only at the focus, with no signal being generated above or below the focal plane [2,3,8]. This is in direct contrast to confocal microscopy, in which absorption of the light occurs throughout the entire excitation cone. The next sections will mainly focus on the use of two-photon excited fluorescence microscopy in the rodent brain, as well as other nonlinear imaging techniques that can be easily implemented with a nonlinear optical setup.

3.3.1 Two-photon excited fluorescence

Perhaps the most widely used multiphoton imaging modality is laser scanning two-photon excited fluorescence (2PEF) microscopy, which was first demonstrated by Denk *et al*. [8] In this technique two photons are simultaneously absorbed (~0.1 fs), combining their energy to excite the fluorescent molecule to the excited state, and proceed with the normal fluorescence-emission sequence (Figure 3.4B) and is demonstrated in Figure 3.5. Because the fluorescence signal is proportional to the I^2, fluorescence is generated only at the focus, where the photon density is sufficient enough to drive nonlinear absorption of photons. Thus, 2PEF microscopy allows for the excitation of fluorescent molecules that is three dimensionally localized (Figure 3.5B). Because 2PEF uses light sources that are in the range of the "optical window," the technique is an ideal tool for *in vivo* studies. Furthermore, the developments of transgenic mice with two-photon excitable, endogenously labeled structures have really showcased the powerful of 2PEF microscopy.

3.3.2 Harmonic generation

Other commonly used nonlinear imaging techniques include second and third harmonic generation (SHG and THG), which produce detectable signals without the introduction of exogenous dyes. However, in these imaging modalities photons are not absorbed and molecules are not excited to a high-energy state. Instead, multiple photons, at frequency ω, interact with a medium to produce a photon of 2ω or 3ω, in SHG and THG, respectively (Figure 3.6) [9,10]. In SHG, photons must interact with a non-centrosymmetrical molecule in order to produce detectable radiation.

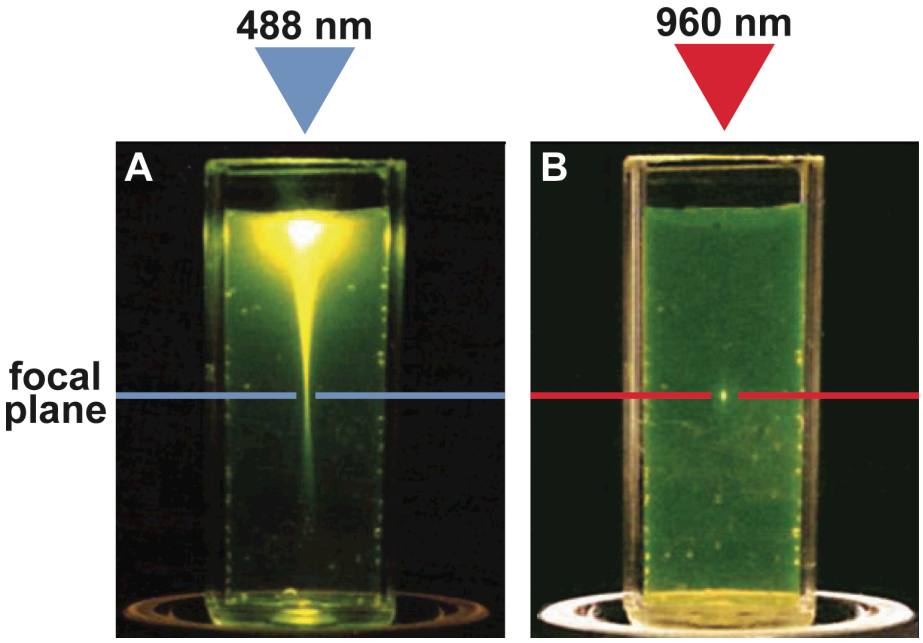

Figure 3.5 Localized excitation of fluorescein using 2PEF. A) Single photon excitation of fluorescein using 488 nm light. Note that all fluorescein within the excitation area is excited. **B)** Two-photon excitation of the same fluorescein dye using femtosecond laser pulses at 960 nm. Excitation of the dye occurs only at the focal plane. Reprinted with permission from [6].

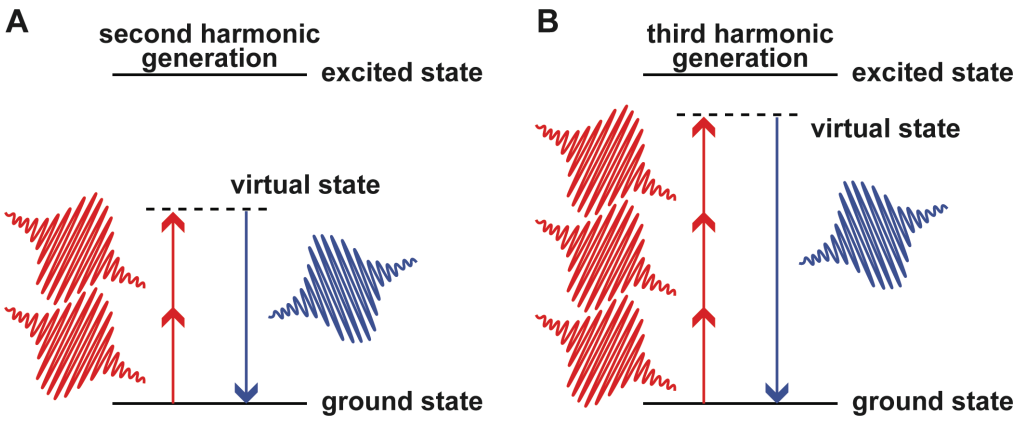

Figure 3.6 SHG and THG Jablonski diagrams. Diagrams for **A)** Second and **B)** third harmonic generation. In SHG, two photons interact with non-centrosymmetric structure to produce light at exactly half the wavelength of the excitation light. And in THG, three photons interact to produce a photon at a third of the excitation wavelength. Note that in both cases the molecule is not driven to the excited state.

Collagen is a highly non-centrosymmetrical structure, and is able to generate strong SHG signals (Figure 3.7A), and consequently has been an effective imaging tool in biomedical research [11]. Unlike SHG, THG does not require the need for a non-centrosymmetrical structure, but can generate third harmonic signals at interfaces (Figure 3.7B) [10]. In both imaging modalities, phase matching must be preserved and therefore, signal is generated in the forward direction, as opposed to isotropic emission associated with standard fluorescence techniques. Therefore, epidetection of harmonic generation is from back-scattered photons. Like other nonlinear imaging methods, these interactions only occur at the focus, where the intensity is strong enough to drive nonlinear interactions. With the appropriate optical filters and light sources, SHG and THG can be easily implemented into pre-existing nonlinear microscopes.

3.4 Femtosecond laser induced damage in bulk media

In the previous sections, the use of femtosecond laser pulses with wavelengths in the near-IR regime, provides a novel imaging tool. At these wavelengths tissue is nearly transparent, and linear absorption of light is negligible. However, with sufficient intensities photons can be nonlinearly absorbed to produce fluorescence or harmonic generation, without introducing any damage to the tissue. For instance, assume a transparent material (no scattering for simplicity) with incident power of 1 mW, a high approximation. The repetition rate for most Ti:sapphire lasers is approximately 80 MHz, which leads to 0.0125 nJ per pulse. With a NA of 0.95 and 800-nm light, the cross-sectional area is approximately 0.1 μm^2. Thus, the peak intensity ($E_{pulse}/\tau A_{cross\text{-}section}$) is on the order of 10^{11} W/cm^2. For optical

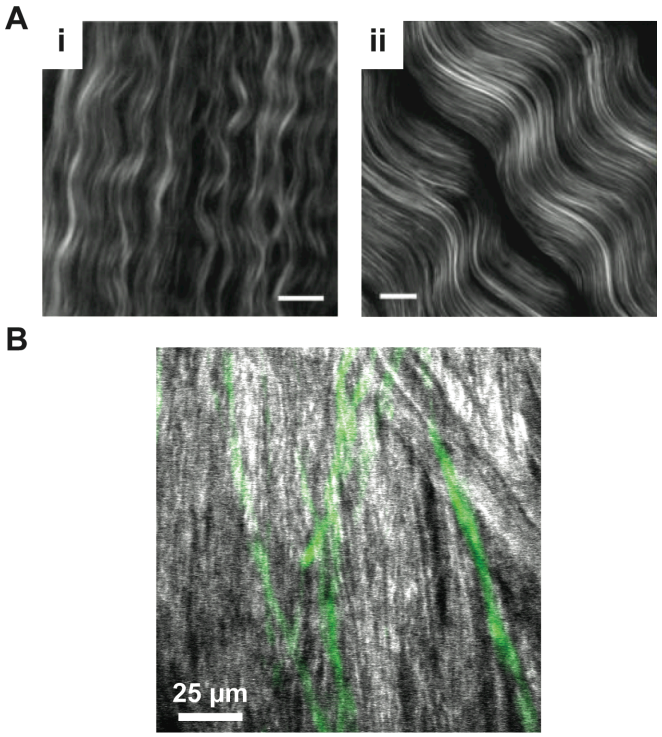

Figure 3.7 Imaging collagen and myelin using harmonic generation. A) Second harmonic generation images of collagen fibrils at i) two days and ii) 19 days taken from a rat tail. **B)** *In vivo* third harmonic generation of the myelin sheath surrounding axons in the spinal cord. THG signal surrounds the small subset of axons that expresses fluorescent proteins (green). Panel A is reprinted with permission from [11], and panel B was generously provided by Matthew J. Farrar.

breakdown of water, a main constituent of biological tissues, including brain, peaks intensities must reach values on the order of 10^{13} W/cm^2 [12]. This calculation shows that the pulse energies from the imaging lasers are not reaching breakdown thresholds that would cause optical breakdown of the tissue. However, regenerative amplifiers are able to produce similar average output powers, but with pulse rates of 1 kHz, and assuming similar incident energy, the peak intensities skyrocket to 10^{15} W/cm^2, far exceeding the threshold for optical breakdown. Because this process is governed by nonlinear absorption, the induced damage is locally confined. The following two sections will discuss different mechanisms for femtosecond laser-based induced damage in bulk media.

3.4.1. Plasma-mediated ablation

Pulse trains of amplified femtosecond laser pulses usually have a repetition rate on the order of a kilohertz. However, the average output power of these kilohertz pulse trains is similar to other femtosecond oscillators used for imaging, but the pulse energy is significantly higher given the that its repetition rate is four orders of magnitude smaller. Tightly focusing high-energy femtosecond laser pulses can generate plasma within the focal volume, inducing damage in the media through ionization, and secondary mechanical effects [12,13]. The production of plasma is dependent on a cascade of events, mainly photoionization, impact and avalanche ionization.

In photoionization, an electron is excited from its valence band to the conduction band through direct interactions with the laser field. The mechanism by which photoionization occurs depends on laser frequency and intensity, and can be described by two main regimes: tunneling and

multiphoton ionization [14]. Figure 3.8 shows schematics of these processes. In tunneling, the electron is accelerated across the energy band gap, a process usually associated with strong electric fields and low laser frequencies. With high laser frequencies, the electron is ionized into the conduction band through the absorption of multiple photons, hence multiphoton ionization. The transition between the two processes can be described by the Keldysh parameter [15]

$$\gamma = \frac{\omega}{e}\left(\frac{mcn\varepsilon_o E_g}{I}\right)^{1/2} \qquad \text{(Eq. 3.2)}$$

where m and e are the reduced mass and charge of the electron, ω is the laser frequency, c is the speed of light, ε_o is the free space permittivity, n is the refractive index of the material, and I is the laser intensity at the focus. For Keldysh values less than 1.5, tunneling is responsible for launching the electron through the band gap, whereas values greater than 1.5 lead to mulitphoton ionization. For intermediate values ~1.5, the mechanism is an interplay between tunneling and multiphoton ionization. For studies in this thesis, we use the band gap of water, 6.5 eV, a light wavelength of 800 nm, and the breakdown treshold of 10^{13} W/cm^2, which yields a Keldysh parameter of approximately 1.5.

Once the electron is launched into the conduction band, it is able to linearly absorb more photons in order to increase its kinetic energy to initiate impact ionization. When the photon has reached the critical energy, it can then collide with another electron sitting in the valence band, launching itself and the bound electron into the conduction band. The critical energy obtained through absorption must at least surpass the ionization potential of the bound electron

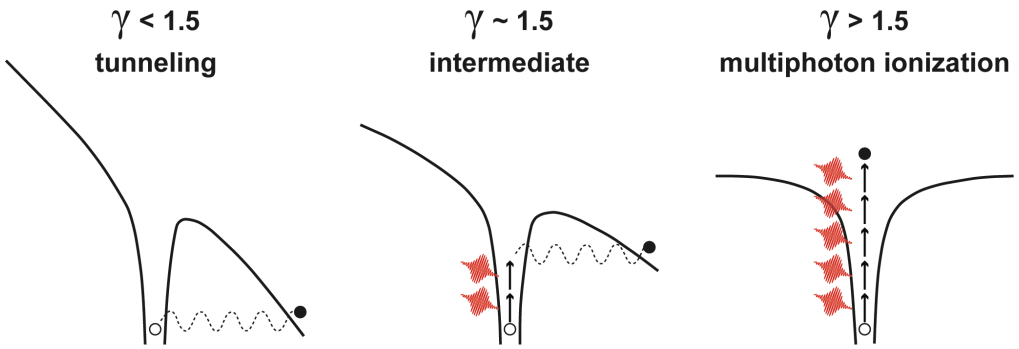

Figure 3.8 Modes of photoionization. Schematics of the photoionization of an electron in an atomic energy potential, for difference Keldysh values. For the same material, tunneling is usually associated with strong laser fields and low laser frequencies, whereas muliphoton ionization is usually driven by high frequency laser light. Reprinted with permission from [14].

to ionize both, the impacting and impacted, electrons into the conduction bands, in order to conserve energy. The ionized electrons in the conduction band are now able to absorb more photons such that impact ionization can continue to produce free electrons. This process then leads to avalanche ionization, where the doubling growth of the free electrons reaches a critical density, 10^{21} electrons/cm^{-3}, to form plasma. This interplay between photoionization, impact ionization, and avalanche ionization is shown in Figure 3.9. At increased electron densities, and therefore increased plasma formation, other disruptive mechanisms begin to form. If intensities at the focus significantly exceed the threshold for optical breakdown, a shock wave and the formation of a cavitation bubble can lead to damage beyond the focal volume, which some distinguish as photodisruption. Figure 3.10 shows an image sequence of the breakdown of water induced by a high-energy femtosecond pulse train. Shortly after absorption of the laser pulse, the plasma cloud is visible (25 ps) and continues to grow (400 ps) [13]. Deposition of laser pulses with such intensities produces extremely large stresses, which leads to the formation of shock wave and cavitation bubble. The shock wave can be seen to start separating from the plasma cloud (1.6 ns) and continues to propagate away as a cavitation bubble (6.4 ns). In brain, this shock wave can rip the tissue apart, provided the induced stress from the propagating wave is greater than the tensile strength of the tissue.

3.4.2. Thermal accumulation

With photodisruption, the secondary mechanical effects that propagate from the focal volume cause much of the induced damage. However, with high-repeption rates on the order of MHz, the photo-damage is largely

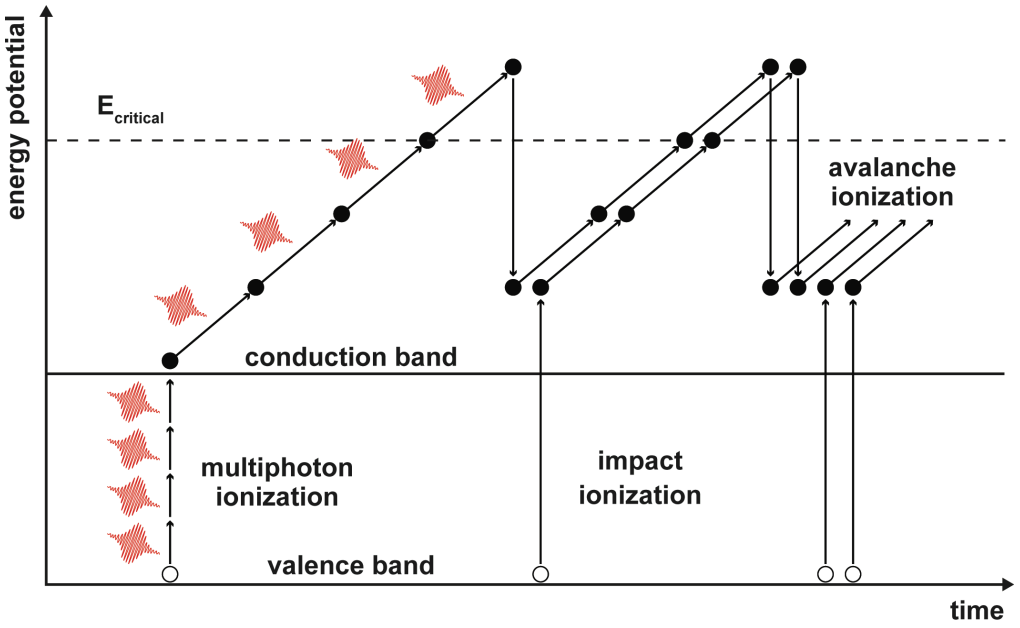

Figure 3.9 Avalanche ionization and plasma formation. A seed electron is launched into the conduction band through photoionization, where it can absorb more photons to reach the critical energy necessary for impact ionization. In this process, the seed electron collides with an electron in the valence band, launching both into the conduction band where they can absorb more photons. The doubling of free electron after each impact leads to avalanche ionization. A critical electron density is then reached leading to the plasma formation and photodisruption. Reprinted with permission from [12].

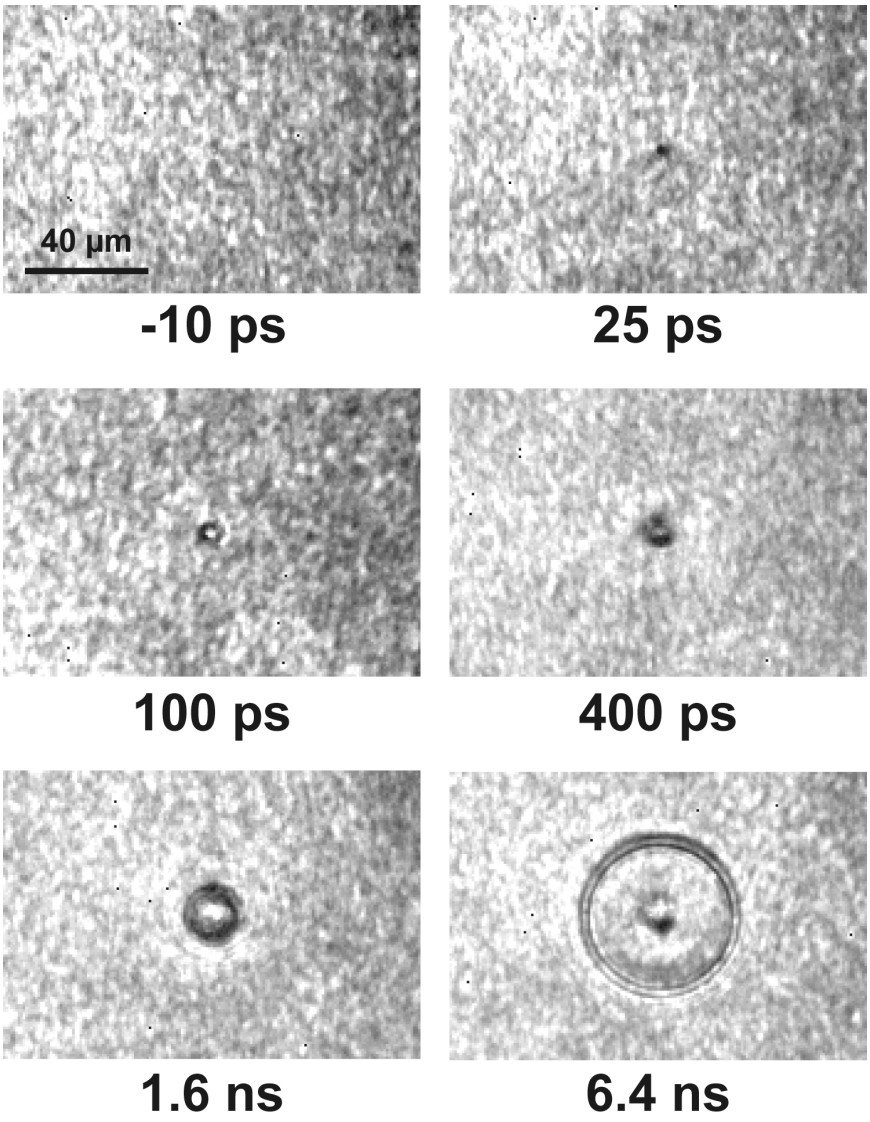

Figure 3.10 Femtosecond laser-induced breakdown of water. A sequence of images showing breakdown of water induced by a single femtosecond laser pulse. Reprinted with permission from [13].

attributed to thermal accumulation of consecutive pulses. At high repetition rates, the heat generated from the initial femtosecond laser pulse cannot diffuse out of the focal volume (~μs) before the next pulse is deposited (~ns) [12]. Therefore, the accumulation of femtosecond laser pulses acts as a point source of heat. Figure 3.11 shows femtosecond laser, induced damage in glass and note that its area increases with greater number of deposited pulses [16].

3.5 General experimental and optical setup

The setup procedures for most of the experiments in chapters three through seven are very similar. All experiments were conducted on rats, except for one, in which a transgenic mouse was used. Briefly, for all experiments, craniotomies were performed to gain optical access to the brain. We used fluorescent dyes to label the vasculature and used 2PEF microscopy to image the vessels. High-energy femtosecond laser pulses were then used to either induce strokes or cut brain tissue, depending on the experiment. Specific details for each experiment are presented in their respective chapter. The following sections provide more details about the optical systems that were used for all applicable studies.

3.5.1 Surgical procedures

All rats were anesthetized with urethane (1.5 g/kg rat) and glycopyrolate (0.5 mg/kg rat) was administered intramuscularly to help prevent secretions. Body temperature was kept at 37^{o} C with a heating blanket controlled by a rectal thermometer (50-7053; Harvard Apparatus). Heart rate and arterial oxygen saturation were monitored with a pulse oximeter (MouseOx; Starr Life Sciences Corp.) clipped to the rat's hind paw. Hydration was maintained with

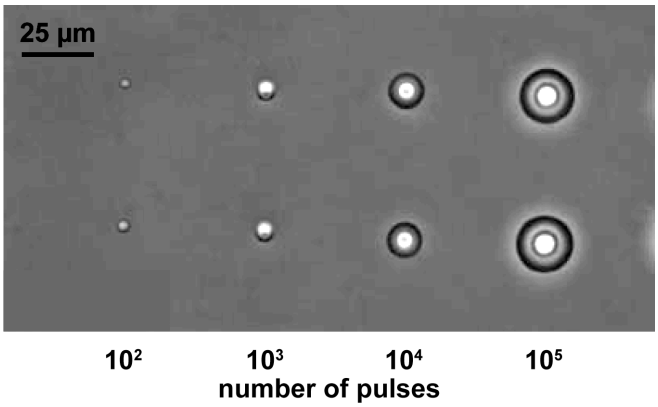

Figure 3.11 Heat accumulation of femtosecond laser pulses in glass. Image of laser-induced damage through the accumulation of 5-nJ, 30 fs laser pulses from a 25 MHz pulse train, tightly focused with a 1.4 NA objective. Note that the damage area becomes larger with an increasing number of pulses. Reprinted with permission from [16].

hourly subcutaneous injections of 5% glucose (wt/vol) in saline (1 ml/kg rat). Physiological parameters were manually recorded every 20 minutes to ensure the physiological state of the rat was stable.

Craniotomies were performed to gain optical access to the brain. A subcutaneous injection 0.1 ml of bupivicaine (0.125% wt/vol in deionized water) was administered to reduce pain at the incision site. A ~3x6-mm craniotomy was made over the parietal cortex and the dura was removed. The brain was then covered in 1.5% agarose (A9793; Sigma) in artificial cerebral spinal fluid [17], and an 8-mm diameter No. 1.5 glass coverslip (50201; World Precision Instruments) was placed over the craniotomy and sealed with dental cement (Co-Oral-Ite Dental Mfg Co.). To visualize the vasculature using 2PEF microscopy, we intravenously injected ~0.3 ml of 5% (wt/vol) 2-MDa fluorescein-conjugated dextran (FD2000S; Sigma) in saline. All animal care and experimental procedures were approved the Institutional Animal Care and Use Committee of Cornell University.

3.5.2 Two-photon microscopy of the brain

In vivo images were obtained with a custom designed 2PEF microscope that used a low-energy, 100-fs, 800-nm, 76-MHz repetition rate pulse train generated by a Ti:sapphire oscillator (Mira-HP; Coherent) that was pumped by a continuous wave diode-pumped solid state laser (Verdi-V18; Coherent). Data acquisition and laser scanning was controlled using MPSCOPE software [18]. Fluorescence was detected through an interference filter centered at 517 nm with a 65-nm bandpass. A 0.28 numerical aperture (NA), 4X-maginfication, air objective (Olympus) was used to obtain images of the entire cranial window. A 0.95 NA, 20X-magnification, water-immersion objective

(Olympus) was used for high-resolution imaging, measurements of vessel diameter and blood flow speed, vessel occlusion, and cutting brain tissue.

3.5.3 Ablation laser

Tissues were irradiated with a 50-fs, 800-nm, 1-kHz pulse train produced by a Ti:sapphire regenerative amplifier (Legend 1k USP; Coherent) pumped by a Q-switched laser (Evolution 15; Coherent) and seeded by a Ti:sapphire oscillator (Chinhook Ti:sapphire laser; Kapteyn-Murnane Laboratories Inc., pumped by Verdi-V6; Coherent, Inc.).

3.5.4 Custom-built microscope

Both the 2PEF imaging and the ablation laser beams were combined along the same beam path using a polarizer beam splitter within the custom 2PEF microscope and focused to the same plane, allowing for simultaneous imaging and ablation (Figure 3.12) [19]. Pulse energy for ablation was varied with neutral density filters and the number of pulses focused in the vessel lumen was controlled using a mechanical shutter with a 2-ms minimum opening time (VMM-D4; Uniblitz).

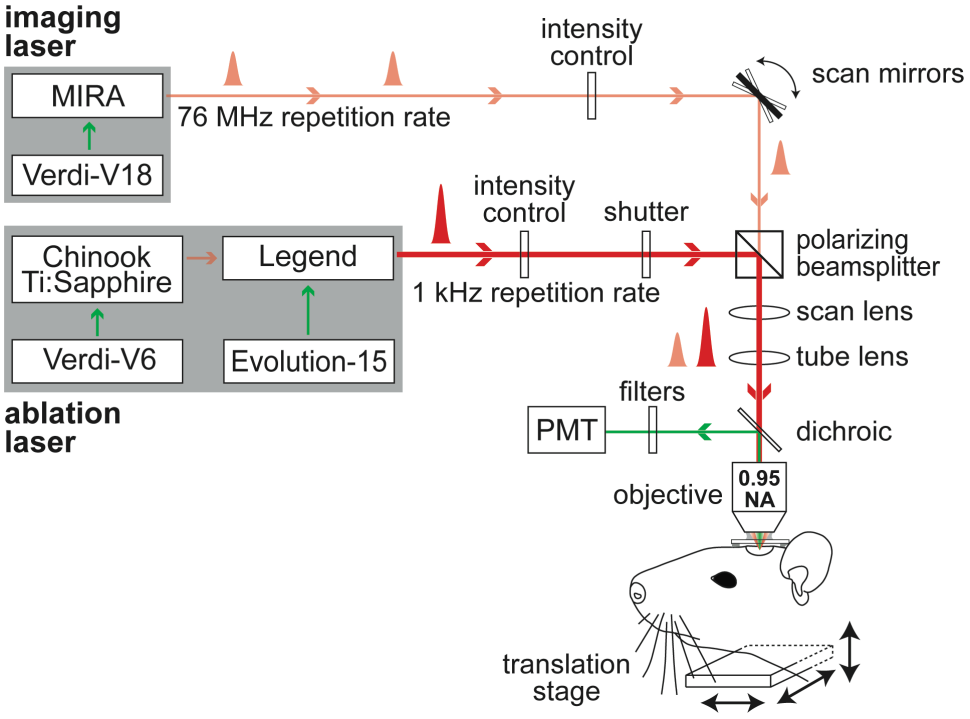

Figure 3.12 Setup for *in vivo* imaging and ablation. Following the craniotomy, the animal was placed on a translational stage that allowed for navigation of the cranial window. Two-photon images were obtained by raster scanning the window with a high-repetition rate, femtosecond pulse train and collecting the two-photon excited fluorescence with a photomultiplier tube (PMT). Femtosecond laser pulses from a regenerative amplifier used for ablation were combined with the imaging beam using a polarizing beamsplitter to allow for simultaneous imaging and ablation.

References

1. Strangman G, Boas DA, Sutton JP. Non-invasive neuroimaging using near-infrared light. Biol Psychiat 2002; 52(7):679-693.
2. Helmchen F, Denk W. Deep tissue two-photon microscopy. Nat Methods 2005; 2(12):932-940.
3. Oheim M, Beaurepaire E, Chaigneau E, Mertz J, Charpak S. Two-photon microscopy in brain tissue: parameters influencing the imaging depth (vol 111, pg 29, 2001). J Neurosci Meth 2001; 112(2):205-205.
4. Svaasand LO, Ellingsen R. Optical-Properties of Human-Brain. Photochem Photobiol 1983; 38(3):293-299.
5. Villringer A, Them A, Lindauer U, Einhaupl K, Dirnagl U. Capillary Perfusion of the Rat-Brain Cortex - an in-Vivo Confocal Microscopy Study. Circ Res 1994; 75(1):55-62.
6. Zipfel WR, Williams RM, Webb WW. Nonlinear magic: multiphoton microscopy in the biosciences. Nat Biotechnol 2003; 21(11):1369-1377.
7. Konig K. Multiphoton microscopy in life sciences. J Microsc-Oxford 2000; 200:83-104.
8. Denk W, Strickler JH, Webb WW. 2-Photon Laser Scanning Fluorescence Microscopy. Science 1990; 248(4951):73-76.
9. Zipfel WR, Williams RM, Christie R, Nikitin AY, Hyman BT, Webb WW. Live tissue intrinsic emission microscopy using multiphoton-excited native fluorescence and second harmonic generation. P Natl Acad Sci USA 2003; 100(12):7075-7080.
10. Barad Y, Eisenberg H, Horowitz M, Silberberg Y. Nonlinear scanning laser microscopy by third harmonic generation. Appl Phys Lett 1997; 70(8):922-924.

11. Williams RM, Zipfel WR, Webb WW. Interpreting second-harmonic generation images of collagen I fibrils. Biophys J 2005; 88(2):1377-1386.
12. Vogel A, Noack J, Huttman G, Paltauf G. Mechanisms of femtosecond laser nanosurgery of cells and tissues. Appl Phys B-Lasers O 2005; 81(8):1015-1047.
13. Schaffer CB, Nishimura N, Glezer EN, Kim AMT, Mazur E. Dynamics of femtosecond laser-induced breakdown in water from femtoseconds to microseconds. Opt Express 2002; 10(3):196-203.
14. Schaffer CB, Brodeur A, Mazur E. Laser-induced breakdown and damage in bulk transparent materials induced by tightly focused femtosecond laser pulses. Meas Sci Technol 2001; 12(11):1784-1794.
15. Keldysh LV. Ionization in Field of a Strong Electromagnetic Wave. Sov Phys Jetp-Ussr 1965; 20(5):1307-&.
16. Schaffer CB, Garcia JF, Mazur E. Bulk heating of transparent materials using a high-repetition-rate femtosecond laser. Appl Phys a-Mater 2003; 76(3):351-354.
17. Kleinfeld D, Delaney KR. Distributed representation of vibrissa movement in the upper layers of somatosensory cortex revealed with voltage-sensitive dyes. J Comp Neurol 1996; 375(1):89-108.
18. Nguyen QT, Tsai PS, Kleinfeld D. MPScope: A versatile software suite for multiphoton microscopy. J Neurosci Meth 2006; 156(1-2):351-359.
19. Nishimura N, Schaffer CB, Friedman B, Tsai PS, Lyden PD, Kleinfeld D. Targeted insult to subsurface cortical blood vessels using ultrashort laser pulses: three models of stroke. Nat Methods 2006; 3(2):99-108.
20. Vogel A, Venugopalan V. Mechanisms of pulsed laser ablation of biological tissues. Chem Rev 2003; 103(2):577-644.

Chapter 4
The impact of single venule occlusions

In this chapter, we present a study that investigates the effects of single venule occlusions. We use two-photon microscopy to map the cortical vasculature and to measure blood flow and diameter in individual vessels and a method for precise and controlled occlusions of venules using femtosecond laser ablation is presented. We also perform detailed analyses of the cortical vasculature and conclude that the vascular architecture plays a large role in the severity of blood flow reductions following a small stroke.

This work is published in the *Journal of Cerebral Blood Flow and Metabolism*. At the time of writing this dissertation, the manuscript was only available as an "Advanced online publication," but can be found with the following citation:

John Nguyen, Nozomi Nishimura, Robert N Fetcho, Costantino Iadecola, Chris B. Schaffer: Occlusion of cortical ascending venules causes blood flow decreases, reversals in flow direction, and vessel dilation in upstream capillaries. *JCBFM*, 2011.

4.1 Implication of small stroke

There is increasing evidence that cerebral venous insufficiency may play a role in many brain diseases. Small ischemic lesions in the cortical grey matter (Figure 4.1) and in the periventricular and subcortical white matter have been linked to the development of cognitive dysfunction [1-3]. These lesions, which have previously been attributed to arteriolar clots or hemorrhages [4], have recently also been found to correlate with venule pathology and occlusion

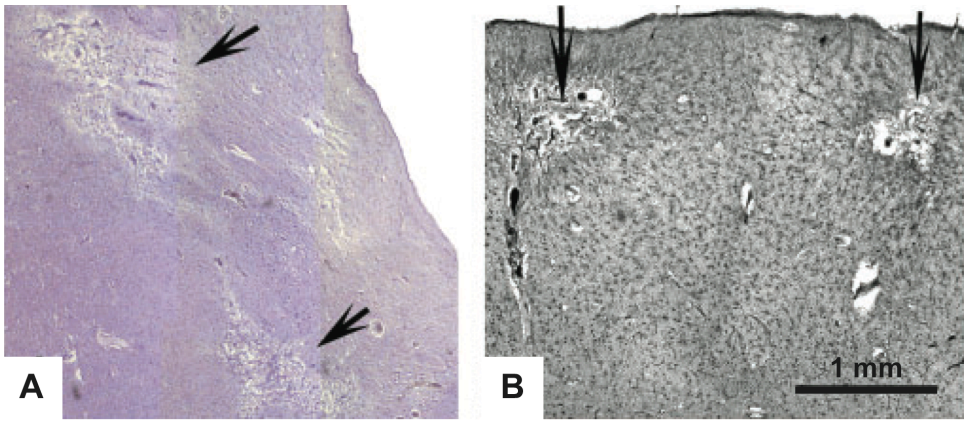

Figure 4.1 Staining of brains slices from patients with dementia. Human brain slices stained with **A)** hematoxylin and eosin and **B)** Globus silver staining (proteins). Arrows point to areas of de-staining, or dead tissue, which are most likely attributed to microvascular occlusions. Reprinted with permission from [38]

[6,7]. Furthermore, venular occlusions have long been thought to play either a primary or secondary role in multiple sclerosis [8,9]. However, due in part to limitations of existing animal models of microvascular occlusion, very little is known about the impact of venule occlusions on cerebral hemodynamics.

Previous studies have focused on the blood flow deficits resulting from thrombosis in large cerebral veins. Occlusion of the superior sagittal sinus [10] and its bridging veins [11,12] in animal models caused severe blood flow reductions in underlying capillaries and resulted in ischemic infarction. Additional studies of the occlusion of the superior sagittal sinus have shown that blood flow reductions were not as severe when more bridging veins were present, suggesting that vascular topology may be critical for the blood flow redistribution [13]. Although these studies provide insight into the effects of thrombosis of larger surface veins, the techniques used for blocking these large vessels do not translate to the production of clots in smaller (<50-μm diameter) surface venules (SVs) or ascending venules (AVs). The recent finding that femtosecond laser ablation [14] can be used to initiate clotting in individual vessels has permitted targeted occlusion of single cortical penetrating arterioles (PAs) [15,16] and capillaries [17]. This nonlinear optical technique is an ideal tool for producing occlusions in targeted cortical venules to investigate whether small venule clots in the cerebral vasculature lead to physiologically important blood flow deficits.

In this study, we quantified the effects of single venule occlusions on blood flow in the rat neocortex. We used femtosecond laser ablation to damage the endothelium and induce clotting in targeted venules and employed two-photon excited fluorescence (2PEF) microscopy to investigate the resulting blood flow and vessel diameter changes as a function of both of topological

separation and spatial distance from the occluded vessel. We found that occlusion of a single AV caused dramatic decreases in blood flow and increases in vessel diameter in capillaries that were upstream from the targeted venule. Similar results were observed following the occlusion of a SV, but flow decreases were almost eliminated when a surface collateral vessel that provided a new drain was present. We mapped the cortical microvascular topology in 600 μm x 600 μm x 500 μm sized volume and used these data to predict the spatial extent and severity of the blood flow reduction following an AV occlusion and found these predictions to agree well with *in vivo* measurements. These results highlight the dominant influence of vascular topology in determining the blood flow rearrangements that result from a vascular occlusion and provide the first comprehensive, quantitative picture of the blood flow rearrangements that result from cortical venular occlusions.

4.2 Experimental methods

Experiments were performed on 27 male Sprague Dawley rats (Harlan Inc.) ranging from 265–375 g in mass. AV occlusions were induced in 16 animals, SV occlusions were induced in eight animals (with collateral vessel: three, no collateral: five) and the rest were used in sham experiments. Only one venule was occluded in each animal. Refer to Chapter 3.5 for general surgical procedures and optical setup.

Two-photon imaging of the cortical vasculature. Using large-area 2PEF images, surface vessels were identified and large venules were followed upstream to identify candidate AVs and SVs for occlusion (Figure 4.2A). The vasculature surrounding the target venule was mapped with 1-μm spaced

image stacks. These high-resolution image stacks were used to map the topological relationship and spatial distance between measured vessels and the targeted venule (Figure 4.2B). Diameters were measured by averaging at least ten movie frames and manually selecting a segment of the vessel. The selected region was then thresholded (20% of maximum intensity) and the average width across the length of the selected segment was calculated as the vessel diameter (Figure 4.2Ci). Centerline red blood cell (RBC) velocities were obtained by tracking the motion of RBCs, which do not take up the intravenously injected dye and show up as dark patches inside the vessel (Figure 4.2Cii). Repetitive linescans along the axis of the vessel, at a rate of 1.7 kHz for about one minute, were used to form a space-time image where moving RBCs produce streaks with a slope that is equal to the inverse of the speed (Figure 4.2Ciii; characteristic diameter and RBC flow speed of all measured vessels shown in Figure 4.3). The slope was calculated using an automated image-processing algorithm [18]. Measured parameters were then mapped to vascular networks that included the targeted venule (Figure 4.2D).

Vessel identification. AVs were defined as vertically-oriented, subsurface vessels that transported blood from the capillary bed to the brain surface, as confirmed through measurement of blood flow direction. Vessels directly downstream from AVs and on the brain surface were defined as SVs. Surface arterioles, which form a net-like network on the brain surface, as well as PAs, which transport blood vertically into the brain, were also identified (Figure 4.2A). The PAs fed an extensive network of capillaries that eventually connected to and drained into AVs. We defined all subsurface vessels between a PA and an AV as capillaries. We determined the dependence of blood flow

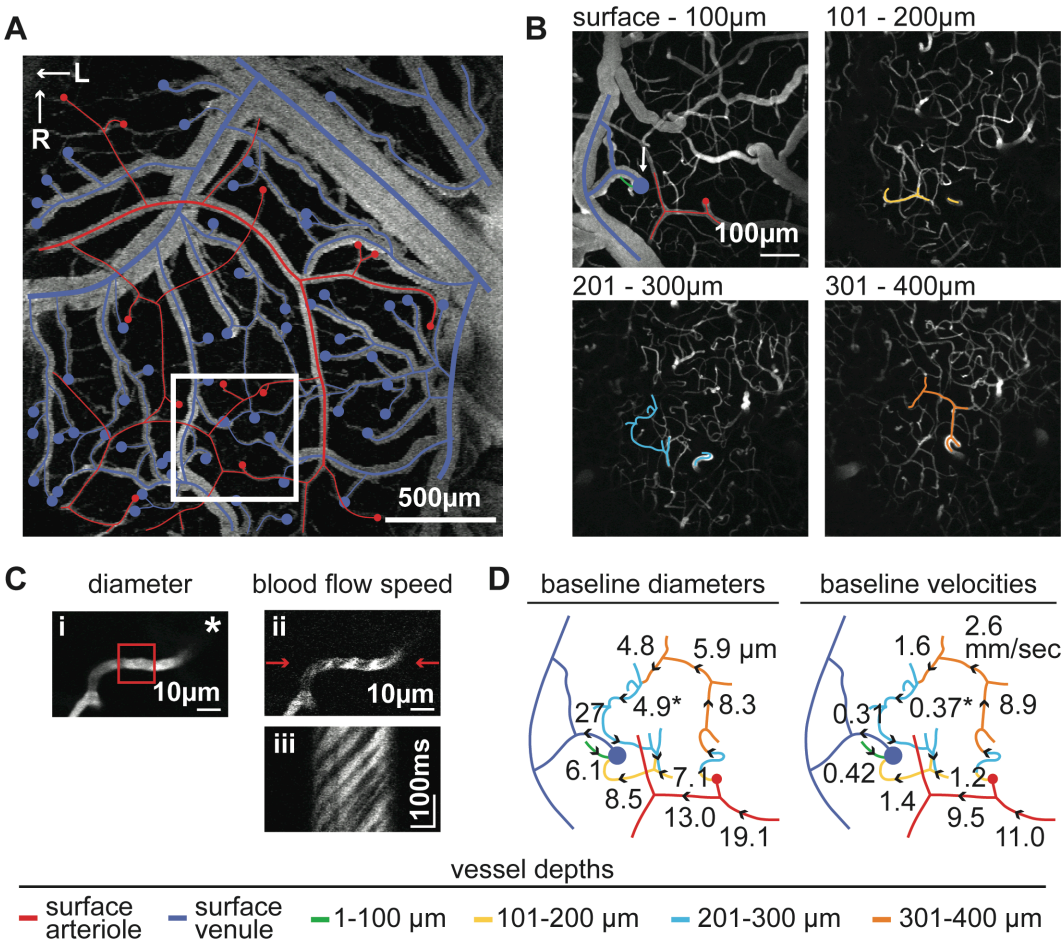
A
←L
↑R
500µm
B
surface - 100µm
101 - 200µm
100µm
201 - 300µm
301 - 400µm
C
diameter
blood flow speed
i
*
10µm
ii
10µm
iii
100ms
D
baseline diameters
baseline velocities
4.8
5.9 µm
27
4.9*
8.3
6.1
7.1
8.5
13.0
19.1
1.6
2.6
mm/sec
0.31
0.37*
8.9
0.42
1.2
1.4
9.5
11.0
vessel depths
surface arteriole
surface venule
1-100 µm
101-200 µm
201-300 µm
301-400 µm

Figure 4.2

Figure 4.2 2PEF microscopy to map and measure cortical vessels. A) Averaged projection of a 2PEF image stack of fluorescently labeled vasculature. Surface (penetrating) arterioles and surface (ascending) venules are indicated with red and blue lines (circles), respectively. The white box indicates the magnified region shown in panel *B*. Arrows labeled R and L indicate rostral and lateral directions. **B)** Series of 100-μm thick average projections of a 2PEF image stack starting from the brain surface to a depth of 400 μm. In each image projection, selected surface and sub-surface vessels are outlined, indicating the vascular network where vessel diameter and blood flow velocity were quantified. White arrow indicates the targeted AV. **C)** Averaged 2PEF image of an individual capillary used to measure vessel diameter *(i)* along a selected segment (red box), single 2PEF image frame of red blood cells flowing through a capillary, with arrows indicating the path of the linescan (*ii*), and the corresponding space-time image from a linescan from which the blood flow speed can be determined (*iii*). **D)** Baseline diameter and blood flow speed measurements of the vascular network traced in panel *B*, where arrows indicate blood flow direction and the asterisk-marked value corresponds to the capillary measured in panel *C*. Color coding indicates the vessel depth. The occlusion of the AV in this network and the resulting changes in vessel diameter and blood flow are shown in Figures 4.5 and 4.7, respectively.

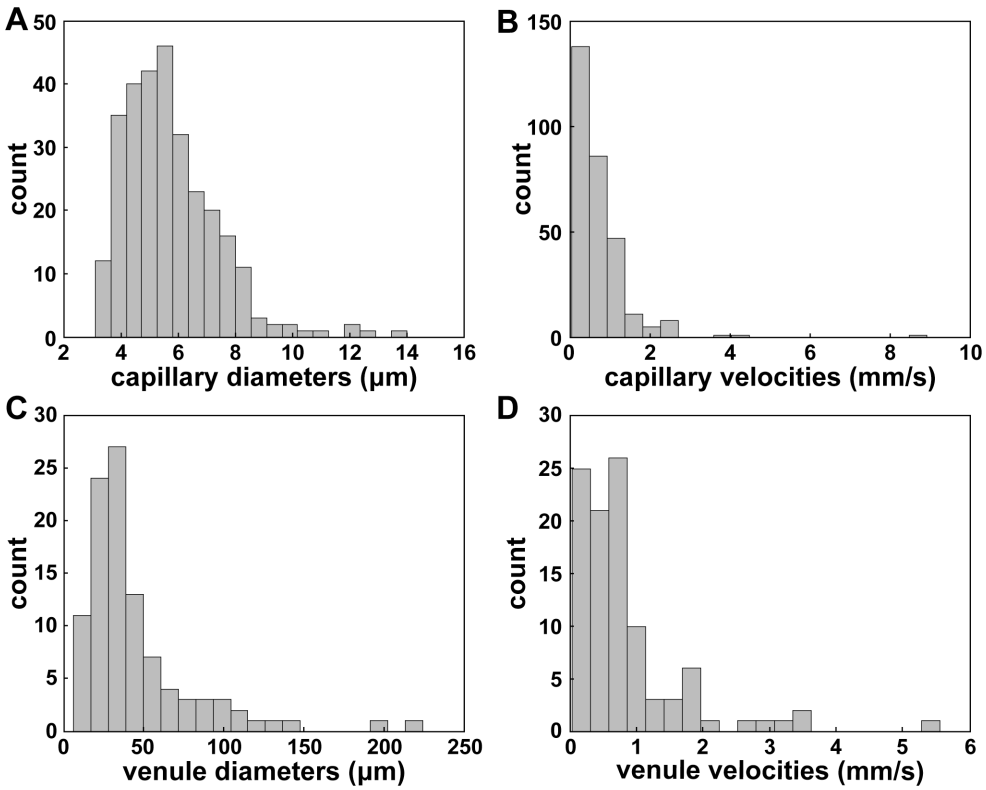

Figure 4.3 Histogram of baseline diameter and speed for all measured capillaries and venules. For this study, 298 capillaries were measured with a baseline median **(A)** diameter and **(B)** speed of 5.4 μm and 0.49 mm/s, respectively. Additionally, 102 surface venules were measured, with a baseline **(C)** diameter and **(D)** speed of 33 μm and 0.61 mm/s, respectively.

and vessel diameter changes after venule occlusion on topological separation by counting the number of vessel branches between a measured vessel and the occluded venule. Measured capillaries that could not be traced back to the targeted venule were grouped as "not connected" (NC).

Topology for surface venule occlusions. For SV experiments, we found two topologically distinct vascular patterns for the SVs immediately upstream from AVs. Both patterns were comprised of two AVs that merged into one SV, forming a "Y" shaped architecture (outlined in blue; Figure 4.11A and 4.11B). The two patterns were distinguished by the presence or absence of a "collateral" SV that connected to another SV (purple line and dashed blue lines, respectively; Figure 4.11A). In both topologies, occlusions were induced in the merged venule (red circles; Figure 4.11A and 4.11B) and vessel diameter and blood flow measurements were made in upstream SVs and capillaries.

Targeted clotting of venules by femtosecond laser ablation. Femtosecond laser pulses were tightly focused on the wall of the targeted vessel, causing nonlinear absorption of laser energy that drives photodisruptive damage [17]. This injury initiated the natural clotting cascade, forming a clot that stopped blood flow in the targeted venule (Figure 4.4). Because nonlinear absorption occurred only at the focus where laser intensity was the highest, photodisruption was confined to the focal volume, leaving the surrounding vessels and tissues intact. Pulse energy for ablation was varied with neutral density filters and the number of pulses focused in the vessel lumen was

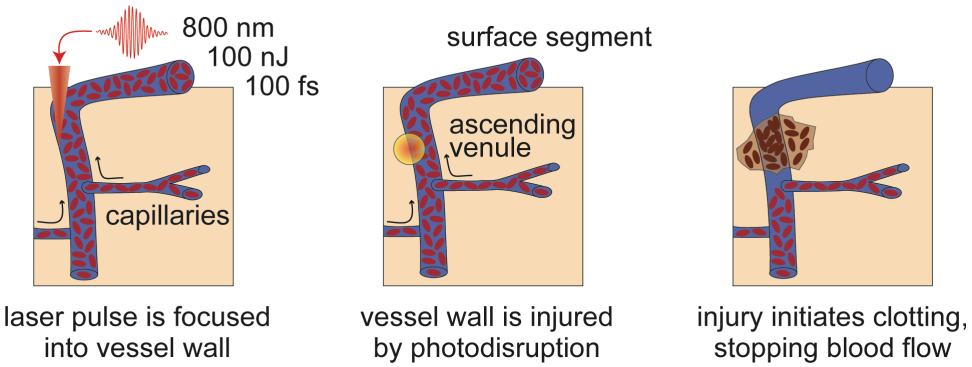

Figure 4.4 Schematic of venule clotting process. High-energy femtosecond laser pulses are tightly focused on to the vessel lumen (left). If a sufficient amount of laser energy is deposited at the focus, nonlinear absorption of the laser light can occur, and injure the vessel through photodisruption (middle). This injury initiates the natural clotting cascade. After injuring the vessel at multiple locations along the lumen, the vessel eventually becomes clotted, stopping blood flow (right).

controlled using a mechanical shutter with a 2-ms minimum opening time. For AV occlusions, the targeted segment was always located above the first branching upstream capillary and below the brain surface, at a depth of several tens of micrometers. Initially, venules were irradiated with a single pulse with energy below the expected damage threshold (~100 nJ at a depth of ~50 μm). The number of pulses was then increased from a single pulse to 1000 pulses, by increments of 100, until damage was observed, which was indicated by extravasation of fluorescently-labeled plasma outside the vessel. If no injury was observed, the energy was increased by ~25% and the process was repeated. Once extravasation occurred, the vessel was irradiated at multiple locations along the lumen until the motion of red blood cells ceased and an accumulation of RBCs in the targeted vessel segment was observed (Figure 4.5). The procedure for occluding SVs was similar, except that the initial laser energies used were lower because the target vessel was located on the brain surface. Characteristic diameter and RBC flow speed of target venules shown in Figure 4.6.

Characterization of capillary topology and prediction of spatial dependence of blood flow change after PA or AV occlusion. 2PEF image stacks from six additional rats were used to quantify the locations of AVs and PAs over ~4 mm^2 of brain surface (Figure 4.15A) and determine the nearest-neighbor separations (Figure 4.16). In three animals, we traced the connectivity of all vessels within a ~0.1-mm^3 volume of brain tissue using custom software (Figure 4.15B and 4.15C). From this data, we quantified the distance between

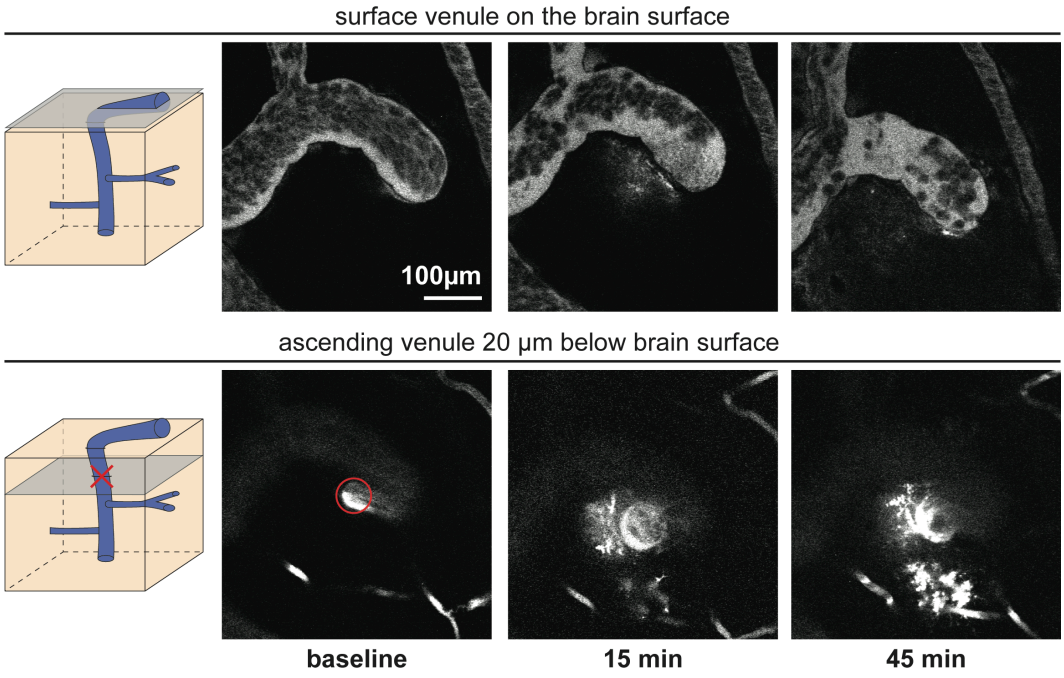
surface venule on the brain surface
100µm
ascending venule 20 µm below brain surface
baseline
15 min
45 min

Figure 4.5

Figure 4.5 Example of an AV occlusion. Grey planes in schematics on the left indicate the imaging plane, with the red X indicating the location of targeted ablation in the AV. The images on the right show a time-lapse series of the surface segment (top) and the 20-μm deep ascending segment (bottom) of the target vessel during clotting. This example shows clotting of an AV by ablation of the ascending segment of the vessel, approximately halfway between the first branching capillary and the brain surface. At baseline, flow of red blood cells was evident in the ascending and surface segments of the targeted venule. The vessel wall of the ascending segment was irradiated with 100-nJ pulses until we observed extravasation of fluorescently labeled blood plasma, indicating that the vessel wall was injured (15 min.). Further damage was induced along the vessel wall until a clot formed and complete cessation of red blood cell motion in the ascending and surface segments was observed (45 min.). Nearby surface vessels were not clotted and remained flowing.

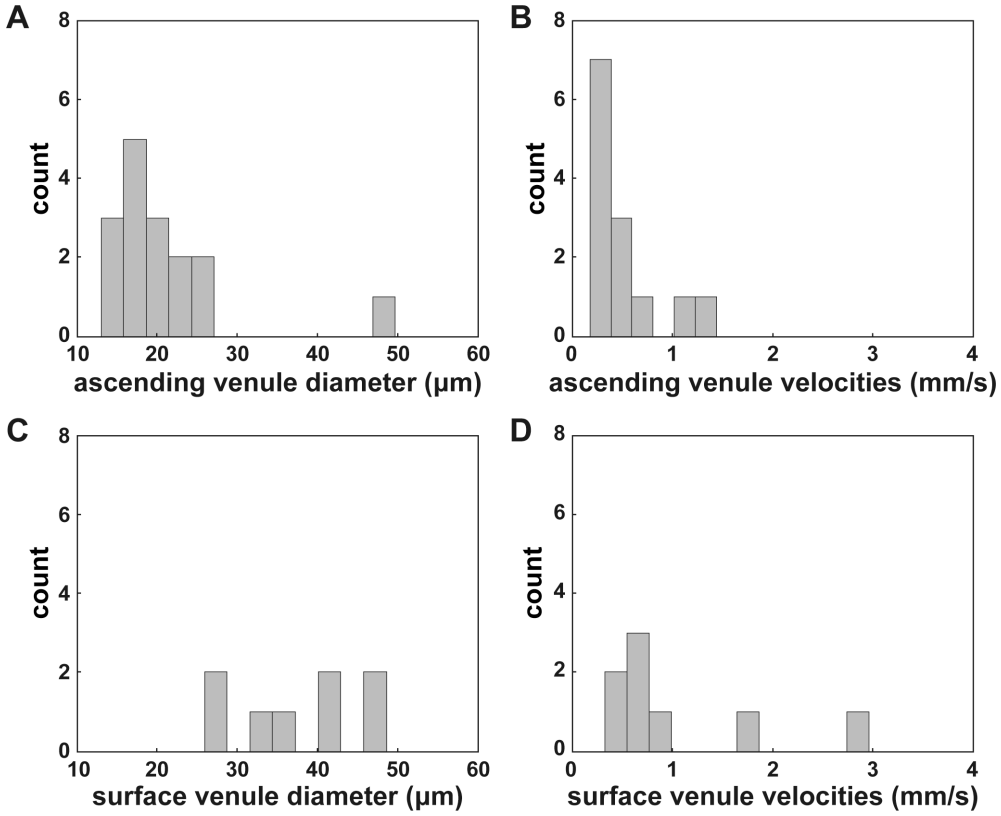

Figure 4.6 Histogram of baseline diameter and speed of occluded venules. Sixteen AVs were targeted with a baseline median **(A)** diameter of 18.4 μm and **(B)** speed of 0.32 mm/s. Eight SVs were targeted with a baseline median **(C)** diameter of 39.3 μm and **(D)** speed of 0.59 mm/s.

capillary segments and the nearest AV (2153 capillaries) or PA (2203 capillaries) as a function of the number of branches upstream or downstream the capillary was from the AV or PA (Figure 4.17A). We then determined the distribution of capillary branch numbers as a function of distance from PAs and AVs in 50-μm radial bins. We used *in vivo* flow change data from this study for AV occlusions and from previous work for PA occlusions [16] to determine the average blood flow decrease in different capillary branches stemming from an occluded AV or PA. Combining both the capillary branch number distribution (Figure 4.17A) and this flow change data, we predicted the post-clot blood flow speed change as a function of distance from occluded AVs and PAs (Figure 4.17B).

Data analysis and statistics. Boxplots were generated with Matlab (The Mathworks) using the boxplot function (Figures 4.8A, 4.10A, 4.14A, and 4.14C). The dependence of median RBC flow speed change (Figure 4.8B), reversal rate (Figure 4.9B), and mean vessel dilation (Figure 4.10B) in capillaries as a function of distance from occluded AVs were determined using a variable width spatial window that was constrained to contain 20 data points. Trend lines were further smoothed with a 20-μm moving average and a running 95% confidence interval about the trend line was calculated.

Differences were considered significant for p-values less than 0.05. For nonparametric data, rank-based analysis was conducted using Dwass-Steel-Critchlow-Fligner (StatsDirect) multiple comparisons test (Figures 4.8A and 4.14A) whereas normally distributed data were analyzed using the Tukey-

Kramer (StatsDirect) multiple comparisons test (Figures 4.10A, 4.14C, and 4.18B). For binomial data, statistical differences were calculated using a binomial proportions test with a Bonferroni adjustment (Figures 4.9A and 4.14B). Medians are reported for nonparametric data, whereas means are reported for normal data.

4.3 Results

We used 2PEF imaging of fluorescently-labeled blood plasma in anesthetized rats to map vascular topology and quantify blood flow speed and vessel diameter in surface vessel and capillary networks near AVs and SVs that were candidates for occlusion (Figure 4.2A). Irradiation of the targeted venules with high-energy, tightly-focused, femtosecond laser pulses caused localized vascular injury, leading to extravasation of fluoresecently-labeled plasma and RBCs and triggering clotting of the vessel (Figure 4.5). Nearby surface vessels and capillaries were not clotted and remained flowing. We then measured the changes in diameter and RBC centerline velocity that resulted from the venule occlusion in individual vessels throughout the nearby vascular network (Figure 4.7).

4.3.1 Venule occlusions

In this study we target two classes of venules: ascending and surface. The majority of the data and analysis stem from the ascending venule occlusions, but SV studies provide new insights as well. Clots were induced in the sub-surface segment of an AV that was just below the brain surface, or in a segment of SVs. Figure 4.5 shows a time sequence of two-photon images of the

occlusion technique. Two–photon images of surface venule occlusions are shown in Figures 4.12 and 4.13.

4.3.2 Ascending venule occlusion

In occlusion experiments, the RBC speed and diameters of individual vessels were measured before and after the occlusion (Figure 4.7Aii and 4.7Bii). The location of each measured vessel was mapped relative to the targeted venule enabling maps of vessel networks with corresponding changes in RBC speed and vessel diameter (Figure 4.7C). In this example, capillaries close to the occlusion slowed down, reversed in flow direction, and increased in vessel diameter.

4.3.2.1 Blood flow reductions

To understand the impact of ascending venule occlusions on blood flow in nearby and connected blood vessels, we investigated how changes in blood flow speed depend on the topological connection and the spatial distance between individual vessels and the occluded venule. RBC speed in capillaries that were one to four branches upstream from the clotted venule decreased dramatically, with flow speeds of only 6% (16%) of the baseline value for vessels one (two) branch(es) upstream from the occlusion (Figure 4.8A). Average speed did not change in capillaries that were more than four branches upstream or not connected to the occluded venule, although vessels five to seven branches upstream showed a 9.5 times increased variance in speed after the occlusion when compared to sham experiments (Figure 4.8A; $p < 1.0E\text{-}7$, F-test). Surface venules downstream from the occluded venule slowed, while parallel surface venules (i.e. vessels that drained into the same

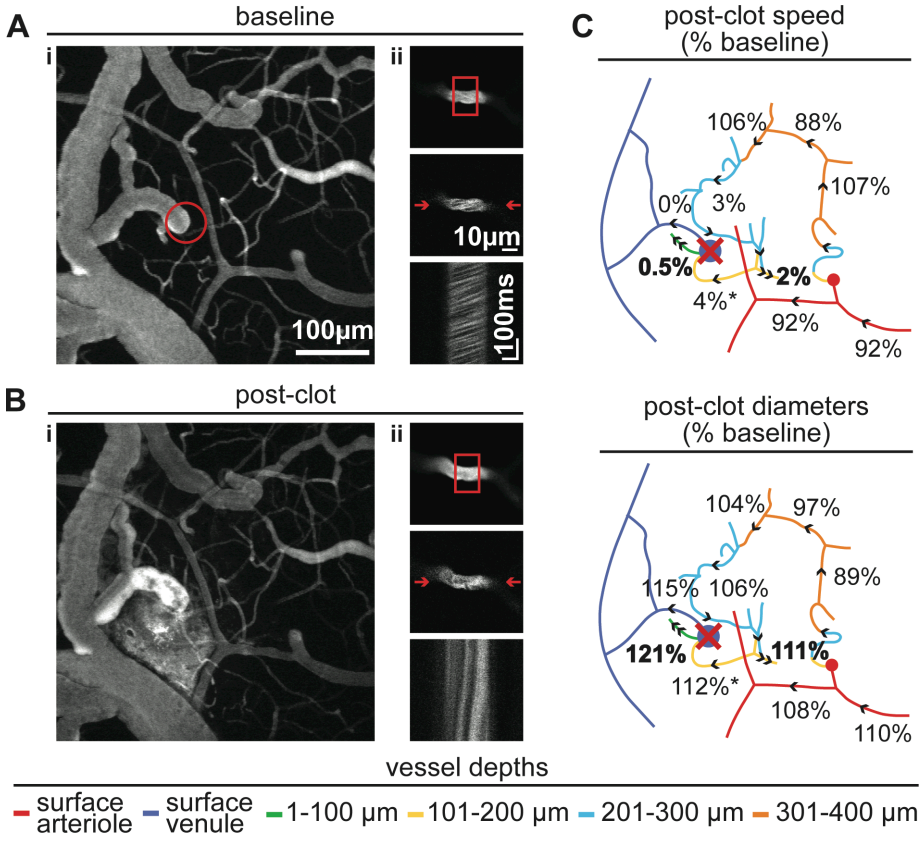
A
baseline
i
ii
100µm
10µm
100ms
B
post-clot
C
post-clot speed
(% baseline)
106%
88%
107%
0%
3%
0.5%
2%
4%*
92%
92%
post-clot diameters
(% baseline)
104%
97%
89%
115%
106%
121%
111%
112%*
108%
110%
vessel depths
surface arteriole
surface venule
1-100 µm
101-200 µm
201-300 µm
301-400 µm

Figure 4.7

Figure 4.7 Vascular and flow changes after an AV occlusion. 2PEF imaging at **A)** baseline and **B)** after clotting a single AV showing: (*i*) average projection of 100-μm deep image stack of fluorescently labeled vasculature, and (*ii*) image data for measurements of the diameter and RBC speed in an individual capillary. Extravasation of fluorescently labeled blood plasma was visible near the clotted venule in B(*i*), but nearby surface vasculature and underlying capillaries remained intact. There was a slight dilation in the capillary shown in A(*ii*) and B(*ii*) after the clot, and the post-clot linescan showed more vertically oriented streaks from moving RBCs, indicating dramatically decreased blood flow speed. **(C)** Vessel RBC speeds (top) and diameters (bottom) in the vascular network after the occlusion of an AV, expressed as a percentage of the baseline values. Vessels topologically close to the targeted venule slowed dramatically, two of the ten measured vessels reversed flow direction (indicated with double arrows and bold numerical values), and the majority of vessels increased in diameter. Red "X" indicates the location of the clotted AV. The vessel marked with an asterisk corresponds to the vessel in A(*ii*) and B(*ii*). The clotting sequence for this AV is shown in Figure 4.5.

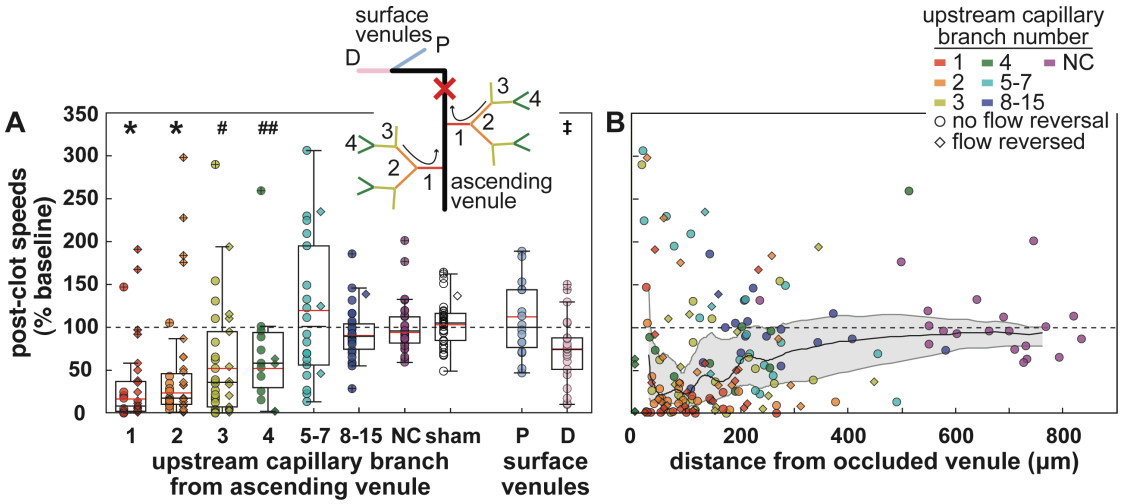
A
B
post-clot speeds
(% baseline)
350
300
250
200
150
100
50
0
*
*
#
##
‡
surface
venules
P
D
3
4
2
1
ascending
venule
1
2
3
4
5-7
8-15
NC
sham
P
D
upstream capillary branch
from ascending venule
surface
venules
upstream capillary
branch number
1
2
3
4
5-7
8-15
NC
no flow reversal
flow reversed
0
200
400
600
800
distance from occluded venule (μm)

Figure 4.8

Figure 4.8 AV occlusions resulted in decreased blood flow. A) Changes in RBC speed (expressed as percentage of baseline speed) following an AV occlusion for upstream capillaries and downstream surface venules as a function of topological connection to the occluded vessel. The schematic inset shows the vessel enumeration scheme, with arrows indicating the direction of blood flow at baseline and the red "X" indicating the occlusion location. **B)** Changes RBC speed as a function of distance away from the occluded AV for capillaries. The black line in *B* represents a running median. Capillaries topologically grouped in "NC" indicate no connection to the target vessel was able to be determined and "sham" indicates experiments where no vessel was clotted. P and D represent parallel and downstream surface venules, respectively. In speed and diameter plots, diamonds (circles) indicate vessels where flow did (did not) reverse direction after the occlusion. Black and red lines in the boxplots represent the median and mean, respectively. Statistical outliers, denoted with a crosshair, were excluded when calculating the mean. Color-coding to indicate topological connectivity is the same for Figure 3.7 and 3.8. Grey shaded region in *B* indicate the 95% confidence interval about the trend line. Three outlier points are not shown (groups: 4, sham, P; 5.9, 6.1, 5.2, respectively) in panels A and B. *: $p < 1.0E\text{-}7$, #: $p < 0.0005$, ##: $p < 0.005$, ǂ: $p < 0.05$; compared to sham vessels.

venule as the clotted vessel) did not change speed (Figure 4.8A). The median RBC speed in measured capillaries located within 100 μm of the occluded venule decreased to about 26% of the baseline value, and returned to baseline with increasing distance from the occluded vessel (Figure 4.8B).

4.3.2.2 Reversals in blood flow direction

In addition to changes in blood flow speed, we observed dramatic changes in the routing of blood flow through the capillary bed after AV occlusion. We frequently observed a reversal in blood flow direction in capillaries one to four branches upstream from the occluded venule, with just over half of the first and second upstream branches reversing flow direction (Figure 4.9A). Neither capillaries not connected to the occluded venule, nor downstream or parallel surface venules reversed flow direction (Figure 4.9A). The number of blood flow reversals in capillaries decreased with increasing distance from the occluded venule, with no flow reversals observed more than 650 μm away from target vessel (Figure 4.9B).

4.3.2.3 Capillary dilations

We further examined the impact of AV occlusions on the diameter of nearby and connected vessels. We found that capillaries up to three branches upstream from the targeted venule dilated after the clot as compared to sham experiments, with an average diameter increase of ~25% (Figure 4.10A). Capillaries further upstream or not connected to the targeted vessel, as well as downstream and parallel surface venules, did not dilate significantly (Figure 4.10A). The amount of dilation decreased with increasing distance from the clot, with no dilation observed at distances greater than 200 μm (Figure 4.10B).

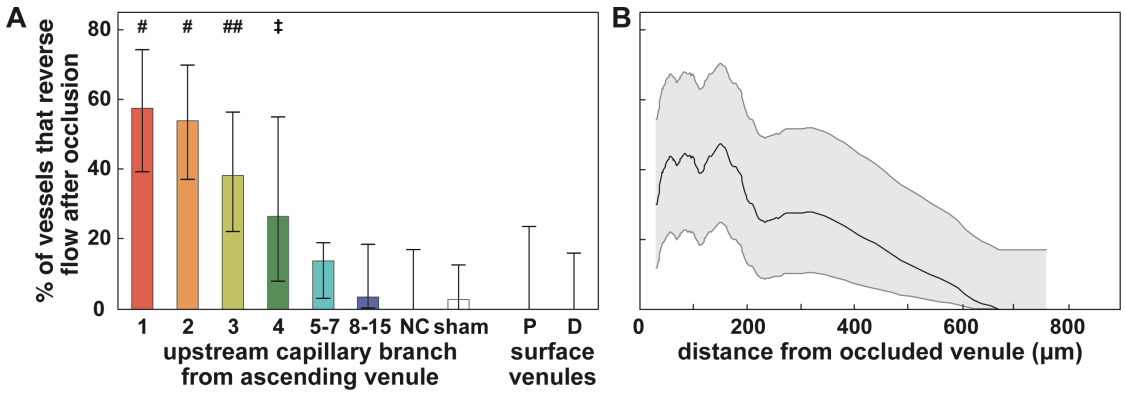
A
% of vessels that reverse flow after occlusion
80
60
40
20
0
#
#
##
‡
1
2
3
4
5-7
8-15
NC
sham
P
D
upstream capillary branch from ascending venule
surface venules
B
0
200
400
600
800
distance from occluded venule (μm)

Figure 4.9

Figure 4.9 Blood flow direction reversed after AV occlusions. A) Blood flow direction (percentage of vessels with reversed flow) following an AV occlusion for upstream capillaries and downstream surface venules as a function of topological connection to the occluded vessel. The schematic inset shows the vessel enumeration scheme, with arrows indicating the direction of blood flow at baseline and the red "X" indicating the occlusion location. **B)** Changes blood flow direction as a function of distance away from the occluded AV for capillaries. The black line in *B* represents a running fraction. Capillaries topologically grouped in "NC" indicate no connection to the target vessel was able to be determined and "sham" indicates experiments where no vessel was clotted. P and D represent parallel and downstream surface venules, respectively. Grey shaded region in *B* indicate the 95% confidence interval about the trend line. #: $p < 0.0005$, ##: $p < 0.005$, ‡: $p < 0.05$; compared to sham vessels.

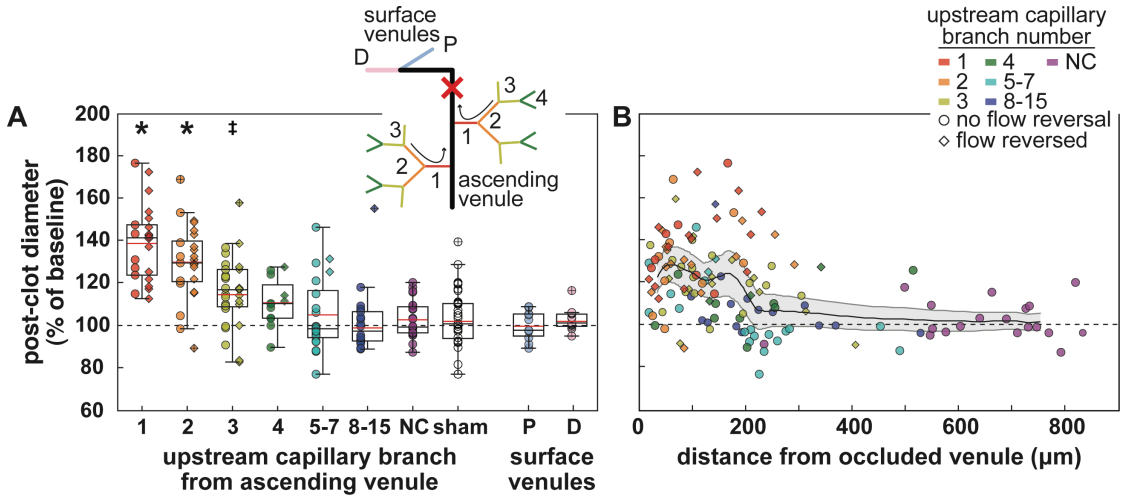
A
B
post-clot diameter (% of baseline)
200
180
160
140
120
100
80
60
*
*
‡
1
2
3
4
5-7
8-15
NC
sham
P
D
upstream capillary branch from ascending venule
surface venules
surface venules
D
P
ascending venule
upstream capillary branch number
1
2
3
4
5-7
8-15
NC
no flow reversal
flow reversed
0
200
400
600
800
distance from occluded venule (μm)

Figure 4.10

Figure 4.10 Capillaries increased in diameter after AV occlusion. A) Changes in vessel diameter (percentage of baseline diameter) following an AV occlusion for upstream capillaries and downstream surface venules as a function of topological connection to the occluded vessel. The schematic inset shows the vessel enumeration scheme, with arrows indicating the direction of blood flow at baseline and the red "X" indicating the occlusion location. **B)** Changes in vessel diameter as a function of distance away from the occluded AV for capillaries. The black line in *B* represents a running mean. Capillaries topologically grouped in "NC" indicate no connection to the target vessel was able to be determined and "sham" indicates experiments where no vessel was clotted. P and D represent parallel and downstream surface venules, respectively. In speed and diameter plots, diamonds (circles) indicate vessels where flow did (did not) reverse direction after the occlusion. Black and red lines in the boxplots represent the median and mean, respectively. Statistical outliers, denoted with a crosshair, were excluded when calculating the mean. Grey shaded region in *B* indicate the 95% confidence interval about the trend line. *: $p < 1.0E\text{-}7$, ‡: $p < 0.05$; compared to sham vessels.

4.3.3 Surface venule occlusions

We also examined the blood flow changes caused by the occlusion of SVs in vascular topologies that had (Figure 4.11A) and did not have (Figure 4.11B) a collateral SV. Examples of occlusion studies for both types are shown in Figures 4.12 and 4.13. On average, blood flow speeds in capillaries one and two branches upstream from the AVs were unaffected by a SV occlusion when a collateral vessel was present, while flow was reduced to an average of 12% of the baseline speed when no collateral vessel was present (Figure 4.14A). Blood flow reversals in the first two upstream capillaries occurred only when no collateral SV was present (Figure 4.14B). Diameters increased in the first upstream capillary branch only when no collateral vessel was present, while the second upstream capillary branch dilated following a surface vessel occlusion both with and without a collateral (Figure 4.14C).

4.3.4 Significance of vascular topology

In order to gain insight into the role of vascular topology in determining blood flow rearrangements after an occlusion, we used in vivo imaging to map the vascular topology over ~0.1 mm^3-volumes in cortex and combined this with topology-dependent measurements of RBC speed change after vascular occlusion to predict the spatial extent and severity of blood flow decrease. We found that the number of AVs outnumbered PAs by a factor of 1.8 (Figure 4.15A; 6 animals, 360 PAs to 201 AVs), and that the average distance between two PAs was significantly greater than the distance between two AVs (Figure 4.16). We used tracings of all vessels (Figure 4.15B and 4.15 C; 4256 capillaries in 3 animals) to determine the three-dimensional spatial location of each capillary as a function of topological connectivity to the

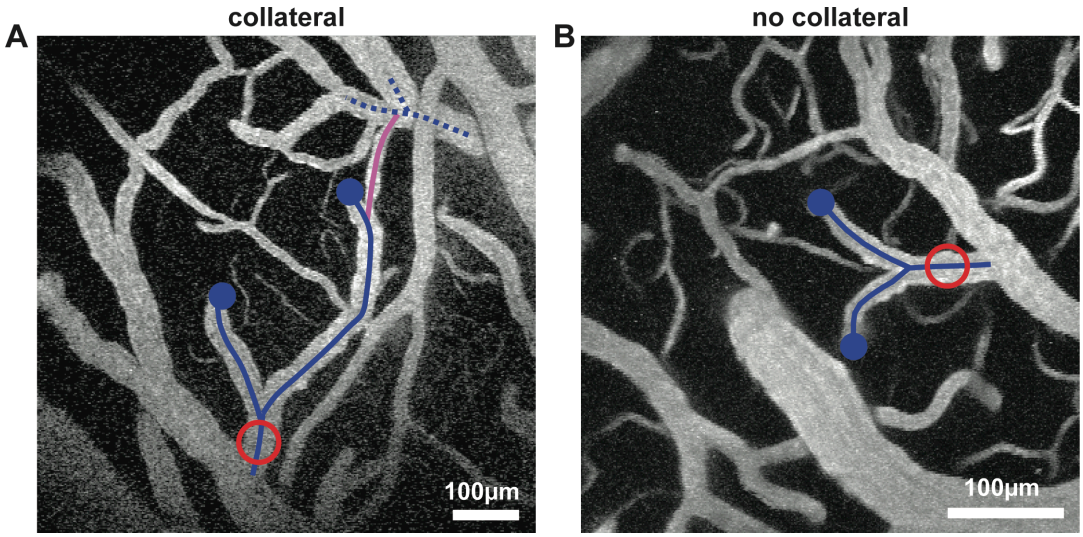

Figure 4.11 SV topologies with and without a collateral vessel. Averaged projections of 2PEF image stacks of brain surface vasculature with **(A)** a collateral vessel (purple) links a terminal venule with another draining surface venule (dashed) or **(B)** with no such collateral vessel. The red circle indicates the clot location. Maps of the flow changes in the upstream vessels after occlusion are shown in Figures 4.13 and 4.14.

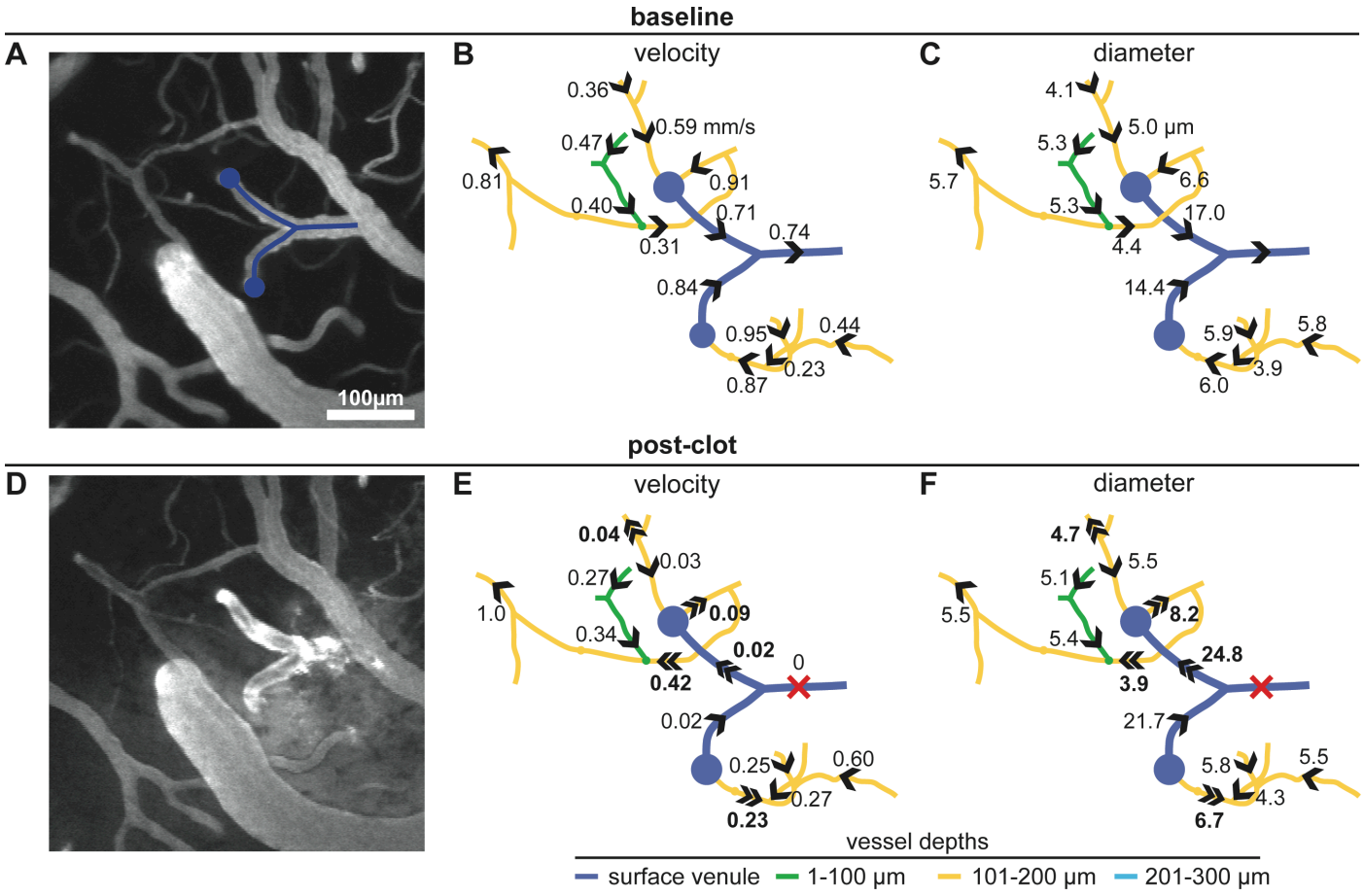
baseline
A
B
velocity
C
diameter
0.36
0.59 mm/s
0.47
0.81
0.91
0.40
0.71
0.74
0.31
0.84
0.95
0.44
0.23
0.87
100µm
4.1
5.0 µm
5.3
5.7
6.6
5.3
17.0
4.4
14.4
5.9
5.8
3.9
6.0
post-clot
D
E
velocity
F
diameter
0.04
0.03
0.27
1.0
0.09
0.34
0.02
0
0.42
0.02
0.25
0.60
0.27
0.23
4.7
5.5
5.1
5.5
8.2
5.4
24.8
3.9
21.7
5.8
5.5
4.3
6.7
vessel depths
surface venule
1-100 µm
101-200 µm
201-300 µm

Figure 4.12

Figure 4.12 Case study of SV occlusion with no collateral vessel. Average projection of a 2PEF image stack before **(A)** and after the clot **(D),** with the targeted venule indicated by the blue circle in A. Baseline **(B)** RBC velocities and **(C)** diameters are shown in upstream capillaries, with post-clot measurements in **(E)** and **(F),** respectively. Arrows indicate the direction of blood flow. Double arrowheads and bold values indicate vessels that reversed in flow direction following the occlusion and the red "X" indicates the location of the clot. Note that with no collateral vessel present, some capillaries upstream of AVs reverse in flow direction following the occlusion.

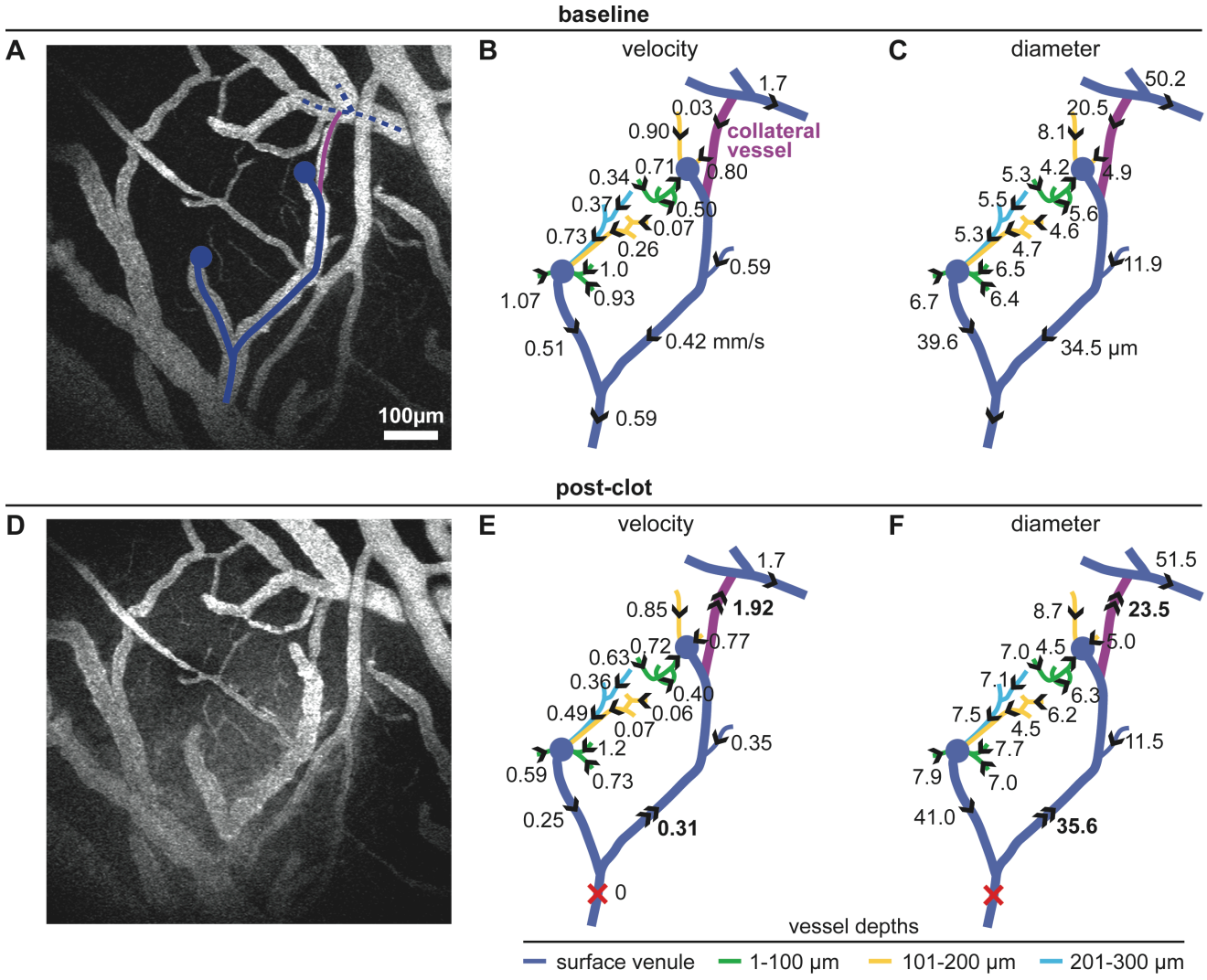
baseline
A
100μm
B
velocity
1.7
0.03
0.90
collateral vessel
0.71
0.80
0.34
0.37
0.50
0.07
0.73
0.26
1.0
0.59
1.07
0.93
0.51
0.42 mm/s
0.59
C
diameter
50.2
20.5
8.1
4.2
4.9
5.3
5.5
5.6
4.6
5.3
4.7
6.5
11.9
6.7
6.4
39.6
34.5 μm
post-clot
D
E
velocity
1.7
0.85
1.92
0.77
0.72
0.63
0.36
0.40
0.49
0.06
0.07
1.2
0.35
0.59
0.73
0.25
0.31
0
F
diameter
51.5
8.7
23.5
5.0
7.0
4.5
7.1
6.3
7.5
6.2
4.5
7.7
11.5
7.9
7.0
41.0
35.6
vessel depths
surface venule
1-100 μm
101-200 μm
201-300 μm

Figure 4.13

Figure 4.13 Case study of SV occlusion with collateral vessel. Average projection of a 2PEF image stack before **(A)** and after the clot **(D),** with the targeted venule indicated by the blue circle in A. Baseline **(B)** RBC velocities and **(C)** diameters are shown in upstream capillaries, with post-clot measurements in **(E)** and **(F),** respectively. The red "X" indicates the location of the clot. The collateral vessel (purple) connects the terminal vessel to another surface venule (dashed line). Note that in this example, when a collateral vessel is present, the capillaries upstream from AVs (blue circles in A) did not reverse in flow direction.

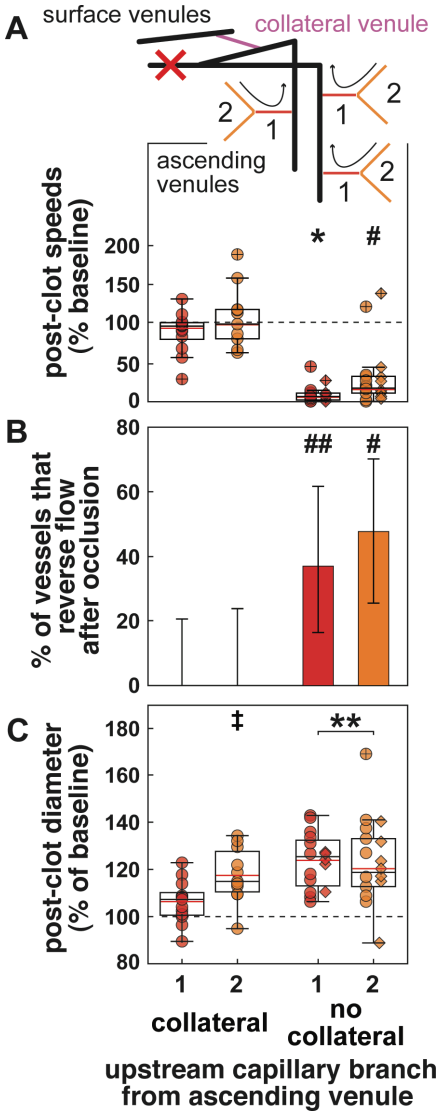
A
surface venules
collateral venule
2
1
1
2
ascending
venules
1
2
post-clot speeds
(% baseline)
200
150
100
50
0
*
#
B
% of vessels that
reverse flow
after occlusion
80
60
40
20
0
##
#
C
post-clot diameter
(% of baseline)
180
160
140
120
100
80
‡
**
1
2
1
2
collateral
no
collateral
upstream capillary branch
from ascending venule

Figure 4.14

Figure 4.14 Collateral SVs helped maintain normal flow. A) RBC speed in upstream capillaries, expressed as a percentage of the baseline values, for clots placed in surface venules with and without a collateral vessel. Schematic inset indicates the vascular topology considered, vessel designations, and location of the surface venule occlusion. **B)** Percentage of capillaries that reverse flow direction after surface venule occlusions. **C)** Plot of the vessel diameter, expressed as a percentage of the baseline value, for capillaries upstream from clots formed in surface venules. Diamonds (circles) indicate vessels where flow did (did not) reverse direction after the occlusion and the color-coding scheme is the same for all plots. *: $p < 1.0E-7$, **: $p < 0.00001$, #: $p < 0.0005$, ##: $p < 0.005$, ‡: $p < 0.05$; compared to sham vessels.

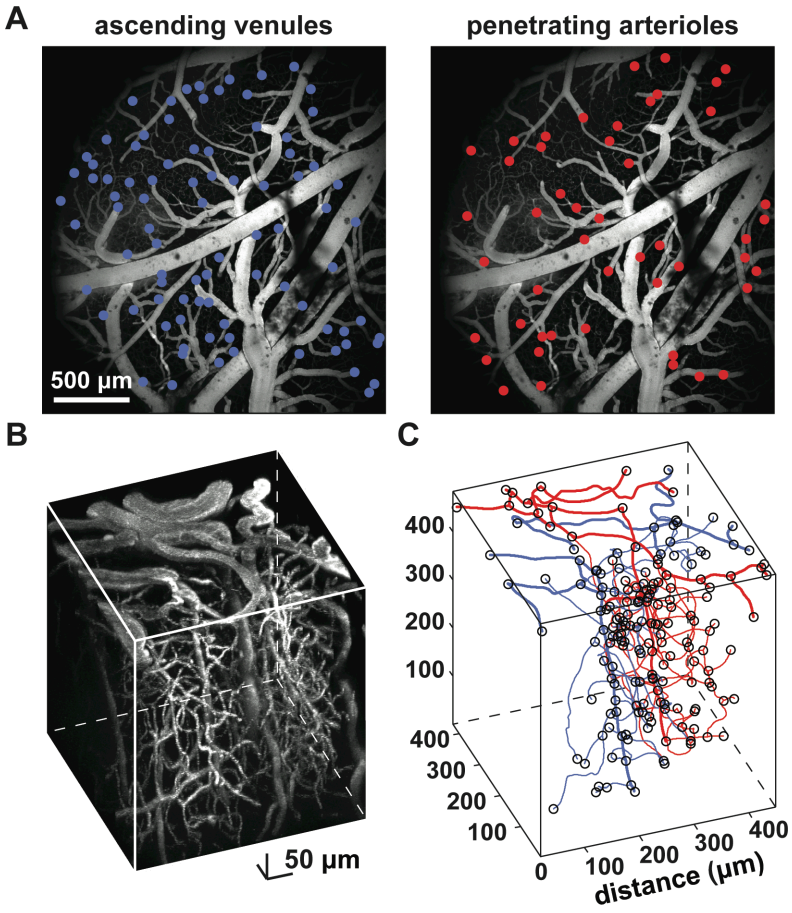
A
ascending venules
penetrating arterioles
500 µm
B
50 µm
C
400
300
200
100
400
300
200
100
0
100
200
300
400
distance (µm)

Figure 4.15

Figure 4.15 Mapping vascular topology. A) Average projections of a 2PEF image stack of the cortical surface vasculature. Locations of AVs (left) and PAs (right) are indicated by blue and red dots, respectively. **(B)** 2PEF, three-dimensional volumetric projection, using Voxx [5], of cortical vasculature starting at the brain surface. **C)** All vessels and bifurcation points were traced to characterize vascular topology. Surface vessels and a subset of the traced capillaries are shown (right) to emphasize the complexity of the cortical vasculature.

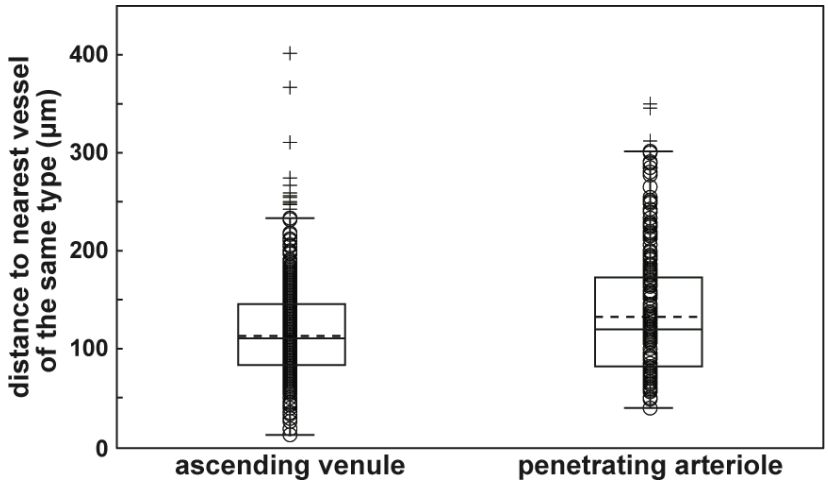

Figure 4.16 Nearest distance between two AVs and two PAs. The average distance between two PAs (145.9 μm ± 5.2 μm (mean ± SEM)) is significantly greater ($p < 0.01$, t-test) than the average distance between two AVs (123.6 μm ± 2.6 μm). Dashed and solid horizontal lines within boxes represent the mean and median, respectively.

nearest AV or PA. The average distance of capillaries from an AV or PA as a function of the number of branches upstream or downstream, respectively, was comparable (Figure 4.17A), suggesting a similarity in the capillary branching topology away from AVs and PAs. We then used *in vivo* measurements of capillary flow speed decreases after AV and PA occlusions as a function of topological separation from Figure 4.8A and from Nishimura *et al.* [16], respectively, to calculate the post-clot flow speed changes in capillaries as function of distance from the occluded vessel, weighted according to the topological data from Figure 4.17A. This calculation predicted both the spatial extent and severity of the blood flow deficit to be smaller following the occlusion of a single AV as compared to a PA (Figure 4.17B), in agreement with the experimental data from Figure 4.8B and previous work [15,16].

4.4 Discussion

We examined vessel-by-vessel hemodynamics following cortical venule occlusions using nonlinear optical techniques. Measurements of centerline RBC speed and direction, vessel diameter, and topological connectivity of individual vessels were obtained using 2PEF microscopy and femtosecond laser ablation was used to trigger clotting in targeted AVs and SVs. Vessels were measured before and after the occlusion in order to determine topologically and spatially dependent changes in RBC speed and direction as well as in vessel diameter. Capillaries immediately upstream from the target venule experienced a dramatic decrease in RBC speed, reversals in blood flow direction, and an increase in diameter, with each parameter recovering to baseline values in vessels further upstream from the clotted venule. Similar

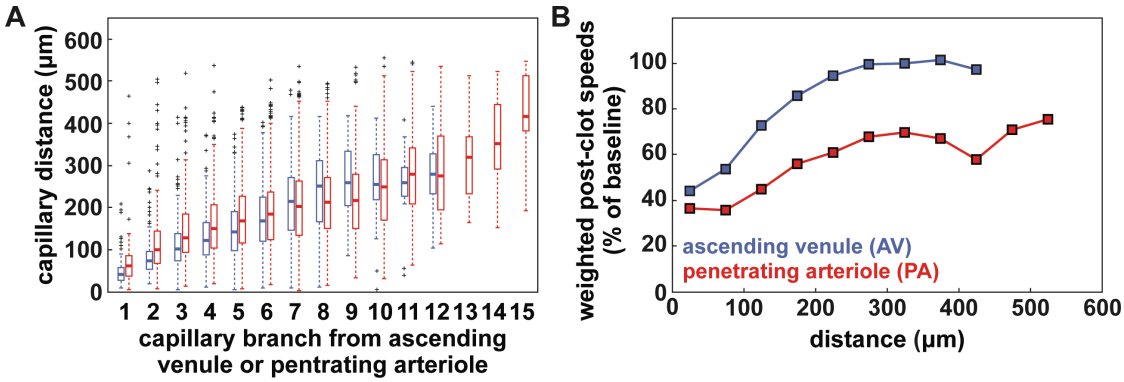

Figure 4.17 Flow changes depend on AV-AV and PA-PA spacing. A) Boxplot of capillary distance to nearest AV (blue) or PA (red) as a function of capillary branches away from an AV or a PA. **B)** A weighted calculation of post-clot speeds as a function of distance for occlusion of an AV (blue) and PA (red) using *in vivo* flow data that was topologically weighted based on the data in panel *C*. Each data point represents a weighted mean for a 50-μm binned window.

behaviors were observed in upstream capillaries following SV occlusions in topologies that did not contain a collateral vessel, while blood flow deficits were alleviated with the presence of a surface collateral venule. Furthermore, we studied the density of AVs and PAs as well as the topology of the capillaries that branch from them and used these values to predict differences in the spatial extent and severity of the blood flow decreases that result from AV and PA occlusions. These observations revealed the blood flow impact, both as a function of vascular topology and distance through the cortex, associated with cortical venule occlusions.

Nonlinear optical techniques enable the creation of robust models of small cortical venule occlusion. The ability to measure cerebral blood flow during normal and pathological states is critical for the development of an animal model of venule stroke. Most previous work on cortical venule occlusions has used laser Doppler flowmetry to characterize the flow changes that result from occlusion of cortical veins with ~0.1–1-mm diameter [10-13]. While this approach allows for mapping of regional blood flow changes resulting from large vessel occlusions, it would tend to average over the effects associated with occlusions in vessels with ~10–50-μm diameter, such as those considered in this study. Quantitative autoradiography has also been used to map tissue perfusion deficits after superior sagittal sinus occlusion [19], but this method does not enable the *in vivo* measurements that could, for example, connect vascular topology to blood flow change. In this study, we used 2PEF microscopy to characterize, at the vessel-by-vessel level, the changes in blood flow and diameter in vessels located deep within the cortical tissue after venule occlusion. While it is difficult to characterize a large number of vessels

in one experiment with this approach, the limited topological and spatial extent of the blood flow rearrangements we observed after AV and SV occlusion suggest 2PEF imaging is well suited to the study of these microvessel occlusions [20]. Other methods that enable simultaneous measurement of blood flow changes across many surface or penetrating/ascending vessels, such as Doppler optical coherence tomography [21] or advanced intrinsic optical imaging [22], could complement the approach taken here.

Conventional methods for producing vascular occlusions are not well suited to producing occlusions in small venules. Mechanical ligation approaches are limited to large vessels, such as the superior sagittal sinus [23]. Optical methods relying on linear excitation of an intravenously-injected photosensitizer [24] potentially provide higher precision [11], but thrombus formation is difficult to localize to a single vessel. Embolus injection models have been used to occlude smaller vessels [25], but this technique is inappropriate for venule occlusions, as the emboli will block arterioles and capillaries before ever reaching the venous system. In this study, we tightly focused high-energy, femtosecond laser pulses onto the vessel lumen to drive nonlinear absorption of the laser energy at the focus, thereby inducing an injury that is confined within the focal volume [17]. This injury triggers clotting in the target vessel, while leaving nearby vessels and the surrounding brain tissue morphologically intact. Overall, this approach provides a robust animal model of cortical venule occlusions that allows precise and controlled clotting of single venules at and below the brain surface with minimal collateral damage.

Topology is a dominant factor in the redistribution of blood following vascular occlusion. Vascular topology plays a crucial role in redistributing blood flow following a cortical vessel clot. Occlusion of communicating surface arterioles does not lead to severe decreases in flow in downstream arterioles and capillaries because the vascular anastomoses within the surface arteriole network provide collateral flow [18,26]. Similarly, after the occlusion of a surface venule with a collateral vessel, we find that blood flow changes in upstream capillaries are minimized, while topologies that do not contain a surface collateral venule result in severe blood flow decreases. These studies highlight the important role of redundancy in both the arterial and venular networks in maintaining flow following surface vessel occlusions. In contrast, occlusions in vessels with topologies that contain no collateral pathways, such as PAs and AVs, lead to flow decreases in underlying capillaries. Clotting of a PA results in severe decreases in blood flow in downstream capillaries to at least seven branches downstream from the targeted vessel [16], whereas blood flow is seen to recover after the fourth branch upstream following an AV occlusion. The difference in the topological distance through the capillary network at which blood flow recovers after a PA or AV occlusion can be attributed to the fact that PAs are outnumbered by AVs almost two to one. Because the capillary branching pattern is similar for both vessel types, this difference in density, and therefore in distance between two PAs or two AVs, suggests that the number of capillary branches between two PAs is greater than number of branches between two AVs. As a result, blood flow deficits in capillaries downstream from an occluded PA will extend further into the capillary network before another nearby PA is able to effectively provide alternatively-sourced blood flow. In contrast, because two AVs are closer,

blood in capillaries upstream from an occluded AV requires fewer branches to reach an alternative AV, resulting in less severe blood flow deficits. To further support this idea, we performed a topology-weighted analysis of capillary flow changes as a function of distance from an occluded vessel, which showed that the spatial extent and severity of blood flow decrease was less dramatic following an AV occlusion as compared to a PA occlusion. Together, these results not only implicate the role of vascular topology and connectivity in the redistribution of blood flow, but also highlight the importance of the occlusion location within the vascular hierarchy.

Capillary dilations are a passive process following an ascending venule occlusion. One of the key findings in this study is the large dilation in upstream capillaries following the occlusion of an AV. One question is whether or not the observed dilation is an active or passive process. Previous anatomical studies of the cerebral microvasculature have established the lack of smooth muscle cells in the capillaries upstream from AVs [27], suggesting that capillaries do not actively modulate their diameter. This leads to the hypothesis that the capillary dilations we observe are a passive process, induced by an increase in intravascular pressure, caused by the fact that after the venule occlusion the immediately upstream capillaries are now topologically further away from a low pressure draining venule. To model this scenario, we considered the capillary as a tube embedded in a matrix of brain tissue [28], with a Young's modulus, E, of 1.5 kPa and a Poisson's ratio, ν, of 0.5 [29]. The change in vessel radius, R, is then linked to the change in intravascular pressure, P, by

$$P_c - P_o = \left(\frac{E}{1+\nu}\right)\left(\frac{R_c - R_o}{R_o}\right) \qquad \text{(Eq. 4.1)}$$

where P_c and R_c are post-clot and P_o and R_o are baseline pressure and radius, respectively. Using Eq. 4.1, we calculated the pressure increase required to induce a dilation that agrees with our experimental measurements (Figure 4.18). The 5-10% increase in intravascular pressure we calculate compares well to the pressure difference measured between capillary beds and the first draining venules in cat mesentery [30]. We note, however, that pericytes have been shown to actively modulate the diameter of capillaries [31], and their involvement in the diameter changes observed here cannot be ruled out, although the magnitude of the dilation we observed is larger than the typical diameter changes associated with pericyte activation [32]. Indeed, previous work showed capillaries downstream from an occluded PA dilate [16], presumably an active process, with diameter changes smaller than those observed here.

Blood flow decreases after small venule strokes may be damaging to brain cells. The extensive blood flow and vascular changes we observed following occlusion of single cortical AVs and SVs suggest that these occlusions may lead to dysfunction in brain cells. Previous work has shown that occlusion of large cortical veins leads to regional reductions in blood flow that causes ischemic infarction [12]. We found that blood flow decreased to about 20% of baseline values within 100 μm of occluded AVs, which is at the level where cellular inhibition of protein synthesis and energy failure begins to occur [33]. These blood flow reductions are not sufficient to cause acute cell death, but, if protracted in time, may lead to brain dysfunction [34]. This conclusion is

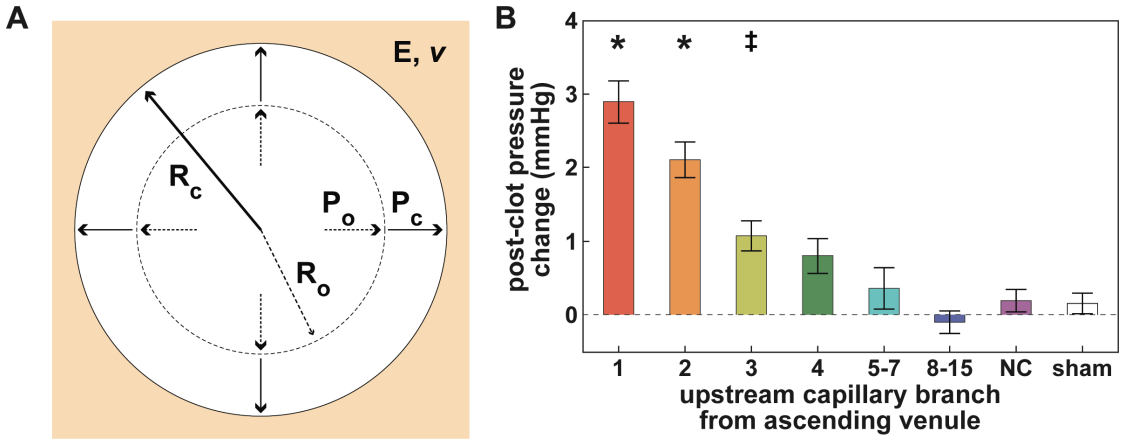

Figure 4.18 Capillary dilations are due to increased internal pressure. A) Schematic of capillary located within the brain tissue that possesses a Young's modulus, E, and Poisson's ratio, ν. At baseline, the initial radius and pressure is R_o and P_o, respectively, both of which increase to R_c and P_c following the clot. **B)** Bar plot of the change (mean ± SEM) in intraluminal pressure as a function of topological connection to the occluded vessel calculated from Eqn. 1 and the mean diameter changes in Figure 3.8. *: $p < 1.0\text{E-}7$, ‡: $p < 0.05$; compared to sham vessels.

supported by studies in the intestinal mesenteric circulation showing that venular occlusion lead to parenchymal cell death that increased with time [35]. Furthermore, changes in vascular wall shear stress caused by changes in flow speed and direction could promote inflammation and oxidative stress in endothelial cells [36]. Lastly, increased intravascular capillary pressures may lead to increased blood brain barrier permeability [37], which can cause brain edema and inflammation [36,37]. Venous insufficiently has been associated with an increasing number of brain pathologies, ranging from multiple sclerosis to dementia [6,7,9]. Although the role of venous alterations in the pathogenesis of these conditions remains uncertain, the present results demonstrate that venular occlusions have profound and widespread effects on brain microcirculation, highlighting the pathogenic potential of venous insufficiency.

References

1. Kovari E, Gold G, Herrmann FR, Canuto A, Hof PR, Michel JP, Bouras C, Giannakopoulos P. Cortical microinfarcts and demyelination significantly affect cognition in brain aging. Stroke 2004; 35(2):410-414.
2. Mok VC, Wong A, Lam WW, Fan YH, Tang WK, Kwok T, Hui AC, Wong KS. Cognitive impairment and functional outcome after stroke associated with small vessel disease. J Neurol Neurosurg Psychiatry 2004; 75(4):560-566.
3. Vermeer SE, Prins ND, den Heijer T, Hofman A, Koudstaal PJ, Breteler MM. Silent brain infarcts and the risk of dementia and cognitive decline. N Engl J Med 2003; 348(13):1215-1222.
4. Fisher CM. Lacunes: Small, Deep Cerebral Infarcts. Neurology 1965; 15:774-784.
5. Clendenon JL, Phillips CL, Sandoval RM, Fang SF, Dunn KW. Voxx: a PC-based, near real-time volume rendering system for biological microscopy. Am J Physiol-Cell Ph 2002; 282(1):C213-C218.
6. Black S, Gao F, Bilbao J. Understanding white matter disease: imaging-pathological correlations in vascular cognitive impairment. Stroke 2009; 40(3 Suppl):S48-52.
7. Moody DM, Brown WR, Challa VR, Anderson RL. Periventricular Venous Collagenosis - Association with Leukoaraiosis. Radiology 1995; 194(2):469-476.
8. Putnam TJ. Lesions of "encephalomyelitis" and multiple sclerosis - Venous thrombosis as the primary alteration. J Amer Med Assoc 1937; 108:1477-1480.
9. Singh AV, Zamboni P. Anomalous venous blood flow and iron deposition

in multiple sclerosis. J Cerebr Blood F Met 2009; 29(12):1867-1878.

10. Ungersbock K, Heimann A, Kempski O. Cerebral blood flow alterations in a rat model of cerebral sinus thrombosis. Stroke 1993; 24(4):563-569; discussion 569-570.
11. Nakase H, Kempski OS, Heimann A, Takeshima T, Tintera J. Microcirculation after cerebral venous occlusions as assessed by laser Doppler scanning. J Neurosurg 1997; 87(2):307-314.
12. Nakase H, Nagata K, Ohtsuka H, Sakaki T, Kempski O. An experimental model of intraoperative venous injury in the rat. Skull Base Surg 1997; 7(3):123-128.
13. Ueda K, Nakase H, Miyamoto K, Otsuka H, Sakaki T. Impact of anatomical difference of the cerebral venous system on microcirculation in a gerbil superior sagittal sinus occlusion model. Acta Neurochir (Wien) 2000; 142(1):75-82.
14. Vogel A, Noack J, Huttman G, Paltauf G. Mechanisms of femtosecond laser nanosurgery of cells and tissues. Appl Phys B-Lasers O 2005; 81(8):1015-1047.
15. Nishimura N, Schaffer CB, Friedman B, Lyden PD, Kleinfeld D. Penetrating arterioles are a bottleneck in the perfusion of neocortex. Proc Natl Acad Sci U S A 2007; 104(1):365-370.
16. Nishimura N, Rosidi NL, Iadecola C, Schaffer CB. Limitations of collateral flow after occlusion of a single cortical penetrating arteriole. J Cerebr Blood F Met 2010; 30(12):1914-1927.
17. Nishimura N, Schaffer CB, Friedman B, Tsai PS, Lyden PD, Kleinfeld D. Targeted insult to subsurface cortical blood vessels using ultrashort laser pulses: three models of stroke. Nat Methods 2006; 3(2):99-108.

18. Schaffer CB, Friedman B, Nishimura N, Schroeder LF, Tsai PS, Ebner FF, Lyden PD, Kleinfeld D. Two-photon imaging of cortical surface microvessels reveals a robust redistribution in blood flow after vascular occlusion. Plos Biol 2006; 4(2):258-270.
19. Kurokawa Y, Hashi K, Okuyama T, Uede T. Regional Ischemia in Cerebral Venous Hypertension Due to Embolic Occlusion of the Superior Sagittal Sinus in the Rat. Surg Neurol 1990; 34(6):390-395.
20. Zhang SX, Murphy TH. Imaging the impact of cortical microcirculation on synaptic structure and sensory-evoked hemodynamic responses in vivo. Plos Biology 2007; 5(5):1152-1167.
21. Srinivasan VJ, Atochin DN, Radhakrishnan H, Jiang JY, Ruvinskaya S, Wu W, Barry S, Cable AE, Ayata C, Huang PL, Boas DA. Optical coherence tomography for the quantitative study of cerebrovascular physiology. J Cereb Blood Flow Metab 2011.
22. Chen BR, Bouchard MB, McCaslin AF, Burgess SA, Hillman EM. High-speed vascular dynamics of the hemodynamic response. Neuroimage 2011; 54(2):1021-1030.
23. Frerichs KU, Deckert M, Kempski O, Schurer L, Einhaupl K, Baethmann A. Cerebral Sinus and Venous Thrombosis in Rats Induces Long-Term Deficits in Brain-Function and Morphology - Evidence for a Cytotoxic Genesis. J Cerebr Blood F Met 1994; 14(2):289-300.
24. Watson BD, Dietrich WD, Busto R, Wachtel MS, Ginsberg MD. Induction of reproducible brain infarction by photochemically initiated thrombosis. Ann Neurol 1985; 17(5):497-504.
25. Miyake K, Takeo S, Kaijihara H. Sustained Decrease in Brain Regional Blood-Flow after Microsphere Embolism in Rats. Stroke 1993; 24(3):415-

420.

26. Blinder P, Shih AY, Rafie C, Kleinfeld D. Topological basis for the robust distribution of blood to rodent neocortex. Proc Natl Acad Sci U S A 2010; 107(28):12670-12675.
27. Rhodin JA. Ultrastructure of mammalian venous capillaries, venules, and small collecting veins. J Ultrastruct Res 1968; 25(5):452-500.
28. Fung YC, Zweifach BW, Intaglie.M. Elastic Environment of Capillary Bed. Circ Res 1966; 19(2):441-&.
29. Gefen A, Gefen N, Zhu QL, Raghupathi R, Margulies SS. Age-dependent changes in material properties of the brain and braincase of the rat. J Neurotraum 2003; 20(11):1163-1177.
30. Lipowsky HH. Microvascular rheology and hemodynamics. Microcirculation 2005; 12(1):5-15.
31. Peppiatt CM, Howarth C, Mobbs P, Attwell D. Bidirectional control of CNS capillary diameter by pericytes. Nature 2006; 443(7112):700-704.
32. Fernandez-Klett F, Offenhauser N, Dirnagl U, Priller J, Lindauer U. Pericytes in capillaries are contractile in vivo, but arterioles mediate functional hyperemia in the mouse brain. Proc Natl Acad Sci U S A 2010; 107(51):22290-22295.
33. Mies G, Ishimaru S, Xie Y, Seo K, Hossmann KA. Ischemic Thresholds of Cerebral Protein-Synthesis and Energy-State Following Middle Cerebral-Artery Occlusion in Rat. J Cerebr Blood F Met 1991; 11(5):753-761.
34. Iadecola C. The overlap between neurodegenerative and vascular factors in the pathogenesis of dementia. Acta Neuropathol 2010; 120(3):287-296.
35. Takase S, Delano FA, Lerond L, Bergan JJ, Schmid-Schonbein GW. Inflammation in chronic venous insufficiency: is the problem

insurmountable? J Vasc Res 1999; 36:3-10.

36. Harrison DG, Widder J, Grumbach I, Chen W, Weber M, Searles C. Endothelial mechanotransduction, nitric oxide and vascular inflammation. J Intern Med 2006; 259(4):351-363.
37. Mayhan WG, Faraci FM, Heistad DD. Disruption of the blood-brain barrier in cerebrum and brain stem during acute hypertension. Am J Physiol 1986; 251(6 Pt 2):H1171-1175.
38. Gold G, Giannakopoulos P, Herrmann FR, Bouras C, Kovari E. Identification of Alzheimer and vascular lesion thresholds for mixed dementia. Brain 2007; 130:2830-2836.

Chapter 5

Pre-ictal and ictal neurovascular and metabolic coupling

This chapter investigates cerebral blood flow changes and metabolic activity before and during focally initiated seizures. We show, for the first time, that surface arterioles demonstrate pre-ictal vasoconstriction in the surrounding regions of the seizure focus. This work was in collaboration with Ted Schwartz, a neurosurgeon at Cornell Weill Medical College, and Mingrui Zhao, a postdoc in Ted's lab. The following text contains the entire study as I thought it would put my contribution in better context. My specific contribution to the study was using two-photon excited fluorescence (2PEF) microscopy to investigate vessel diameter dynamics before, during and after seizure activity, shown in Figure 5.4-5.7.

At the time of writing this dissertation, the following study was accepted into the *Journal of Neuroscience*. The expected citation should resemble the following:

Mingrui Zhao, John Nguyen, Hongtao Ma, Nozomi Nishimura, Chris B. Schaffer, Theodore H. Schwartz: Pre-ictal and ictal neurovascular and metabolic coupling surrounding a seizure focus. *J. Neuro*, 2011.

5.1 The epileptic focus

Neurovascular and neurometabolic coupling are critical to supply the energy demands of brain tissue during both normal physiological function and pathological conditions such as epilepsy [1,2]. Early investigators have shown dramatic increases in cerebral blood flow (CBF) and metabolism in the

epileptic focus during seizure initiation and propagation in a variety of animal models, originally using techniques such as autoradiography and more recently in humans with single photon emission computed tomography, positron emission tomography (PET), functional magnetic resonance imaging (fMRI) and intrinsic optical signal (IOS) imaging [3-8]. Pre-ictal hemodynamic events have also been described, which may precede seizures by anywhere from 20 minutes to a few seconds, showing promise as a technique for identifying seizure onsets [4,9]. However, little attention has been paid to neurovascular and neurometabolic coupling and pre-ictal activity in the area of cortex surrounding the epileptic focus during seizures. The "surround" of an epileptic focus was originally identified in interictal animal models of epilepsy, using penicillin injection or other $GABA_A$ antagonists, as an area of intense neuronal inhibition, presumed to prevent the transition to ictal onset [10]. This so called "inhibitory surround", however, was not commonly found during ictal events, except in *in vitro* models where feed-forward inhibition was shown to act as a "veto" mechanism to limit seizure spread [11].

Hemodynamic techniques also show profound inverted signals in the cortex surrounding an ictal event, indicating decreases in CBF and cerebral blood volume (CBV) [12,13]. Studies of cortical metabolism such as PET or autoradiography, however, do not routinely show hypometabolism in the cortex surrounding the seizure focus [14]. In our previous studies of acute seizures, we have demonstrated a transient decrease in CBF and CBV around an ictal focus, accompanied by an increase in tissue oxygenation [13]. The etiology of this short drop in perfusion was unclear. In this current study we examined whether the decrease in CBF and CBV around a seizure focus was accompanied by a decrease in cortical metabolism. We also examined whether

the decrease in CBF and CBV is caused by a passive shunting of blood into the ictal focus, i.e. a steal phenomenon caused by vasodilation in the focus, or by active shunting of blood due to vasoconstriction in the surrounding brain. Finally we studied the timing of these processes with the goal of identifying pre-ictal neurovascular or neurometabolic events in the surround that may elucidate mechanisms for seizure initiation. We found that metabolism is decreased in the cortex surrounding a seizure focus and discovered a new phenomenon, namely pre-ictal vasoconstriction in a ring of cortex surrounding the seizure focus, which actively shunts blood to the ictal focus and may serve to prepare the focus for the impending dramatic increase in neuronal activity and metabolism. The significance and possibly etiologies of this new finding are discussed.

5.2 Experimental methods

Refer to Chapter 3.5 for general surgical procedures and optical setup.

Epileptogenesis and Electrophysiology. Ictal discharges were induced by injecting 0.5 μl of 4-aminopyridine (4-AP, Sigma), with a concentration 15 mM, through a single-barreled glass microelectrode using a Nanoject II injector (Drummond Scientific) [12,13,15-17]. Extracellular local field potential (LFP) was recorded either with the same electrode or a second single-barreled glass microelectrode (impedance, 2-4 MΩ) filled with saline, positioned <1 mm from the 4-AP electrode and lowered to a depth of 300~500 μm into the neocortex. The signal was amplified and filtered between 0.1 and 500 Hz using a DAB-S system (World Precision Instruments, Sarasota, FL), and digitized at 1000 Hz by a CED Power 1401 (Cambridge Electronic Design). Data was

recorded using Spike2 software (Cambridge Electronic Design).

Laser Doppler flowmetry. One custom angled stainless steel laser Doppler flowmetry (LDF) probe was placed on the cortex, avoiding large blood vessels (wavelength, 780nm; fiber separation, 0.25 μm; Perimed AB). The probe was placed to close as possible to the 4-AP electrode (heretofore referred to as the "focus") or >2 mm away from the electrode (heretofore referred to as the "surround"). Nine rats and eight rats were used in the focus experiment and the surround experiment, respectively. LDF provides continuous hemodynamic monitoring of red blood cell velocity and red cell concentration yielding a calculated CBF measure that correlates with traditional methods [18]. CBF was continuously recorded by the PeriFlux System 5000 (Perimed AB). Data was acquired at 200 Hz with a 0.05 s time constant using a CED Power 1401 and Spike2 software.

Tissue oxygenation. Tissue oxygenation was measured with one Clark-style polarographic oxygen microsensor, which responds linearly to tissue oxygen concentration changes. The tip of the microsensor is 25 μm in diameter with a 90% response time of <0.5 s. The tip measures a sphere of tissue approximately 60 μm in diameter. Calibrations were performed at 37 ^{o}C in saline equilibrated with either bubbling air (atmospheric pO_2) or 100% N_2 gas (zero pO_2) before each experiment. The oxygen microelectrode was inserted ~400 μm deep into the neocortex, close as possible to the 4-AP injection site ("focus") or >2 mm away ("surround"). In both cases, the oxygen microsensor was placed as close as possible to the LDF probe. The signal was measured with a high impedance picoammeter (PA 2000, Unisense A/S) and recorded to

the computer by a CED Power 1401 and Spike2 software. An off-line 0.3 Hz low-pass filter was used to remove the artifacts caused by spatial displacement [19,20].

Oxygen consumption. Cerebral metabolic rate of oxygen ($CMRO_2$) was calculated from CBF and pO_2 measurements as described by Gjedde [21] and Thomsen [22]. The relationship between the three variables is

$$tP_{O_2} = P_{50}\sqrt[h]{\left(\frac{2C_a CBF}{CMRO_2}\right) - 1} - \left(\frac{CMRO_2}{2L}\right) \qquad \text{(Eq. 5.1)}$$

Where tPO_2 is the tissue oxygen tension, P_{50} is the half-saturation tension of the oxygen–hemoglobin dissociation curve, h is the Hill coefficient of the same dissociation curve, C_a is the arterial oxygen concentration, and L is the effective diffusion coefficient of oxygen in brain tissue. The value of L was determined from baseline values of rats in similar conditions of anesthesia in which CBF and $CMRO_2$ were reported in the literature to be 0.53 ml/g/min and 2.19 μmol/g/min [23]. The corresponding value of L was 5.45 μmol/g/min/mmHg for standard values of P_{50} (36 mmHg), h (2.7), and C_a (8 μmol/ml).

Intrinsic optical spectroscopic imaging. The exposed cortical surface was illuminated with one of two different wavelengths (570 ± 10 nm and 810 ± 30 nm) light. Reflected light from the cortical surface was collected by a 50 mm camera lens and divided into two separate paths using a dichroic beamsplitter. Each light beam passed through a second 50 mm camera lens. The reflectance at 570 nm provides a measurement of CBV. At 800 nm, the optical signal is largely derived from changes in light scattering related to cell

swelling as well as intra- and extracellular fluid shifts, which provide an indirect representation of neuronal activity [24]. Images were acquired at 10 Hz (Imager 3001, Optical Imaging Inc.) as previously described [13]. Intrinsic imaging was performed in 5 rats at each wavelength.

Autofluorescence flavoprotein Imaging (AFI). AFI is a non-hemodynamic measure of cellular metabolism derived from the fluorescence of flavoproteins associated with the electron transport chain in mitochondria. We imaged flavoprotein autofluorescence using a band-pass excitation filter (455 ± 35 nm), an extended reflectance dichroic mirror (500 nm), and a 515 nm long-pass emission filter [25], on the same imaging system described above. A total of 5 rats were used in the intrinsic and AFI imaging experiment.

2PEF microscopy of surface cortical vasculature. *In vivo* images of cortical vasculature were obtained with a custom built 2PEF fluorescence microscope using low-energy, 100 fs, 800 nm, 76 MHz repetition rate laser pulses produced by a Titanium:Sapphire oscillator (Mira-HP; Coherent) that was pumped by a continuous wave laser (Verdi-V18; Coherent). Laser scanning and data acquisition was controlled using MPSCOPE software [26]. To help navigate and map the entire cranial window we used a 0.28 numerical aperture (NA), 4x magnification, air objective (Olympus). For high-resolution imaging and vessel diameter measurements, we used a 0.95 NA, 20x magnification, water-immersion, objective (Olympus). High-resolution movies (3.39 frames per second) of vessels were obtained to track diameter changes during seizure activity. Four rats were used for vessel diameter measurements.

Data analysis. The offline analysis was performed using custom analysis software written in Matlab (MathWorks). Since ictal events can have a varying electrographic morphology, we only analyzed those that had no interictal spikes during the 20s prior to the ictal onset and that began with a large population spike followed by a recruiting rhythm to eliminate any confusion regarding the onset of the seizure (Figure 5.1B). Seizure onset was determined by visual analysis of the LFP from the initial negative deflection of the large spike that preceded all seizures [13]. $CMRO_2$ data were converted to percent change (Δ) from baseline by subtracting then dividing the average baseline value obtained over a 2 s block of time prior to the onset of the ictal discharge. The tracing was analyzed starting 20 s prior to the electrographic onset of the seizure to evaluate pre-ictal activity. The magnitude of the response was estimated as the area under the curve above (positive) or below (negative) two standard deviations from the pre-event baseline.

Reflectance changes at 800 nm and 570 nm were expressed in percentage of a negative change from the baseline ($-\Delta R/R$), while flavoprotein autofluorescence is expressed in percentage of fluorescence change from the baseline ($\Delta F/F$). Response time courses were extracted from 0.5 mm concentric rings centered on the focus of the 4-AP seizure. We used concentric rings at a predetermined distance to avoid selection bias resulting from placing a region of interest (ROI) by hand (Figure 5.1A). Each frame following the onset of each seizure and for 20 s before onset, was divided by an average of the 20 frames (2 s) prior to the onset. The amplitude of the response was shown as positive or negative based on whether the signal rose or decreased either above or below a threshold set at two standard deviations from the pre-

event 2 sec baseline. An average of percent fractional changes of optical signal, positive peak, and negative peak at each time point of optical signal inside each of 0.5mm ring were used for further analysis.

For analysis of two-photon image data, Matlab code was developed to calculate diameter changes in individual blood vessels. For each vessel, an ROI was placed over the vessel and its boundary determined using a threshold (20% of maximum intensity). The diameter was then calculated as the average width across the length of the selected region. A trend line of diameter changes was calculated at baseline and during seizure activity. To determine whether the measured vessel elicited a significant response, we calculated the 99% confidence interval about the mean of baseline activity prior to seizure onset. We then use the upper and lower bounds of the confidence interval as threshold values for dilation and constriction, respectively. The dilation or constriction onset is the time point at which the diameter trend line exceeds the threshold values (Figure 5.6A). If the trend line does not exceed the bound limit, then the vessel was deemed to not elicit the respective vascular response to the seizure activity. As described above, a distinct spike in the LFP recording determined seizure onset. For boxplots, circles indicate individual data points while cross hairs are considered statistical outliers, which were not included when calculating the mean. Horizontal red and black lines represent the mean and median, respectively.

For most data, statistical significance was determined with ANOVA and post-hoc tests comparing the baseline mean measurement of results averaged over all seizures in all animals. A Mann-Whitney U test was performed on data shown in Figure 5.7C. All data were expressed as means ± standard error of mean (SEM).

5.3 Results

We studied neurovascular and metabolic activity before and during seizure activity using several optical techniques. Intrinsic optical signal imaging was used to measure CBV and fluid shifts in the tissue. Autofluorescence detections of flavoprotein provided nonhemodynamic measurements of cellular metabolism. Laser Doppler flowmetry provided CBF measurements that enabled $CMRO_2$ calculations. Lastly, we used 2PEF microscopy to measure changes in vessel diameter during seizure activity.

5.3.1 Acute focal 4-AP seizures

Acute focal seizures were elicited with injection of 4-AP. These seizures typically began with a large negative spike followed by a low amplitude fast activity which evolved into rapid spike-and-wave activity that gradually increased in periodicity and decreased in amplitude until the seizure terminated (Figure 5.1B).

5.3.2 Light scattering and CBV imaging of center-surround dynamics

Optical recording at 800 nm demonstrated an antagonistic center-surround dynamic (Figure 5.1C). The complex, dynamic relationship between the positive signal in the focus and the negative signal in the surround evolved over the course of the seizure. For the purposes of data analysis, we chose two moments in time that were representative of the predominant interaction, namely the time point at which the positive signal in the seizure focus was at its maximum, an average of 36.5 ± 8.6 s after seizure initiation and the time point at which the negative signal in the seizure surround was at its maximum, an average of 11.6 ± 9.3 s after seizure initiation. Average data over

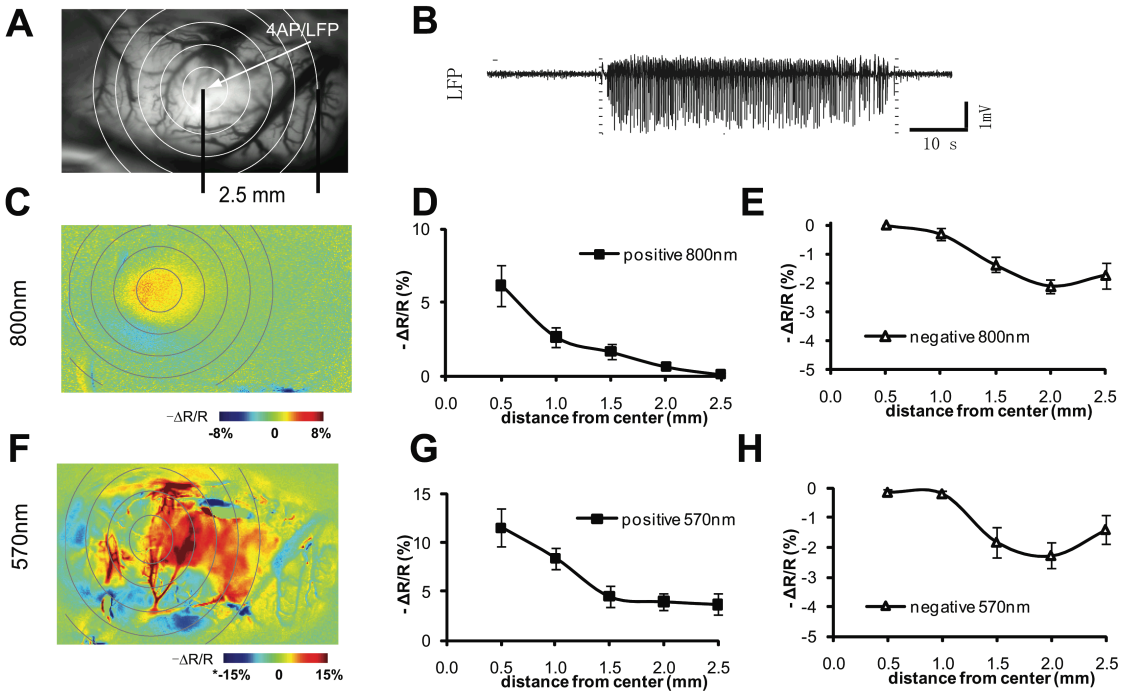
A
4AP/LFP
2.5 mm
B
LFP
1mV
10 s
C
800nm
−ΔR/R
-8%
0
8%
D
positive 800nm
- ΔR/R (%)
distance from center (mm)
E
negative 800nm
- ΔR/R (%)
distance from center (mm)
F
570nm
−ΔR/R
*-15%
0
15%
G
positive 570nm
- ΔR/R (%)
distance from center (mm)
H
negative 570nm
- ΔR/R (%)
distance from center (mm)

Figure 5.1

Figure 5.1. Light scatter and CBV measurements during seizure. A) Image of cortical surface (570nm) to demonstrate location of 4-AP and LFP electrode (white arrow). Concentric rings spaced 0.5 mm around the focus were used to examine positive and negative signal changes. **B)** LFP recording of one seizure. The dotted lines showed the onset (left) and offset (right) of seizure. **C)** Typical 800 nm maps shows an increase in the optical signal in the ictal focus and decrease in the surround at the time of the maximal amplitude in the positive signal in the focus indicating a "center-surround" effect in neuronal activity. **D)** Average positive signal response (n=5 rats, 11 seizures) decreases with distance from the focus. **E)** Average negative signal response at the time of its maximum shows that a smaller negative signal reaches its peak ~2 mm from the focus, in the surrounding cortex. **F)** Typical 570nm map shows a similar "center-surround" dynamic for CBV change but with a more widespread, irregular increase in CBV in the focus with an irregular decrease in CBV in the surround. **G)** Average increase in CBV (n=5 rats, 18 seizures) at its peak is maximal in the focus and falls off with distance. **H)** Average decrease in CBV at the time of its minimum occurs at ~2 mm from the ictal focus. Error bar: SEM.

all experiments revealed that the positive signal diminished in amplitude with increasing distance from the seizure focus (Figure 5.1D, n=5 rats, 11 seizures). The maximum amplitude of the positive signal in the focus was 6.2 ± 1.3%. Statistical testing revealed a significant decline in the positive signal within each ring to a value of 0.14 ± 1.0% in the last ring at 2.5 mm ($p<0.001$). The inverted, negative signal in the surrounding cortex, on the other hand, was largest at a distance of 2.0 mm from the focus with a maximum amplitude of -2.1 ± 0.2%, which was also statistically different from the values in other rings ($p<0.001$, Figure 5.1E). Although not a direct measure of neuronal activity, the signal indirectly represents increases in neuronal activity in the focus and decreases in neuronal activity in the surround by measuring mostly changes in light scattering in the tissue (see Methods).

Optical recording at 570 nm provided a map of CBV during seizure activity (Figure 5.1F), nearly identical to those previously published by our group [13]. The 570 nm map revealed a similar center-surround effect as seen with the 800 nm data but the activity was less focal and had more vascular artifact, which was not seen in the 800 nm data (Figure 5.1F). The maximal increase in CBV in the focus was 11.5 ± 1.9%, which decreased with distance but did not reach baseline, even 2.5 mm from the focus ($p<0.001$; Figure 5.1G, n=5 rats, 18 seizures). A decrease in CBV in the surround was also identified with a maximum change of -2.3 ± 0.4% peaking at 2.0 mm from the focus ($p<0.01$, Figure 5.1H). Hence, CBV maps provide an indirect and less spatially precise measurement of excitatory and inhibitory pattern of neuronal activity, as indirectly measured by as compared with those measured with light scatter changes (Figure 5.1C–5.1E), and clearly show a decrease in CBV surrounding a seizure focus. The etiology of this negative signal in the surround and its

timing with respect to the seizure onset was then investigated in further detail. Of note, using intrinsic signal imaging in this acute seizure model, we did not find any pre-ictal increase or decrease in either light reflection or CBV during a 20 s window before seizure onset.

5.3.3 Metabolic mapping of center-surround dynamics.

In a previous paper using laser Doppler flowmetry (LDF), we showed that the decrease in CBV surrounding the 4-AP focus was accompanied by a transient decrease in CBF, followed by a later increase in CBF as the seizure propagated horizontally [13]. Tissue oxygenation in the surround, on the other hand, increased throughout the duration of the seizure [13]. Although we assumed that a drop in blood flow and an increase in tissue oxygenation would be associated with a decrease in oxygen metabolism from neuronal inhibition, having not directly measured metabolism, the possibility remained that the increase in activity in inhibitory interneurons would result in an increase in metabolism, or that only a fraction of the pyramidal cells would be inhibited while others would increase their activity, resulting in a net increase or no change in metabolism. To address this question, we first investigated metabolism using autofluorescence imaging (AFI) of flavoproteins, so as to sample large areas of the cortex simultaneously including both the seizure focus and the surround (n=5 rats). With this technique, we could also determine if the resulting maps of seizure onset were more focal than hemodynamic maps, since the signal arises purely from local mitochondria rather than non-local vascular supply [25,27-29].

AFI measured changes in the redox state of mitochondrial flavoproteins, primarily flavin adenine dinucleotide (FAD), since its oxidized form (FAD+) is

more fluorescent than the reduced form FADH [27]. Increases in neuronal activity result in increases in intracellular Ca^{+} and depletion of ATP and production of ADP, which leads to a reduction in the proton gradient across the inner mitochondrial membrane and an increase in flavoprotein fluorescence [25,30]. Similar to AFI of normal sensory processing, we found that the signal was biphasic, having an early oxidation phase i.e. "light phase" (Figure 5.2A), arising from neuronal oxidative metabolism, followed by a later, more prolonged reduction phase i.e. "dark phase" (Figure 5.2D and 5.2G), presumably arising from a combination of glycolysis in astrocytes and contamination from increased CBV and the intrinsic signal [31,32]. However, certain aspects of the AFI maps showed that epileptic events differ from normal physiologic sensory responses. In the early light phase (~0-2 sec), the maximal positive AFI peak occurred in the focus with an amplitude of 1.5 ± 0.3% and decreased with towards the periphery ($p<0.001$, Figure 5.2B). Unlike normal physiologic responses to sensory stimulation in the neocortex, we identified an inhibited surround with a peak negative AFI of -0.9 ± 0.3% ($p<0.01$, Figure 5.2C). The strong positive AFI signals were centered between 0 and 1.0 mm, while the smaller negative AFI signal were between 1.5 and 2.5 mm. As the seizure progressed, the signal inverted and a decrease in AFI of -3.3 ± 0.9% was recorded in the focus and a peak increase of 1.9 ± 0.3% ($p<0.001$) was recorded in the surround (Figure 5.2E and 5.2F). In the late part of the dark phase (>5 s), the negative signal in the focus reached -6.2 ± 1.4% while the positive peak in the surround decreased to a maximum of 0.9 ± 0.2% ($p<0.001$, Figure 5.2H and 5.2I). These findings confirm an early increase in metabolism in the epileptic focus, consistent with the dip in hemoglobin and tissue oxygenation, or "initial dip" previously demonstrated in this model.

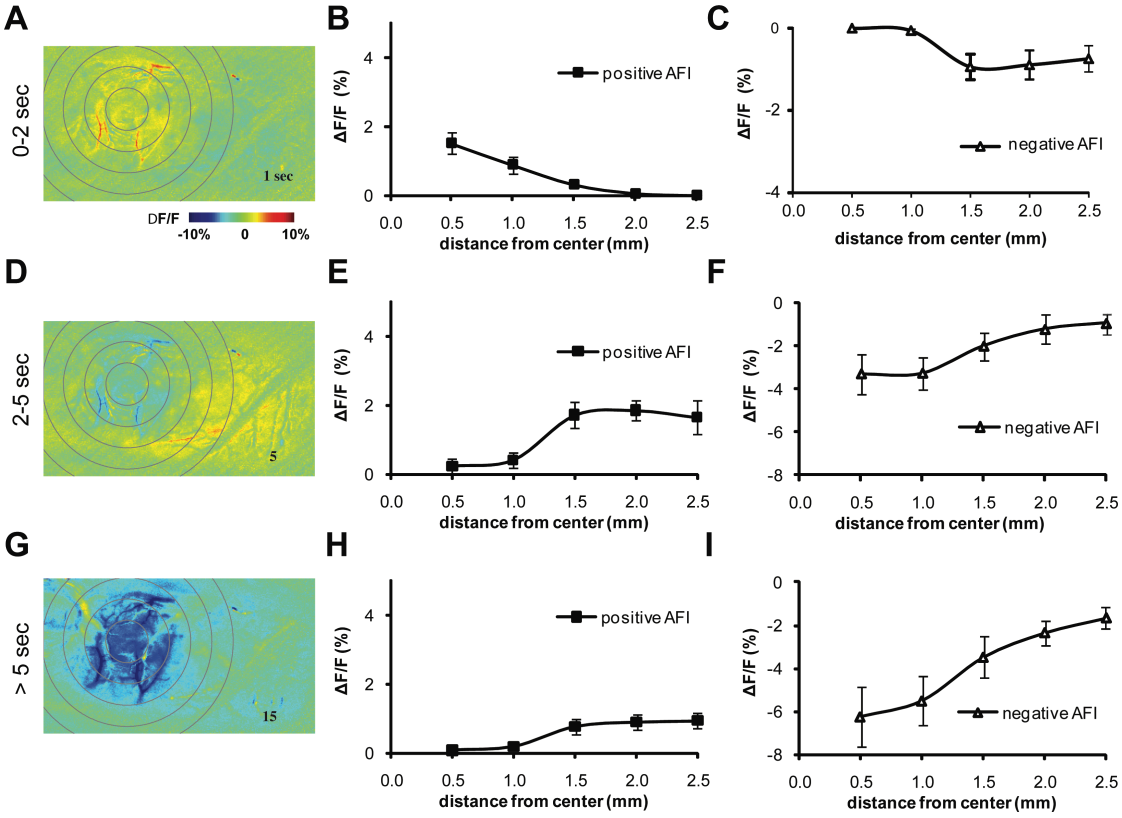
A
0-2 sec
1 sec
DF/F
-10%
0
10%
B
positive AFI
ΔF/F (%)
distance from center (mm)
C
negative AFI
ΔF/F (%)
distance from center (mm)
D
2-5 sec
5
E
positive AFI
ΔF/F (%)
distance from center (mm)
F
negative AFI
ΔF/F (%)
distance from center (mm)
G
> 5 sec
15
H
positive AFI
ΔF/F (%)
distance from center (mm)
I
negative AFI
ΔF/F (%)
distance from center (mm)

Figure 5.2

Figure 5.2 Cellular and metabolic changes in focus and surround. A) Flavoprotein autofluorescence images (AFI) at selected time points after seizure onset in a single animal reveal biphasic signal with a center-surround effect during the early "light" phase. **B)** The average amplitude of the positive signal during the first 2 sec after seizure onset shows an increase in oxidative metabolism in the focus. **C)** Average amplitude of the negative signal shows a small decrease in oxidative metabolism in the surround. **D)** AFI after seizure onset at early "dark" phase. **E)** Between 2 and 5 s after seizure onset, there is an inversion in the signal with an increase in fluorescence in the surround. **F)** The center-surround effect is seen at this time period also showing a decrease in fluorescence in the focus. **G)** AFI after seizure onset at the later "dark" phase. As the seizure progresses (5-40 s), the decrease in fluorescence in the focus increases in amplitude **H)** and the increase in the surround **I)** diminishes (B-C, E-F, H-I: n=5 rats, 14 seizures). Error bars: SEM.

However, the decrease in AFI during the early light phase surrounding the ictal focus is consistent with a transient decrease in oxidative metabolism in the surround, a newly described phenomenon that is consistent with a decrease in neuronal activity. At later timepoints, interpretation of the etiology of the AFI signal is less clear, resulting from a combination of changes in CBV, which make up a significant proportion of the optical signal at the emission wavelength of AFI, as well as glycolysis in astrocytes, which is the primary component of the later "dark" phase of the AFI signal.

In order to overcome these temporal limitations of AFI, namely overlap between the emission spectrum of AFI and the intrinsic CBV signal at timepoints >2 s, we directly derived tissue oxygen metabolism using simultaneous measurements of CBF and tissue oxygenation in the focus (n=9 rats) and the surround (n=8 rats) and calculated cortical oxygen consumption ($CMRO_2$) using Gjedde's method [21,22]. In the focus, $CMRO_2$ was significantly increased 2.2 s after seizure onset ($p<0.05$) and reached a maximum of 14.7 ± 3.8% ($p<0.001$) compared with the pre-ictal baseline (n=9 rats, 54 seizures, Figure 5.3, top). In the surround region, two different phenomena were identified. In most of the rats, $CMRO_2$ showed a significant sustained decrease by an average of -8.3 ± 2.5% (5 of 8 rats; n=43 seizures; $p<0.05$). In the rest of the animals, we found a transient increase of 6.3 ± 1.3% (1.3 to 3.2 s; $p<0.05$; Figure 5.3, middle) followed by a sustained decrease to -5.7 ± 1.4% (3 of 8 rats; n=39 seizures; $p<0.05$; Figure 5.3, bottom). These results show the expected dramatic increase in metabolism in the focus and confirm the AFI results showing an overall decrease in metabolism in the surround consistent with a net decrease in neuronal activity. However, unlike the AFI results, the measurements of tissue metabolism persist for a longer time

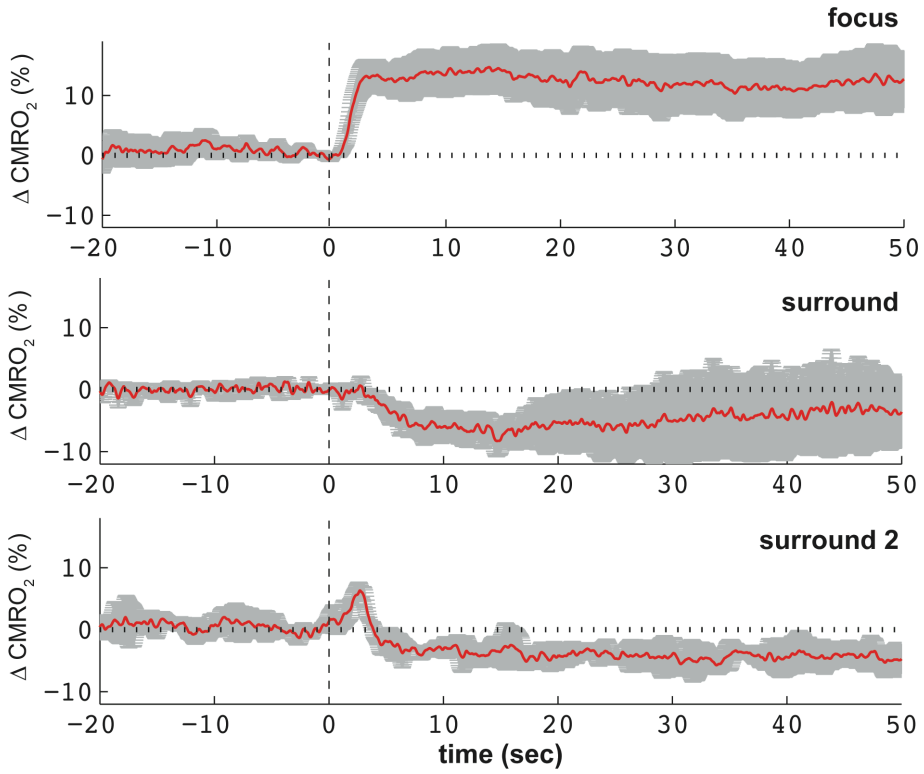

Figure 5.3. **$CMRO_2$ during seizure.** $CMRO_2$ increases in the focus during the ictal discharge (top, n=9 rats, 54 seizures). Two different responses were recorded in the surround. In most animals (middle, n=5 rats, 43 seizures) a decrease in $CMRO_2$ was measured while in other animals (bottom, n=3 rats, 39 seizures) a transient increased was followed by a longer decrease in $CMRO_2$.

period, supporting the correlation between only the early light phase of the AFI data and neuronal metabolism.

5.3.4 Two-photon measurements of arteriolar diameter.

In order to determine the etiology of the transient drop in CBF and CBV in the surround at seizure onset, we measured arteriolar diameter using 2PEF imaging (n=4 rats). Low magnification images were first used to navigate the surface vasculature and determine spatial distances of specific vessels relative to the injection site of the 4-AP (Figure 5.4A). High magnification movies of individual arterioles allowed for tracking diameter changes during seizure activity near (Figure 5.4B and 5.4C) and far (Figure 5.4D and 5.4E) from the seizure focus. We found that arterioles dilated in response to the seizure, with a decreasing amount of dilation with increasing distance from the 4-AP injection site (Figure 5.5A; n=4 rats, 71 vessels, 45 seizures, 143 measurements). Within 2.5 mm of the seizure focus, 97% of the measured arterioles dilated (Figure 5.5B), with diminishing responses further away. For vessels within a 1 mm ring centered on the 4-AP injection site (focus) arterioles dilated by an average of 63 ± 5% of their baseline diameter (Figure 5.5A). In the ring 1.5-2.5 mm from the 4-AP injection site (surround), we observed early vascular constriction followed by delayed dilation in all seizures measured (Figure 5.4E and 5.6A). In this ring, 69% of the vessels displayed this early constriction, with a smaller fraction of vessels dilating for vessels closer or farther from the seizure focus (Figure 5.6B). On average, the vessels in this ring constricted to 7% ± 1% of their baseline diameter during this constriction phase, with smaller constrictions for vessels closer or farther from the seizure focus (Figure 5.6A).

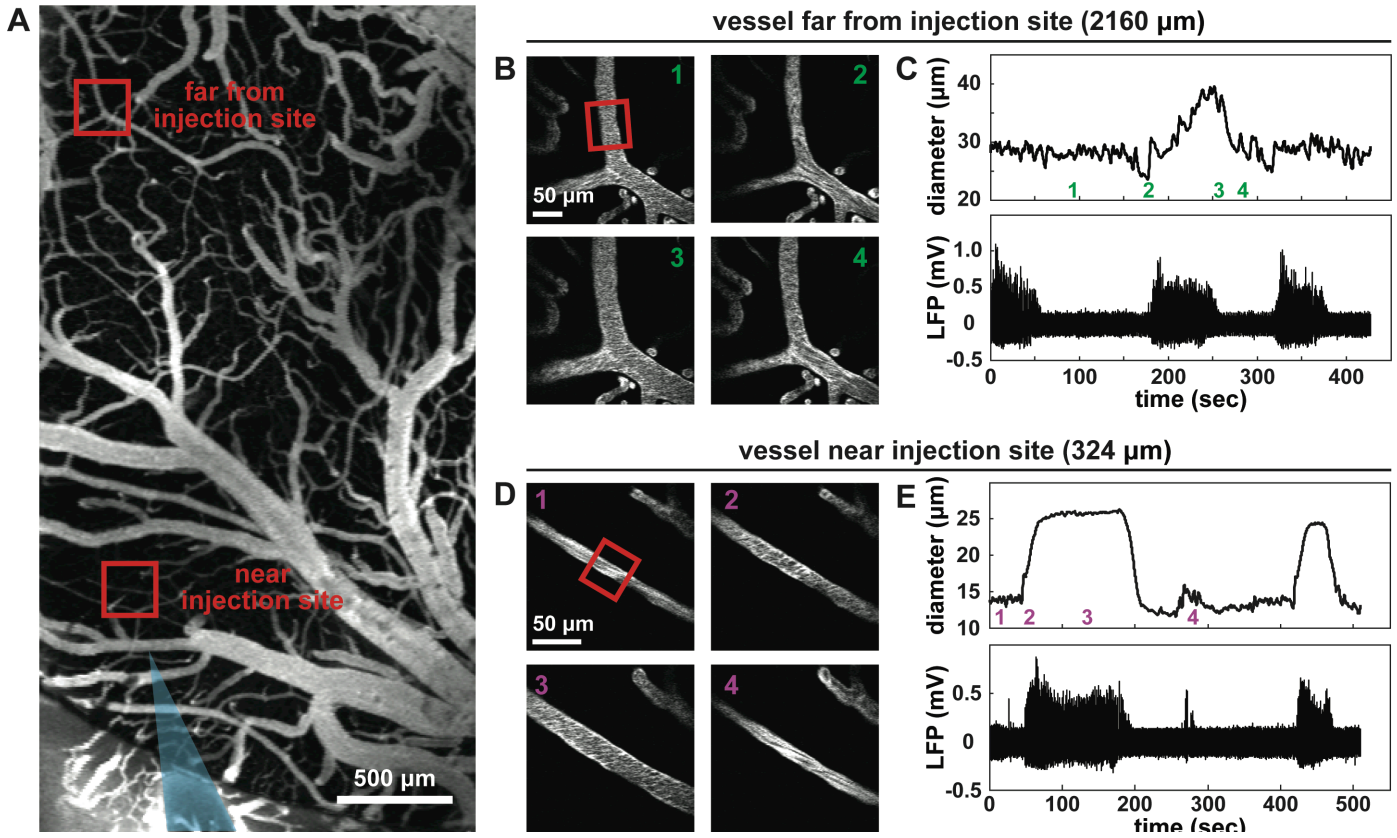
A
far from injection site
near injection site
500 µm
B
1
2
3
4
50 µm
vessel far from injection site (2160 µm)
C
diameter (µm)
40
30
20
1
2
3 4
LFP (mV)
1.0
0.5
0
-0.5
0
100
200
300
400
time (sec)
vessel near injection site (324 µm)
D
1
2
3
4
50 µm
E
diameter (µm)
25
20
15
10
1 2
3
4
LFP (mV)
0.5
0
-0.5
0
100
200
300
400
500
time (sec)

Figure 5.4

Figure 5.4 Seizure-induced vascular changes. A) Two-photon image of fluorescence-labeled surface vasculature. The electrode (blue) is implanted into the brain and vessels near and far (red boxes) from the seizure focus are studied. The vascular responses for these regions are show in panels *B* through *E*. **B)** Two-photon images of a vessel located ~2100 μm from the injection site. Each time stamp corresponds to a time point in panel *C*. Corresponding plot of vessel diameter (top) from panel *B* during ictal events (bottom). Note vascular constriction prior to seizure onset. **D)** Two-photon images of a vessel ~325 μm from the seizure focus. Each time stamp corresponds to a time point in panel *E*. **E)** Corresponding plot of vessel diameter (top) from panel *D* during ictal events (bottom). Note that vascular dilation is concurrent with seizure onset and evolution.

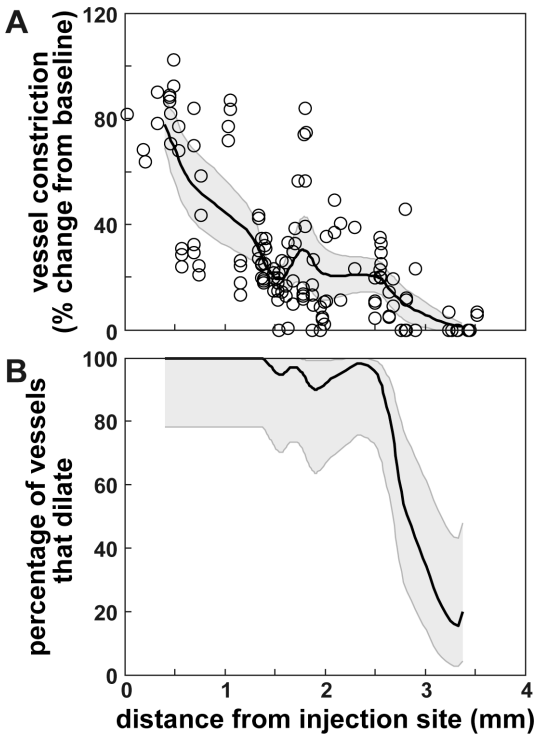

Figure 5.5 Seizures result in spatially dependent arteriole dilations. A) Vessel dilation and **B)** percentage of vessels that dilate as a function distance from the seizure focus. Black lines represent the running mean and fraction for panels *A* and *B*, respectively. Circles represent individual data points. Grey regions represent the 95% confidence interval about the trend line.

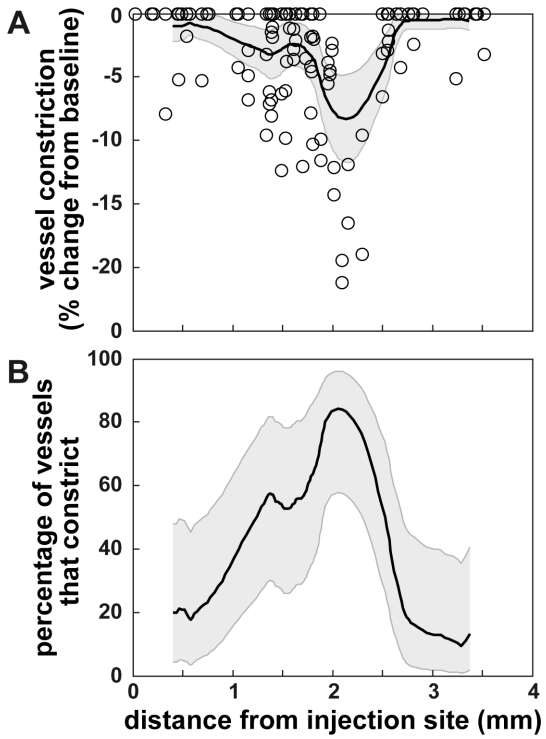

Figure 5.6 Spatially dependent arteriole constrictions A) Vessel constriction and **B)** percentage of vessels that constrict as a function distance from the seizure focus. Black lines represent the running mean and fraction for panels *A* and *B*, respectively. Circles represent individual data points. Grey regions represent the 95% confidence interval about the trend line.

5.3.5 Temporal characteristics of vascular reactivity.

Having demonstrated for the first time that active vascular constriction in the ictal surround occurs, we sought to determine the timing of this event with respect to seizure onset. Plotting the temporal profile of vasodilation compared with vasoconstriction (Figure 5.7A and 5.7B), we determined that vasodilation in the focus occurred 0.5 ± 0.1 s after seizure onset whereas vasoconstriction in the surround occurred 5.3 ± 0.5 s prior to seizure onset (Figure 5.7C) ($p < 1.0E-7$, Mann-Whitney U test). Note that all vasoconstriction was observed to occur prior to seizure onset.

5.4 Discussion

Our data indicate that, in a model of acute rodent seizures, ictal onset is preceded by active vasoconstriction in small arterioles surrounding the ictal focus. As the seizure progresses, tissue and oxidative metabolism increase in the ictal focus and generally decrease in the surround, as do CBV and cell swelling, although transient increases in tissue metabolism can occur in the surround in some seizures. Our data support a model in which a "center-surround" dynamic characterizes both metabolic and neurovascular mechanisms during *in vivo* ictal evolution. In addition, this novel pre-ictal event may be a useful tool for seizure prediction and possible manipulated or capitalized upon for therapeutic effect.

Center-surround phenomena. Epileptic surround inhibition elicited by interictal spikes was thought to be a mechanism to prevent the interictal to ictal transition [10]. Similar surround inhibition has been described during normal cortical processing [33,34] as well as during interictal spike activity

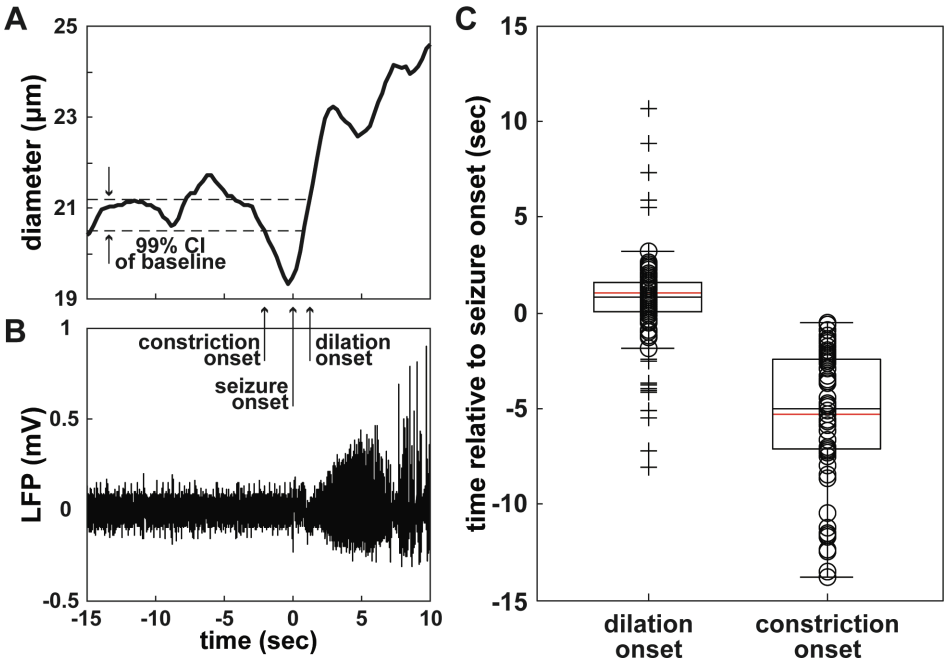

Figure 5.7 Arterioles in surround constrict prior to seizure onset. A) Representative example of vascular diameter and **B)** simultaneous LFP recording of seizure onset demonstrate pre-ictal vasoconstriction and post-ictal vasodilation. A 99% confidence interval about the mean diameter is shown in panel *A*. Arrows indicate constriction (first arrow), seizure onset (second arrow), and dilation (third arrow). **C)** Boxplot of dilation and constriction onset times relative to seizure onset. Red and black lines represent mean and median, respectively. Circles are individual data points and cross hairs are statistical outliers. *: p<1.0E-7. (n = 4 rats, 71 vessels, 45 total seizures, 143 total measurements).

[12]. This finding may be unique to the neocortex and is not found in the cerebellum where perforant pathway stimulation elicits upstream vasodilation of larger arterioles and non-specific widespread increase in CBF [35]. Ictal events are more complicated since they evolve over space and time, through a dynamic interplay of both synchronized and desynchronized excitatory and inhibitory activity, progressing from initiation to propagation to termination as they spread horizontally over the cortex. The concept of surround inhibition has not been well studied during seizures *in vivo*, although evidence of enhanced inhibitory activity around the ictal focus is mentioned in several studies [36]. Ictal surround inhibition does not appear to completely encircle the focus, which is consistent with the "center-surround phenomenon" reported during normal cortical activity [34]. Explanations for such an inhomogeneous response include a mixture of inhibitory and excitatory neuronal activity, potentially a reflection of patchy vascular domains. In this study we show clear evidence of early ictal surround inhibition, revealed with optical mapping of light scattering from cell swelling and CBV, which is further manifested in tissue and cellular metabolism and pre-ictal arteriolar vasoreactivity.

Associated with a decrease in neuronal activity in the ictal surround, we demonstrate a decrease in CBV. The etiology of the widespread decrease in CBV in the surround was hypothesized to arise either from a passive steal phenomenon, as vessels in the focus dilate and redirect oxygenated blood toward the metabolically hyperactive focus [37], or from active shunting of blood through vasoconstriction of vessels in the surround [13]. This latter mechanism has been demonstrated to occur during normal cortical processing. However, surround vasoconstriction during normal cortical

processing occurred *after* physiologic stimulation and after a brief period of vasodilation [34]. In contrast, we report the opposite time profile of dilation and constriction in the surround of an epileptic seizure, namely pre-ictal vasoconstriction followed by vasodilation. Surprisingly, the spatial topography, if not the timing, of the center-surround inversion in vascular reactivity is conserved, when comparing normal sensory processing to ictal events using 2-photon imaging, as well as in studies of the blood oxygen level dependent signal, which also inverts at >2 mm during normal visual processing in the monkey [38]. The conservation of the center-surround effect and its spatial topography in both normal and abnormal physiologic events points to a conserved mechanism. Recent evidence is mounting that vascular reactivity at the arteriolar level is highly influenced by local neurotransmitter and neuropeptide release [39]. Putative mechanisms include release of NO by excitatory neurons causing vasodilation , inhibitory neurotransmitters causing vasoconstriction [39], varying levels of extracellular potassium eliciting vasodilation and vasoconstriction [40], as well as astrocyte and pericyte-mediated vascular reactivity [41,42].

Pre-ictal surround vasoconstriction. Pre-ictal increases and decreases in neuronal activity, and progressive coalescing of high-frequency activity and microseizures have been documented [43]. It is likely that these pre-ictal electrophysiological events are accompanied by alterations in focal hemodynamic responses. However, no pre-ictal decreases in high frequency activity in the surround have been demonstrated, although human single unit recordings have shown a small percentage of neurons may decrease activity during the immediate pre-ictal activity (Truccolo et al. 2011). Indeed, pre-ictal

vascular reactivity was first theorized (mistakenly at the time) to be the etiology for seizure activity as early as 1933 [44]. More recent studies have demonstrated increases in lobar perfusion as early as 20 minutes before focal as well as generalized spike-and-wave events [9]. Likewise, both increases [45] and decreases [46] in tissue oxygenation have been found tens of seconds before seizure onset using fMRI and NIRS. IOS imaging has also demonstrated focal pre-ictal changes in light reflection in animal models and in increases in CBV and decreases in hemoglobin oxygenation in human epileptic cortex almost 20 seconds before seizure onset [4]. However, this is the first report of active pre-ictal vasoconstriction surrounding an ictal focus. Another report of 2PEF imaging of blood flow in and around an epileptic focus used an interictal model and did not report decreases in blood flow in the surround but defined the surround as only > 1 mm from the focus, which may have been an inadequate distance [47]. Our data are consistent with a model of pre-ictal vasoconstriction in the cortex surrounding the ictal focus as crucial for initiating seizure onset. Since we did not perform electrical recordings from the surround, we cannot say if this pre-ictal vascular activity correlates with early decreases in neuronal activity.

Another hypothesis rests on the concept of anticipatory shunting of oxygenated blood to the ictal focus, possibly precipitated by a gradual build-up of excitatory activity. A similar anticipatory increase in CBV has been demonstrated prior to normal cortical processing in visual cortex, the mechanism of which is unknown [48]. However, if the pial arterioles we are imaging around the focus provide blood flow to the focus itself, we would expect a decrease in flow in the focus, which we do not find. Alternatively, the pial arterioles in the surround may only control very local blood flow and

have no influence on blood flow in the focus. This would imply that there is a transient decrease in metabolism in the surround before the seizure begins followed by an increase in metabolism in the focus, however, we did not find any pre-ictal changes in metabolism using AFI and direct tissue measurements, although slight metabolic changes may be below the resolution of our techniques. Finally, there is the more controversial and less likely possibility that the hemodynamic events are primary and the electrographic events secondary. This hypothesis has been raised for both epileptic activity [49] and normal cortical processing [50] whereby hemodynamic fluctuations alter the gain of normal cortical processing through delivery of blood borne messengers and thermal and mechanical modulation of neurons thereby precipitating neuronal activation. Along this line of argument, pre-ictal vasoconstriction would shunt oxygenated blood to the focus, which would then facilitate or directly cause ictal onset. At this time, the mechanistic details of pre-ictal surround vasoconstriction remain unknown. However, the phenomenon may be useful in triggering closed loop abortive therapies and may provide a novel target for therapeutic modulation, although significant pre-clinical work would be required to confirm these events in humans and develop miniaturized implantable devices capable of detecting them.

Ictal metabolism in the focus and surround. In spite of the discovery of pre-ictal surround vasoconstriction, we did not find any evidence of significant pre-ictal alterations in metabolism in either the focus or the surround. Not surprisingly, a clear increase in metabolism was found in the focus. The sustained increase in metabolism in the ictal focus is consistent with prior

work using either autoradiography or PET. Although human PET studies show interictal hypometabolism [51], intense interictal activity causes focal hypermetabolism with surround hypometabolism [52]. Ictal events, on the other hand, always show increases in glucose and oxygen metabolism in the focus [14]. Although AFI imaging has been used extensively to map normal sensory processing [28,29,32], only one prior report exists of AFI imaging of epilepsy [53]. In this study, there was no concurrent electrophysiology and the AFI signal occurred ~75 seconds after audiogenic stimulation, rendering the source of the signals ambiguous. In this paper, we show for the first time that AFI signals are exquisitely sensitive to the ictal onset during the "light" phase of imaging as early as 0-2 seconds after ictal onset. Hence, AFI imaging may be a useful technique for localizing epileptic seizures possibly providing a map for therapeutic intervention that may be more focal than CBV or hemoglobin oxygenation maps derived from the IOS.

Metabolism in the surround of an ictal focus has not been well-studied. Our results provide direct evidence of a drop in tissue metabolism surrounding the ictal focus, which is consistent with the existence of neuronal inhibition in these areas and consistent with *in vivo* models of "feed-forward" or "veto" inhibition shaping the epileptic wavefront as it propagates [11]. Decreased AFI fluorescence in areas of cortex surrounding areas of focal activation have been correlated with neuronal inhibition in the cerebellum [25]. However, AFI imaging of surround metabolism has not yet been reported in the neocortex. Additional evidence for this finding arises from the direct calculations of $CMRO_2$ using Gjedde's method. However, using this technique, in a subset of animals, we found a transient rise in metabolism in the surround, followed by a longer-lasting decrease. One possibility is that

AFI samples large areas in space simultaneously where Gjedde's method is limited by only sampling individual points in space. Another possible explanation is the situation where an unusually large burst of inhibitory interneurons in the surround causes an increase in metabolism that outweighs the decrease in metabolism in the adjacent pyramidal cells for a short period of time, causing a transient increase in metabolism. Nevertheless, an association occurs between metabolism and blood flow in the ictal surround as the seizure evolves.

In summary, we have identified a novel pre-ictal vascular phenomenon, namely surround vasoconstriction. Although the precise etiology of this event is unclear, a transient rise in pre-ictal inhibition, which serves to increase synchronization, is a possible candidate. We have also shown that AFI imaging, particularly during the early "light" phase, is useful at mapping the ictal onset zone and its clinical applications should be explored as has been done with optical imaging of intrinsic signals [4]. Finally, we find support for a center-surround dynamic at play in ictal propagation, lending further support for surround inhibition in shaping the evolving ictal wavefront.

References

1. Raichle ME, Mintun MA. Brain work and brain imaging. Annu Rev Neurosci 2006; 29:449-476.
2. Iadecola C, Nedergaard M. Glial regulation of the cerebral microvasculature. Nature neuroscience 2007; 10(11):1369-1376.
3. Roche-Labarbe N, Zaaimi B, Berquin P, Nehlig A, Grebe R, Wallois F. NIRS-measured oxy- and deoxyhemoglobin changes associated with EEG spike-and-wave discharges in children. Epilepsia 2008; 49(11):1871-1880.
4. Zhao M, Suh M, Ma H, Perry C, Geneslaw A, Schwartz TH. Focal increases in perfusion and decreases in hemoglobin oxygenation precede seizure onset in spontaneous human epilepsy. Epilepsia 2007; 48(11):2059-2067.
5. Benar CG, Gross DW, Wang Y, Petre V, Pike B, Dubeau F, Gotman J. The BOLD response to interictal epileptiform discharges. NeuroImage 2002; 17(3):1182-1192.
6. Folbergrova J, Ingvar M, Siesjo BK. Metabolic changes in cerebral cortex, hippocampus, and cerebellum during sustained bicuculline-induced seizures. Journal of neurochemistry 1981; 37(5):1228-1238.
7. Ingvar M. Cerebral blood flow and metabolic rate during seizures. Relationship to epileptic brain damage. Ann N Y Acad Sci 1986; 462:194-206.
8. Kreisman NR, Magee JC, Brizzee BL. Relative hypoperfusion in rat cerebral cortex during recurrent seizures. J Cereb Blood Flow Metab 1991; 11(1):77-87.
9. Diehl B, Knecht S, Deppe M, Young C, Stodieck SR. Cerebral hemodynamic response to generalized spike-wave discharges. Epilepsia

1998; 39(12):1284-1289.

10. Prince DA, Wilder BJ. Control mechanisms in cortical epileptogenic foci. "Surround" inhibition. Arch Neurol 1967; 16(2):194-202.
11. Trevelyan AJ, Sussillo D, Yuste R. Feedforward inhibition contributes to the control of epileptiform propagation speed. J Neurosci 2007; 27(13):3383-3387.
12. Schwartz TH, Bonhoeffer T. In vivo optical mapping of epileptic foci and surround inhibition in ferret cerebral cortex. Nat Med 2001; 7(9):1063-1067.
13. Zhao M, Ma H, Suh M, Schwartz TH. Spatiotemporal dynamics of perfusion and oximetry during ictal discharges in the rat neocortex. J Neurosci 2009; 29(9):2814-2823.
14. Engel J, Jr., Kuhl DE, Phelps ME. Patterns of human local cerebral glucose metabolism during epileptic seizures. Science 1982; 218(4567):64-66.
15. Motamedi GK, Salazar P, Smith EL, Lesser RP, Webber WR, Ortinski PI, Vicini S, Rogawski MA. Termination of epileptiform activity by cooling in rat hippocampal slice epilepsy models. Epilepsy Res 2006; 70(2-3):200-210.
16. Rensing N, Ouyang Y, Yang XF, Yamada KA, Rothman SM, Wong M. In vivo imaging of dendritic spines during electrographic seizures. Ann Neurol 2005; 58(6):888-898.
17. Xu L, Rensing N, Yang XF, Zhang HX, Thio LL, Rothman SM, Weisenfeld AE, Wong M, Yamada KA. Leptin inhibits 4-aminopyridine- and pentylenetetrazole-induced seizures and AMPAR-mediated synaptic transmission in rodents. J Clin Invest 2008; 118(1):272-280.
18. Skarphedinsson J, Harding H, Thoren P. Repeated measurements of cerebral blood flow in rats. Comparison between hydrogen clearance

method and laser Doppler Flowmetry. Acta Physiol Scand 1983; 134:133-142.

19. Masamoto K, Omura T, Takizawa N, Kobayashi H, Katura T, Maki A, Kawaguchi H, Tanishita K. Biphasic Changes in Tissue Partial Pressure of Oxygen Closely Related to Localized Neural Activity in Guinea Pig Auditory Cortex. J Cereb Blood Flow Metab 2003; 23(9):1075-1084.
20. Offenhauser N, Thomsen K, Caesar K, Lauritzen M. Activity-induced tissue oxygenation changes in rat cerebellar cortex: interplay of postsynaptic activation and blood flow. J Physiol 2005; 565(Pt 1):279-294.
21. Gjedde A. Blood-Brain Transfer and Metabolism of Oxygen. In: Dermietzel R, Spray DC, Nedergaard M, eds. Blood-brain barriers : from ontogeny to artificial interfaces. Weinheim: Wiley-VCH. 2006:2 v. (xxxii, 741 p.).
22. Thomsen K, Piilgaard H, Gjedde A, Bonvento G, Lauritzen M. Principal cell spiking, postsynaptic excitation, and oxygen consumption in the rat cerebellar cortex. J Neurophysiol 2009; 102(3):1503-1512.
23. Zhu XH, Zhang Y, Tian RX, Lei H, Zhang N, Zhang X, Merkle H, Ugurbil K, Chen W. Development of (17)O NMR approach for fast imaging of cerebral metabolic rate of oxygen in rat brain at high field. Proc Natl Acad Sci U S A 2002; 99(20):13194-13199.
24. Salzberg BM, Obaid AL, Gainer H. Large and rapid changes in light scattering accompany secretion by nerve terminals in the mammalian neurohypophysis. J Gen Physiol 1985; 86(3):395-411.
25. Reinert KC, Gao W, Chen G, Ebner TJ. Flavoprotein autofluorescence imaging in the cerebellar cortex in vivo. J Neurosci Res 2007; 85(15):3221-3232.

26. Nguyen QT, Tsai PS, Kleinfeld D. MPScope: a versatile software suite for multiphoton microscopy. J Neurosci Methods 2006; 156(1-2):351-359.
27. Chance B, Schoener B, Oshino R, Itshak F, Nakase Y. Oxidation-reduction ratio studies of mitochondria in freeze-trapped samples. NADH and flavoprotein fluorescence signals. J Biol Chem 1979; 254(11):4764-4771.
28. Husson TR, Mallik AK, Zhang JX, Issa NP. Functional imaging of primary visual cortex using flavoprotein autofluorescence. J Neurosci 2007; 27(32):8665-8675.
29. Shibuki K, Hishida R, Murakami H, Kudoh M, Kawaguchi T, Watanabe M, Watanabe S, Kouuchi T, Tanaka R. Dynamic imaging of somatosensory cortical activity in the rat visualized by flavoprotein autofluorescence. J Physiol 2003; 549(Pt 3):919-927.
30. Llano DA, Theyel BB, Mallik AK, Sherman SM, Issa NP. Rapid and sensitive mapping of long-range connections in vitro using flavoprotein autofluorescence imaging combined with laser photostimulation. J Neurophysiol 2009; 101(6):3325-3340.
31. Kasischke KA, Vishwasrao HD, Fisher PJ, Zipfel WR, Webb WW. Neural activity triggers neuronal oxidative metabolism followed by astrocytic glycolysis. Science 2004; 305(5680):99-103.
32. Sirotin YB, Das A. Spatial Relationship between Flavoprotein Fluorescence and the Hemodynamic Response in the Primary Visual Cortex of Alert Macaque Monkeys. Front Neuroenergetics 2010; 2:6.
33. Derdikman D, Hildesheim R, Ahissar E, Arieli A, Grinvald A. Imaging spatiotemporal dynamics of surround inhibition in the barrels somatosensory cortex. J Neurosci 2003; 23(8):3100-3105.
34. Devor A, Tian P, Nishimura N, Teng IC, Hillman EM, Narayanan SN,

Ulbert I, Boas DA, Kleinfeld D, Dale AM. Suppressed neuronal activity and concurrent arteriolar vasoconstriction may explain negative blood oxygenation level-dependent signal. J Neurosci 2007; 27(16):4452-4459.

35. Iadecola C, Yang G, Ebner TJ, Chen G. Local and propagated vascular responses evoked by focal synaptic activity in cerebellar cortex. Journal of neurophysiology 1997; 78(2):651-659.
36. Bragin A, Mody I, Wilson CL, Engel J, Jr. Local generation of fast ripples in epileptic brain. J Neurosci 2002; 22(5):2012-2021.
37. Hirase H, Creso J, Buzsaki G. Capillary level imaging of local cerebral blood flow in bicuculline-induced epileptic foci. Neuroscience 2004; 128(1):209-216.
38. Shmuel A, Augath M, Oeltermann A, Logothetis NK. Negative functional MRI response correlates with decreases in neuronal activity in monkey visual area V1. Nature neuroscience 2006; 9(4):569-577.
39. Hamel E. Perivascular nerves and the regulation of cerebrovascular tone. J Appl Physiol 2006; 100(3):1059-1064.
40. Filosa JA, Bonev AD, Straub SV, Meredith AL, Wilkerson MK, Aldrich RW, Nelson MT. Local potassium signaling couples neuronal activity to vasodilation in the brain. Nature neuroscience 2006; 9(11):1397-1403.
41. Peppiatt CM, Howarth C, Mobbs P, Attwell D. Bidirectional control of CNS capillary diameter by pericytes. Nature 2006; 443(7112):700-704.
42. Wang X, Lou N, Xu Q, Tian G-F, Peng WG, Han X, Kang J, Takano T, Nedergaard M. Astrocytic Ca2+ signaling evoked by sensory stimulation in vivo. Nature neuroscience 2006; 9(6):816-823.
43. Litt B, Esteller R, Echauz J, D'Alessandro M, Shor R, Henry T, Pennell P, Epstein C, Bakay R, Dichter M, Vachtsevanos G. Epileptic seizures may

begin hours in advance of clinical onset: a report of five patients. Neuron 2001; 30(1):51-64.

44. Gibbs FA. Cerebral blood flow preceding and accompanying experimental convulsions Arch Neurol Psychiat Chicago 1933; 30:1003-1010.
45. Makiranta M, Ruohonen J, Suominen K, Niinimaki J, Sonkajarvi E, Kiviniemi V, Seppanen T, Alahuhta S, Jantti V, Tervonen O. BOLD signal increase preceeds EEG spike activity--a dynamic penicillin induced focal epilepsy in deep anesthesia. NeuroImage 2005; 27(4):715-724.
46. Hoshi Y, Tamura M. Cerebral oxygenation state in chemically-induced seizures in the rat--study by near infrared spectrophotometry. Adv Exp Med Biol 1992; 316:137-142.
47. Hirase H, Qian L, Bartho P, Buzsaki G. Calcium dynamics of cortical astrocytic networks in vivo. PLoS Biol 2004; 2(4):E96.
48. Sirotin YB, Das A. Anticipatory haemodynamic signals in sensory cortex not predicted by local neuronal activity. Nature 2009; 457(7228):475-479.
49. Hawco CS, Bagshaw AP, Lu Y, Dubeau F, Gotman J. BOLD changes occur prior to epileptic spikes seen on scalp EEG. NeuroImage 2007; 35(4):1450-1458.
50. Moore CI, Cao R. The hemo-neural hypothesis: on the role of blood flow in information processing. J Neurophysiol 2008; 99(5):2035-2047.
51. Franck G, Sadzot B, Salmon E, Depresseux JC, Grisar T, Peters JM, Guillaume M, Quaglia L, Delfiore G, Lamotte D. Regional cerebral blood flow and metabolic rates in human focal epilepsy and status epilepticus. Adv Neurol 1986; 44:935-948.
52. Bruehl C, Witte OW. Cellular activity underlying altered brain

metabolism during focal epileptic activity. Ann Neurol 1995; 38:414-420.

53. Takao T, Murakami H, Fukuda M, Kawaguchi T, Kakita A, Takahashi H, Kudoh M, Tanaka R, Shibuki K. Transcranial imaging of audiogenic epileptic foci in the cortex of DBA/2J mice. Neuroreport 2006; 17(3):267-271.

Chapter 6
Laser cuts in rat cortex

This chapter presents a method to produce sub-surface cortical cuts in the brain of a live, anesthetized rodent. We characterize the cut width and maximum cutting depth as a function of laser energy. Quantification of the data allowed us to develop a model that allowed for future predictions of cut widths for a given laser energy and tissue depth. This technique is later employed in studies to halt seizure propagation (presented in Chapter 7).

This work is published in *Lasers in Surgery and Medicine*. The citation is:

John Nguyen, Jillian Ferdman, Mingrui Zhao, David Huland, Shatha Saqqa, Jan Ma, Nozomi Nishimura, Theodore H. Schwartz, Chris B. Schaffer: Sub-Surface, Micrometer-Scale Incisions Produced in Rodent Cortex using Tightly-Focused Femtosecond Laser Pulses. *Lasers in Surgery and Medicine,* 43:382–391, 2011.

6.1 Sub-surface targeting of biological structures

Tools that enable the disruption of targeted structures in the bulk of a biological tissue without affecting the overlying structures or causing collateral damage outside the targeted volume could open the door to new surgical procedures. Radio-frequency and ultrasound ablation enable sub-surface incisions, but have a spatial precision of centimeters to millimeters, respectively [1,2]. Mechanical tools, such as scalpels, can achieve higher cutting precision, but incisions must start at a tissue surface. What is lacking is a technique that provides spatial precision comparable to or better than a

mechanical scalpel, with the ability to disrupt sub-surface structures and preserve the overlying tissue.

Nonlinear optical absorption can enable fine-scale, sub-surface disruption in biological tissue. In most biological samples, linear absorption of near-infrared light is weak, so this light can penetrate deeply into the tissue. Focusing femtosecond-duration pulses of near-infared light at high numerical aperture into the bulk of the tissue produces high intensities that can drive nonlinear absorption of the laser energy in the focal volume. Multiphoton and tunneling ionization produce initial ionized electrons which then linearly absorb laser energy and impact ionize other electrons, a process called avalanche ionization [3]. When using lower energy pulses from high-repetition rate laser sources in the MHz range, tissue damage from this nonlinear absorption is likely dominated by cumulative photochemical damage [4] and heat accumulation [5]. In contrast, when using higher energy pulses from lower repetition rate laser sources of around 1 kHz, damage is largely driven by vaporization of tissue components in the focal volume and subsequent mechanical effects, such as cavitation [4,6]. In this regime, sufficient ionization occurs to cause optical breakdown and plasma formation, vaporizing material in the focal volume. The subsequent expansion of the vaporized material leads to the formation of a cavitation bubble and the launch of a propagating pressure wave [4,7]. The maximal expansion of this cavitation bubble determines the volume of tissue that is disrupted. In both of these regimes, because nonlinear absorption of the laser energy is localized within the focal volume, tissue disruption can be confined to micrometer-sized volumes, while leaving the surrounding tissue intact.

Several studies have used femtosecond laser ablation to disrupt biological

structures in a variety of *in vitro* preparations and *in vivo* animal experiments, as well as in humans. Single chromosomes in human cells have been dissected, providing a technique for noninvasive gene inactivation [8] and single cell and sub-cellular disruptions permitted studies that elucidated the functional neural architecture [9] and mechanisms of neural regeneration [10] in *C. elegans*. Ablation of single cells in drosophila embryos was used to study the role of mechanical forces in development [11], while targeting of sub-cellular structures, such as cytoskeletal filaments, in live cells provided insight into the regulation of mechanical stiffness [12,13]. Additionally, femtosecond laser pulses have been used to selectively perforate cellular membranes for DNA transfection [14,15]. Femtosecond lasers are now also routinely used to produce sub-surface cuts in cornea as a means to produce the "flap" necessary for laser-assisted *in situ* keratomileusis for vision correction surgery [16]. In all these examples, the samples are almost completely transparent and have little to no optical scattering, making the delivery of focused femtosecond pulses to sub-surface regions relatively straightforward. As long as there is not strong linear absorption of the light, however, this approach to producing sub-surface disruption should also be feasible in scattering tissues. Scattered light cannot contribute to nonlinear absorption and has minimal effects on the tissue, so the laser energy incident on the sample can be increased to compensate for scattering losses and deliver the necessary energy to the focus to cause optical breakdown in the depth of the tissue. For example, previous work has show it is possible to produce sub-surface ablation in keratinized corneal and scleral tissue, where the tissue is optically scattering [17]. Additionally, rodent models of small stroke have been developed using femtosecond laser ablation to trigger clotting in individually targeted, cortical

blood vessels that are located several hundred micrometers in the depth of scattering brain tissue [18]. In other work, individual dendrites were cut from pyramidal neurons in live mouse brain, illustrating the precision possible with femtosecond laser ablation, even in scattering tissue [19].

Here, we used tightly-focused femtosecond pulses as a light scalpel to make sub-surface incisions in *in vivo* rodent brain, a scattering biological tissue. We demonstrated our ability to produce sub-surface cuts by ablating the cortex in the rostral-caudal direction. We then produced vertical cuts to determine cut width and maximum achievable ablation depth as a function of laser energy. We used these results to construct a phenomenological model that predicts the laser energy that should be chosen to achieve a given cut size at a given cortical depth. Overall, we describe a technique that allows ablation of biological structures that lie below the surface of a scattering tissue with cell-level precision.

6.2 Experimental methods

Data were acquired from seven male Sprague-Dawley rats (275-350g). Two rats were used to produce sub-surface, horizontal ablations at constant depths with fixed laser energy (Figures 6.1 and 6.2). The remaining rats were used to study depth-dependent cut width and maximum ablation depth as a function of laser energy (Figures 6.3-6.6). Refer to Chapter 3.5 for general surgical procedures and optical setup

2PEF microscopy. High resolution, 2PEF images were obtained to demonstrate sub-surface cuts (Figure 6.1B and 6.7). Large 2PEF surface vasculature maps were obtained to help locate vertical cuts that were used to

determine the cut width and depth dependence on laser energy (Figure 6.3B).

Femtosecond laser sub-surface ablation. To make cuts, the animal was translated at 50 μm/s either horizontally or vertically relative to the cortex surface, depending on the study, while continuously irradiating with the 1-kHz pulse train. At this translation speed, approximately 20 pulses are deposited in each volume along the cut. For horizontal cuts, translation occurred at constant depth (Figure 6.1A and 6.2). For vertical cuts (Figure 6.3A), laser light was focused more than 1 mm into the cortex, and the animal was vertically translated until the focus neared the surface of the brain. For vertical cuts, about 15-20 cuts were placed in each animal in an irregular grid that avoided large blood vessels using laser energies of 0.3, 5, and 13 μJ (Figure 6.3B). At the two higher energies, irradiation was halted about 200 μm below the brain surface to prevent rupturing of large surface vessels.

Post-mortem histology. At the conclusion of each experiment, animals were euthanized and were perfused with 100 ml PBS followed by 100 ml 4% (wt/vol) paraformaldehyde in PBS. Brains were extracted and post-fixed in 4% paraformaldehyde for at least 24 hours. Brains were then cryoprotected using 25% (wt/vol) sucrose in PBS followed by 50% sucrose in PBS [20]. Prior to cryosectioning, fiducial marks were placed at the edges of the cranial window to help map and locate cuts. The brain was then embedded in a cryomold with Optimal Cutting Temperature Compound (O.C.T. Compound, Tissue-Tek), frozen in dry ice, and cut into 20-μm thick coronal sections on a cryostat (HM 505 E, Microm). Slices were stained with 3,3'-diaminobenzidine (DAB) to detect red blood cells as well as hematoxylin and eosin (H&E) to

view tissue structure.

Vertical cut measurement and data analysis. Slides were imaged and examined using an upright microscope (BX41 with DP70 camera; Olympus). Coronal sections gave cross-sectional views of cone-shaped, red blood cell-filled cuts. The fiduciary marks and the in vivo two photon images were used as guides to help identify specific laser cuts observed in serial brain slices (Figures 6.3B and 6.3C). For each tissue section that contained a specific cut the width was measured as a function of depth, and this was repeated for every cut. At each depth beneath the cortical surface, the largest width for each specific cut found across all sections that included that cut was used for data analysis. This ensured that the width of the cut was measured at the widest point at each depth. At higher laser energies, cut widths were measured in 100-μm depth increments. Additionally, the maximum cut depth was recorded for each cut. Cut width as a function of depth for each laser energy and the maximum cut depth as a function of laser energy were fitted to quantify trends. For statistical analysis, means were calculated for each binned group as well a 95% confidence interval (CI) about the mean.

Dissection of neuronal dendrites in a transgenic mouse. We used a 31-g, male, transgenic mouse that expressed yellow fluorescent protein (YFP) in a subset of pyramidal neurons (C57B/6-thy1-YFPH, Jackson Labs) [21] to evaluate structural changes following transections of neural processes using femtosecond laser ablation. The dendritic projections of excitatory pyramidal neurons are imaged in the supragranular layers of the cortex in this mouse line (Figure 6.7A). Surgical methods were similar to those described above,

with slight modifications. The mouse was anesthetized with 5% inhaled isofluorane, and maintained at approximately 1.25%. We performed a bilateral craniotomy that was sealed with a glass coverslip, leaving the dura intact. To visualize the vasculature, we performed a retro-orbital injection of ~0.4 ml of 2.5% (wt/vol) Texas Red-conjugated dextran (D-1830; Invitrogen) in saline. A 1-mm long medial-lateral cut was produced at a depth of 70 μm with an incident laser energy of ~0.2 μJ in parietal cortex (Figure 6.7).

6.3 Results

We demonstrated the use of femtosecond laser ablation to produce sub-surface cuts in the cortex of live, anesthetized rodents. 2PEF microscopy was used to monitor cutting in real-time *in vivo*. The cuts were quantified through histological analyses of brain slices. Cut width and maximum achievable ablation depth were measured as a function of laser energy.

6.3.1 Localized cuts below the brain surface

Two-photon imaging was used to image before, during, and after a sub-surface femtosecond laser cut was produced in the rostral-caudal direction through the cortex of an anesthetized rat with a craniotomy (Figure 6.1A). Projections of 2PEF image stacks showed that the surface vasculature (labeled with intravenously injected fluorescein-dextran) was maintained after a horizontal laser cut (Figure 6.1B, left). The cut was apparent as a ~75-μm wide fluorescent band in the depth of the tissue, not seen in the baseline image (Figure 6.1B, middle). This band was due to fluorescently labeled blood plasma that leaked from the transiently ruptured capillaries that were located along the path of the sub-surface cut. A *y-z* projection of the vasculature

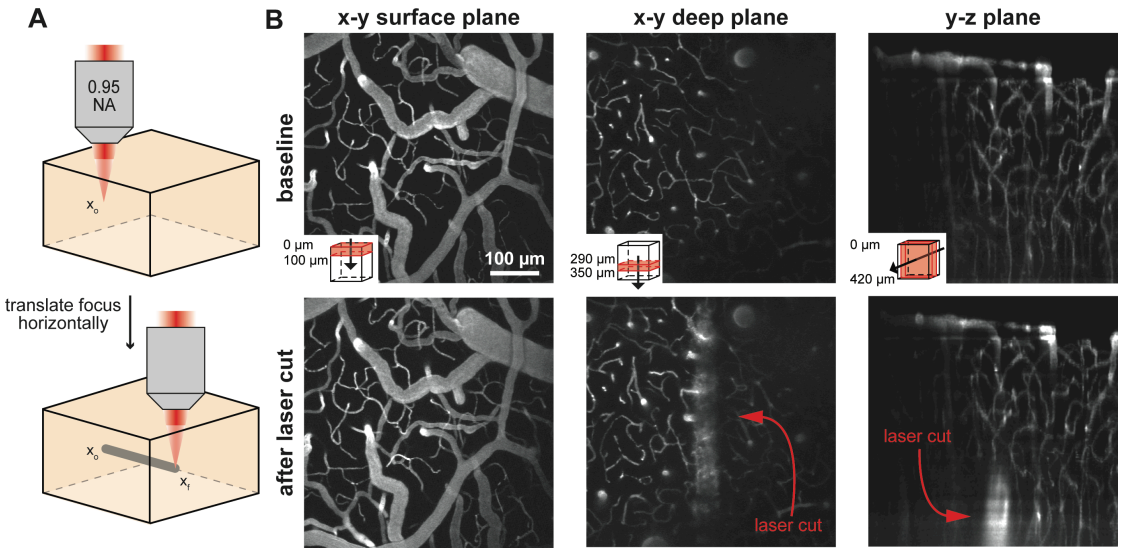
A
0.95
NA
x_o
translate focus
horizontally
x_o
x_f
B
x-y surface plane
x-y deep plane
y-z plane
baseline
after laser cut
0 µm
100 µm
100 µm
290 µm
350 µm
0 µm
420 µm
laser cut
laser cut

Figure 6.1

Figure 6.1 Sub-surface cuts in rat cortex *in vivo* A) Sub-surface cuts were produced by tightly focusing high-energy, femtosecond laser pulses into the cortex of a live, anesthetized rat, through a craniotomy and translating the rat in the horizontal direction at a constant depth. **B)** Average projections of two-photon image stacks of fluorescently labeled cortical vasculature at baseline (top) and after laser cut (bottom). Corner schematics indicate direction and volume of projections. The cut was produced with 4.5-μJ laser pulse energy, focused to a depth of approximately 350 μm. Centered around the cut is an approximately 75-μm band of labeled blood plasma from capillaries ruptured during the cutting (middle, bottom). The post-cut images were acquired approximately five minutes after the cut was produced.

showed that the cut was confined to a volume below the surface of the brain, with the tissue above still intact (Figure 6.1B, right).

Histological studies confirmed our ability to produce sub-surface cuts with micrometer precision in the rat cortex. Red blood cells (stained by DAB) were evident in the tissue, confirming that there was some bleeding into the laser cut (Figure 6.2A). The width of cuts depended on the laser energy and depth below the cortical surface. In the example of Figure 6.2A, three cuts were made with a laser energy of 0.5 μJ near the brain surface that served as guides to help identify a deeper, smaller cortical cut generated with an energy of 3 μJ. Although the laser energy used for the deeper cut was higher compared to the energy used for the shallower cuts, the cut size was smaller due to exponential decay of laser energy as light was focused deeper into the optically scattering brain tissue. A higher magnification view of the 700-μm deep cut showed a 25-μm cut size and an accumulation of red blood cells in the ablated area (Figure 6.2B). Because the capillary density is high in the cortex, we found that laser cuts always ruptured enough capillaries to fill the cylinder-shaped ablated volume with red blood cells. Hematoxylin and eosin staining was used to inspect the surrounding tissue, which appeared intact with very little to no cellular pathology outside the deeper laser cut (Figure 6.2B). The larger, shallower cuts showed some hematoxylin destaining in a band around the cut, suggesting cells around the cut volume were damaged when a laser energy that was high for the depth beneath the surface was used.

6.3.2 Cut width and depth dependence on laser energy

To determine dependence of the cut width on cortical depth and laser

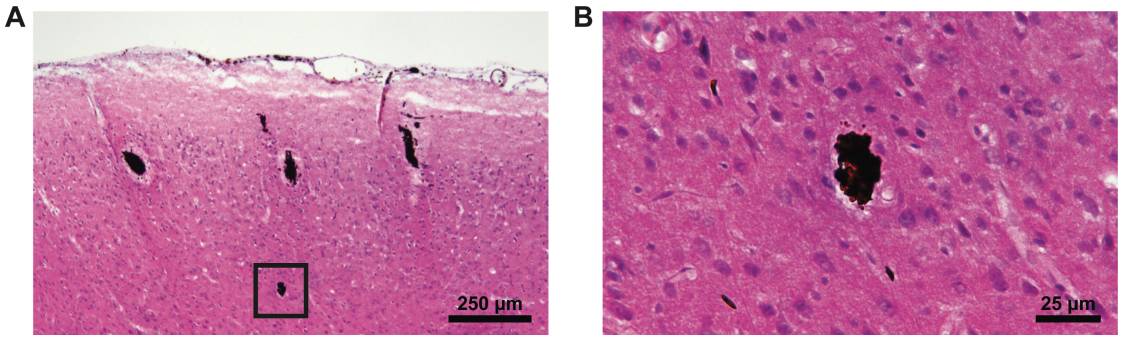

Figure 6.2 H&E and DAB stained brain slices with sub-surface cuts. A) H&E and DAB (for red blood cells) stained 20-μm thick coronal brain slice with sub-surface ablations. Three cuts, produced approximately 300 μm below the surface of the brain with 0.5-μJ laser energy, serve as markers to identify a single cut made at approximately 700 μm below the brain surface with 3-μJ laser energy. **B)** Higher magnification view of the deeper cut from panel *A* (boxed).

energy as well as the dependence of the maximum ablation depth on laser energy, we produced vertical cuts using different laser energies and analyzed the size of the cuts as a function of depth with histology (Figure 6.3A). The location of individual cuts were noted on 2PEF images of the surface vasculature (Figure 6.3B) and were mapped to the damage tracts observed in H&E and DAB stained coronal histological sections (Figure 6.3C).

We found that for fixed laser energy, the cut width increased as the laser focus was vertically translated from deeper to shallower in the cortex (Figures 6.4A-6.4C). For each cut, the width was measured as a function of depth, with the cut width taken to be the maximum width across all serial slices containing a given cut at a particular depth. We found that for all energies, cut widths decreased exponentially with increasing depths. For example, at laser energy of 13 μJ, widths decreased from 158 μm ± 43.1 (mean ± standard deviation) to 56 μm ± 33 for depths of 200 to 800 μm, respectively. Averaging across all cuts, we found about 50% variation in cut width at a fixed depth and laser energy. Because the maximal extent of the tissue disruption should depend on the maximal size the laser-produced cavitation bubble reaches, the volume of the tissue disrupted should scale approximately linearly with the laser energy deposited into the focal region by nonlinear absorption [4]. For pulse energies above the breakdown threshold, the fraction of the pulse energy that is deposited by nonlinear absorption increases slowly with pulse energy [3]. Thus the width of the laser cut should scale as the cube root of the laser energy that reaches the focus unscattered, which is an exponential function of depth beneath the cortical surface. We thus fit the measured cut width, w, as a function of depth, d, for multiple cuts at each laser energy to

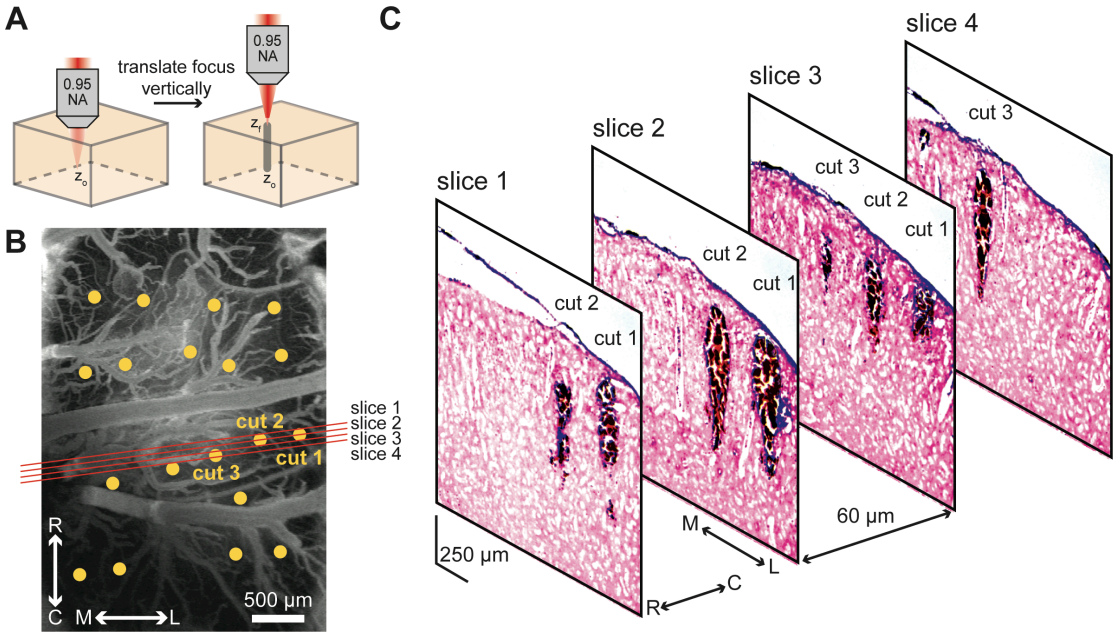
A
0.95 NA
translate focus vertically
0.95 NA
z_f
z_o
z_o
B
cut 2
cut 1
cut 3
slice 1
slice 2
slice 3
slice 4
R
C
M
L
500 µm
C
slice 1
slice 2
slice 3
slice 4
cut 2
cut 1
cut 2
cut 1
cut 3
cut 2
cut 1
cut 3
250 µm
M
L
R
C
60 µm

Figure 6.3

Figure 6.3 Vertical cuts are identified with stained serial slices A) Schematic of vertical sub-surface ablation. High intensity, femtosecond laser pulses were tightly focused into the brain through a craniotomy, and cuts were made by vertically translating the animal, starting deep within the cortex. **B)** *In vivo* two-photon image of fluorescently labeled surface vasculature. Yellow dots represent locations where sub-surface cuts were produced. Red lines correspond to histological brain slices in (c). The brain was sliced at a tilt due to the angled mounting of the brain on the cryostat. R: rostral, C: caudal, M: medial, L: lateral. **C)** Serial images of every fourth 20-μm thick brain slice stained with H&E and DAB. Cuts labeled one, two, and three correspond to labeled cut locations in (b). Slices one through three reveal the beginning, middle, and end cross-section views of the damage caused by cuts one and two. Slice three shows a beginning cross-section view of cut three, with a middle cross-section view in slice four.

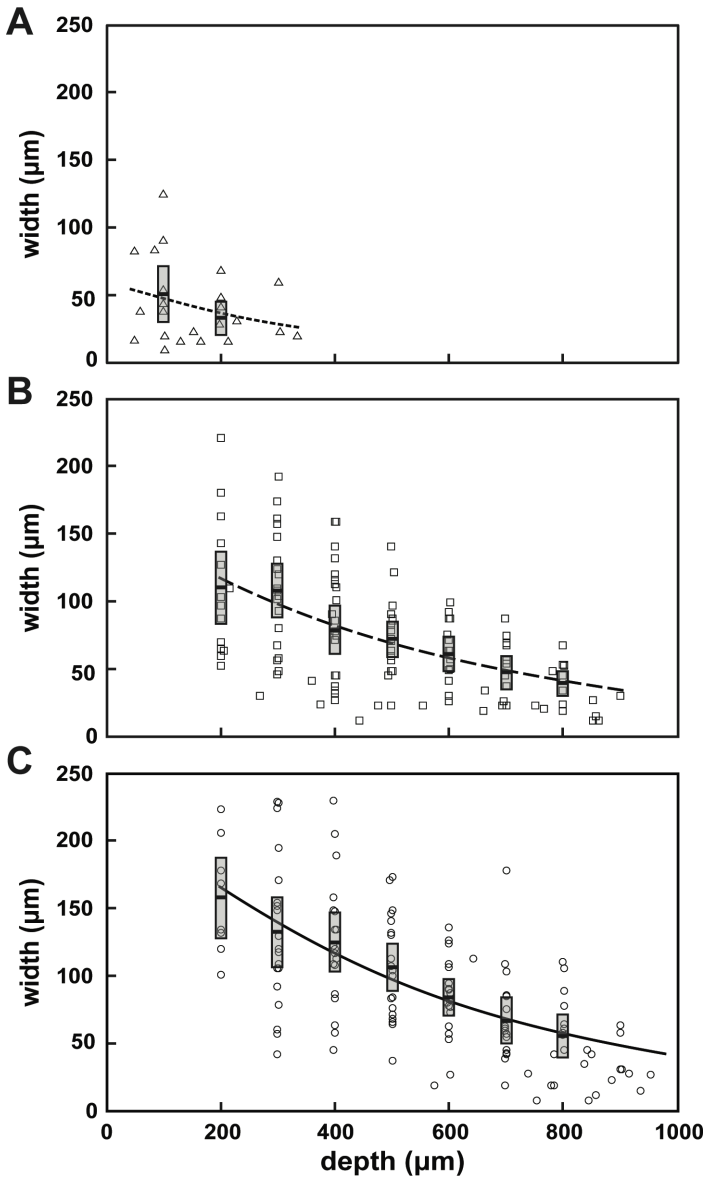

Figure 6.4

Figure 6.4 Cut width dependence on laser energy. Cut width decreases exponentially with depth beneath the cortical surface at laser energies of **A)** 0.3, **B)** 5 and **C)** 13 μJ, with fits to Eq. 6.1 (68 cuts across 5 rats). Each shape represents an individual data point. Within all plots, grey boxes represent 95% confidence intervals about the mean, indicated by the horizontal black line. Black trend lines are respective fits for each data set.

$$w = C\exp\left(\frac{-d}{3l_s}\right) \qquad \text{(Eq. 6.1)}$$

where C is a pre-factor that depends on hydrostatic and vapor pressures and on laser energy, as described by Vogel, *et al.* [22] (Figures 6.4A-6.4C). The scattering length, l_s, in brain for 800-nm light was taken to be 175 μm [23]. These exponential fits generated pre-factor values of approximately 61, 167, and 235 μm for laser energies 0.3, 5.0 and 13.0 μJ, respectively (Figure 6.5). The pre-factors scaled as the cube root of laser energy, consist with the idea that a roughly constant fraction of the laser pulse energy is deposited into the sample by nonlinear absorption over this range of laser energy. We find that

$$C = 99\frac{\mu m}{\mu J^{1/3}}E^{1/3} \qquad \text{(Eq. 6.2)}$$

where E is the incident laser energy (Figure 6.5). Eqs. 6.1 and 6.2 provide a quantitative formula to predict cut width as a function of laser energy and depth within cortex.

The maximum depth where laser damage was observed was characterized for each cut (Figure 6.6). Ablation will occur as long as the laser energy exceeds the threshold energy for optical breakdown in brain, E_{th}, so the maximum achievable ablation depth, d_{max}, increases logarithmically with laser energy as

$$d_{max} = l_s \ln\left(\frac{E}{E_{th}}\right) \qquad \text{(Eq. 6.3)}$$

Fitting to our experimental data gave a threshold energy of approximately 130 nJ, which corresponds to a fluence of 90 J/cm^2, assuming diffraction-limited

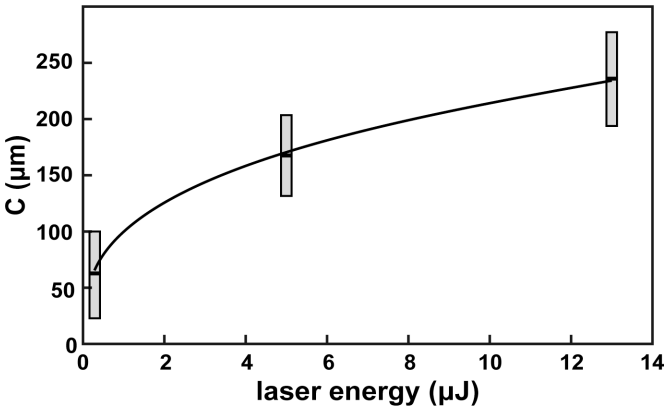

Figure 6.5 The C prefactor. The prefactor in the exponential fits (from Figure 6.4) is proportional to cube root of the laser energy (Eq. 6.2). Grey boxes represent 95% confidence intervals about the mean, indicated by the horizontal black line.

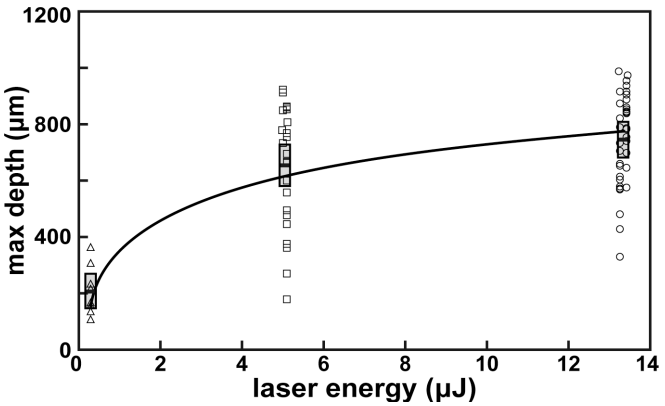

Figure 6.6 Dependence of maximum ablation depth on laser energy. Maximum cut depth increases logarithmically with laser energy (Eq. 6.3). Each shape represents an individual data point. Grey boxes represent 95% confidence intervals about the mean, indicated by the horizontal black line.

focusing (Figure 6.6). This likely significantly overestimates the threshold fluence, as the focusing was unlikely to be diffraction limited deep inside the heterogenous, scattering brain tissue.

6.3.3 Femtosecond laser cutting of neuronal dendrites

We produced sub-surface horizontal cuts in the brain of a live, anesthetized mouse that expressed YFP in a subset of pyramidal neurons and imaged the effect on cortical dendrites using 2PEF microscopy. The cuts were placed approximately 70 μm beneath the brain surface and transected the dendritic projections of the pyramidal cells (Figure 6.7). Dendrites and blood vessels above the targeted depth were unaffected (Figures 6.7A-D), while cut dendrites and bleeding from ruptured capillaries was observed in the plane of the cut (Figure 6.7E-H). Although the dendrites and vessels above the cut are intact, leaked plasma caused by the shallow cut was observed (Figure 6.7D). Dendrites immediately outside the ablated volume did not show signs of degeneration or blebbing characteristic of acute cellular injury (Figure 6.7G).

6.4 Discussion

We demonstrated the ability to produce localized, micrometer-scale, sub-surface cuts in rodent cortex using high-energy, tightly-focused, femtosecond laser pulses. We measured the cut width as a function of depth in the tissue and the incident laser energy as well as the maximum achievable cutting depth as a function of energy. We showed that the cut width decreases exponentially with depth and increases as the cube root of the laser energy, while the maximum achievable cut depth increases logarithmically with laser energy. Overall, our results establish the capability of femtosecond laser

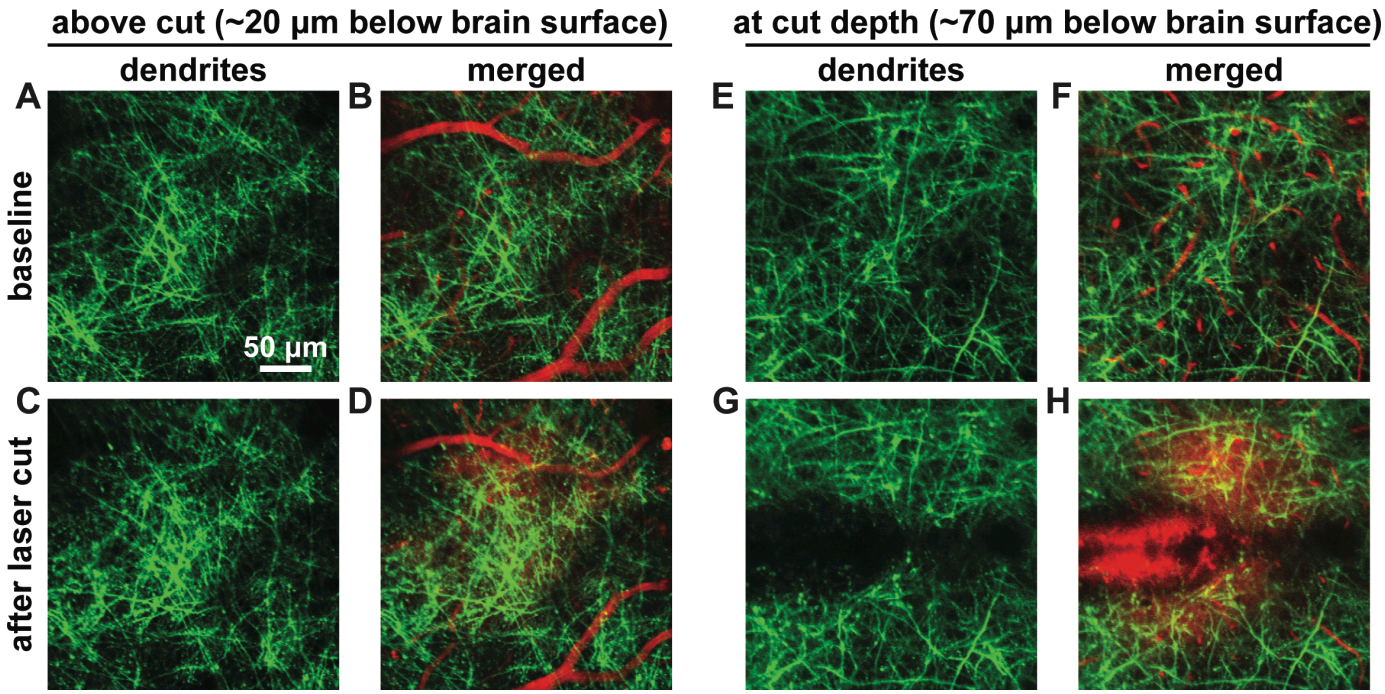
above cut (~20 µm below brain surface)
at cut depth (~70 µm below brain surface)
dendrites
merged
dendrites
merged
A
B
E
F
baseline
50 µm
C
D
G
H
after laser cut

Figure 6.7

Figure 6.7 Femtosecond laser ablation of neural dendrites *in vivo*. Images were obtained from a transgenic mouse that expressed YFP in pyramidal neurons and their dendritic arbors (green). A retro-orbital injection of Texas red-dextran was used to fluorescently label the vasculature (red). Baseline images of dendrites **(A and E)** and merged images of both dendrites and capillaries **(B and F)** located 20 μm below the brain surface **(A and B)** and at the cutting depth of 70 μm **(E and F)**. A cut was produced with incident laser energy of approximately 0.2 μJ that was translated through the cortex at 50 μm/s. Dendrites and blood vessels above the cut **(C and D)** remained unaffected while dendrites were cut and blood vessels were ruptured at the cutting depth **(G and H)**. Post-cut images were acquired approximately five minutes after the cut was produced.

ablation to produce disruption beneath the surface of optically scattering tissue. In addition our work provides a phenomenological guide to what laser energy should be chosen to produce a cut of specified width at a particular cortical depth (Eqs. 6.1 and 6.2), and what ablation depths can be achieved (Eq. 6.3).

The width of the laser cuts varied by about 50% at fixed laser energy and depth. Such variations were likely due to heterogeneity in the vasculature on the surface of the cortex through which the laser beam passed. For example, a large vessel that partially obscures the path of the focused laser beam will attenuate some of the laser energy, due to light absorption and strong scattering by red blood cells [24]. This will reduce the amount of light that reaches the focus, thereby decreasing the size of the cut that is produced.

The maximal achievable ablation depth is ultimately limited by optical scattering. Linear absorption of the laser light could also play a role, but the only significant chromophore in the brain for 800-nm light is the hemoglobin in the red blood cells. The vasculature occupies about 6% of the cortical volume [25], yielding an absorption length of approximately 8 cm, assuming uniformly distributed blood vessels, filled with 2-mM hemoglobin, in tissue with the absorption of water [26,27]. This absorption length is significantly longer than the 175-μm scattering length, so the effects of linear absorption can effectively be ignored, except for the locally strong absorption (and scattering) from large surface blood vessels that was noted above as a potential source of cut heterogenity.

As the focus penetrates deeper into the tissue the laser power must be increased exponentially to compensate for the scattering loss and maintain enough intensity at the focus to cause optical breakdown. On the other hand,

the increase in intensity at depth compared to the surface due to focusing is only a power law with focusing depth. Thus, in order to maintain the same intensity at the laser focus with increasing depth, there is an increase in the intensity at the surface. Eventually, a depth is reached where the intensity at the focus is less than the intensity at the surface of the tissue. At this point, nonlinear absorption will occur at the surface rather than at the focus, prohibiting ablation in the depth. To ensure that ablation is occurring at the focus, the probability of nonlinear absorption at the focus, P_{focus}, must be greater than the probability of absorption at the surface, $P_{surface}$, giving the condition

$$\frac{P_{focus}}{P_{surface}} = \left(\frac{I_{focus}^{N} V_{focus}}{I_{surface}^{N} V_{surface}}\right) \geq 1 \qquad \text{(Eq. 6.4)}$$

where I is the laser intensity, V is the volume, and N is the number of photons which must be simultaneously absorbed to ionize an electron. We approximate the focal volume as a cylinder with diffraction-limited dimensions. Following the analysis of Theer, *et al.*, we take the volume for nonlinear absorption at the surface to be a product of the beam cross section at the surface ($A_{surface} = \pi z^2 (NA)^2 / n^2$) and the scattering length, as the probability of out-of-focus nonlinear absorption will drop dramatically with increasing depth below the surface due to light scattering [28]. This yields

$$\frac{P_{focus}}{P_{surface}} = \left(\frac{2NA^2 z}{n^2 \lambda}\right)^{2N-2} \left(\frac{2\pi n^2 \lambda}{NA^2 l_s}\right) \exp\left(\frac{-Nz}{l_s}\right) \qquad \text{(Eq. 6.5)}$$

where NA is the numerical aperture of the objective lens, z is the depth of the laser focus beneath the cortical surface, and λ is the wavelength of the light.

Breakdown thresholds of biological specimens have been shown to be similar to water [29]. Therefore we assume that for for optical breakdown to occur, the nonlinear absorption of photons must overcome the 6.5-eV bandgap of water. At 800-nm, with a photon energy of 1.56 eV, at least $N = 5$ photons must be simultaneously absorbed in order to overcome the energy bandgap. We assume that these initial seed electrons, generated by multiphoton absorption, can then facilitate avalanche ionization that leads to optical breakdown and damage [4]. In our case, we use an objective lens with an NA of 0.95, an index of refraction of 1.33, an 800-nm wavelength, and a scattering length of 175 μm, which gives a maximum ablation depth of 2.1 mm. In our experimental work, we achieved a maximum ablation depth of about 1 mm beneath the cortical surface using 13-μJ laser pulse energy, and thus did not reach this fundamental limit, but were rather limited by the maximum laser energy we used (and the 2-mm working distance of the objective). We did not observe ablation at the sample surface even with the highest energy, supporting the idea that deeper ablation could be achieved with higher laser energy. Using longer laser wavelengths could likely extend the maximum ablation depth even further. At 1300-nm wavelength, the scattering length is longer by about a factor of two in brain [30], but water absorption has not yet become significant. Using this wavelength would increase the maximum achievable ablation depth predicted by Eqs. 6.4 and 6.5 to 4.8 mm, assuming $N = 7$. This analysis neglects the role of tunneling ionization in producing the initial electrons that seed avalanche ionization and treats the initial electron generation as a pure multiphoton absorption process [3]. For the high-order multiphoton ionization considered here, this assumption likely underestimates the nonlinear ionization rate and therefore somewhat

overestimates the maximal possible ablation depth.

In the sub-surface incisions we produced, capillaries were ruptured, pushing red blood cells and plasma into the brain tissue. This bleeding could trigger inflammatory responses and previous work has suggested that blood products can be epileptogenic [31]. The rupturing of capillaries could be avoided by turning off the cutting laser with a mechanical shutter when the laser focus reaches a vessel. This could be achieved, for example, by detecting 2PEF of intravenously injected fluorescein-dextran generated by a lower intensity femtosecond laser focused just ahead of the cutting laser.

With the ability to produce minimal collateral damage, femtosecond laser ablation is an ideal tool for fine-scale surgery. In addition to sub-surface tissue disruption in non-scattering tissue for ophthalmic surgery [16], femtosecond ablation has also been investigated for surface ablation of tissues, such as teeth and ear [32], showcasing its potential in the clinical setting. We have demonstrated the ability to cut sub-surface, cortical dendrites in optically-scattering brain tissue in live, anesthetized rodents. This capability may open the door for the use of femtosecond laser ablation in the neurosurgical field. One exciting opportunity is in the treatment of focal cortical epilepsy, where this sub-surface laser ablation technique provides a potential path to stop seizures from starting or spreading without damaging the brain's ability to process information. Because seizures spread horizontally through the brain, while much of normal information processing is associated with vertical connections in the brain, making cuts that encircle regions of the brain where seizures start could prevent the seizure from reaching other parts of the brain while minimally affecting the connections more responsible for normal function. Indeed, a mechanically-based implementation of this surgical

therapy, called multiple subpial transections, has been used to treat human epilepsy. In this method, a small hook wire is used to produce full cortical thickness cuts with 5-mm spacing within the epileptic focus [33]. The technique is crude and results have been mixed, in large part due to extensive collateral damage [34,35]. Multiple small optical transactions could be more effective. In addition to blocking propagation of seizures, isolating microcolumns of epileptic cortex could prevent the coalescence of microseizures into a symptomatic seizure, again with minimal damage to vertical cortical connections [36]. Because this optical ablation technique provides extremely high cutting precision, collateral effects on surrounding tissue would be minimal, resulting in a better preservation of normal function and leading to improved patient outcomes as compared to current surgical approaches for epilepsy treatment.

Overall, our work utilizes nonlinear optical techniques to produce micrometer-scale incisions in the cortex of live, anesthetized rodents. While laser-based therapies in the neurosurgical field have been attempted for decades [37], the precision and sub-surface targeting achieved here were not possible with previous approaches. Additionally, our nonlinear techniques produce significantly less collateral damage than previous techniques that relied on linear absorption. We recognize that not all neurosurgical procedures will require such fine-scale tissue disruption, but for surgical procedures that do require such high precision and sub-surface targeting, femtosecond laser ablation provides an attractive approach.

References

1. Anzai Y, Lufkin R, DeSalles A, Hamilton DR, Farahani K, Black KL. Preliminary experience with MR-guided thermal ablation of brain tumors. AJNR Am J Neuroradiol 1995; 16(1):39-48; discussion 49-52.
2. Kennedy JE. High-intensity focused ultrasound in the treatment of solid tumours. Nat Rev Cancer 2005; 5(4):321-327.
3. Schaffer CB, Brodeur A, Mazur E. Laser-induced breakdown and damage in bulk transparent materials induced by tightly focused femtosecond laser pulses. Meas Sci Technol 2001; 12(11):1784-1794.
4. Vogel A, Noack J, Huttman G, Paltauf G. Mechanisms of femtosecond laser nanosurgery of cells and tissues. Appl Phys B-Lasers O 2005; 81(8):1015-1047.
5. Schaffer CB, Brodeur A, Garcia JF, Mazur E. Micromachining bulk glass by use of femtosecond laser pulses with nanojoule energy. Opt Lett 2001; 26(2):93-95.
6. Loesel FH, Fischer JP, Gotz MH, Horvath C, Juhasz T, Noack F, Suhm N, Bille JF. Non-thermal ablation of neural tissue with femtosecond laser pulses. Appl Phys B-Lasers O 1998; 66(1):121-128.
7. Schaffer CB, Nishimura N, Glezer EN, Kim AMT, Mazur E. Dynamics of femtosecond laser-induced breakdown in water from femtoseconds to microseconds. Optics Express 2002; 10(3):196-203.
8. Konig K, Riemann I, Fritzsche W. Nanodissection of human chromosomes with near-infrared femtosecond laser pulses. Opt Lett 2001; 26(11):819-821.
9. Chung SH, Clark DA, Gabel CV, Mazur E, Samuel ADT. The role of the AFD neuron in C-elegans thermotaxis analyzed using femtosecond laser

ablation. Bmc Neurosci 2006; 7:30-41.

10. Yanik MF, Cinar H, Cinar HN, Chisholm AD, Jin YS, Ben-Yakar A. Neurosurgery - Functional regeneration after laser axotomy. Nature 2004; 432(7019):822-822.
11. Supatto W, Debarre D, Moulia B, Brouzes E, Martin JL, Farge E, Beaurepaire E. In vivo modulation of morphogenetic movements in Drosophila embryos with femtosecond laser pulses. Proc Natl Acad Sci U S A 2005; 102(4):1047-1052.
12. Shen N, Datta D, Schaffer CB, LeDuc P, Ingber DE, Mazur E. Ablation of cytoskeletal filaments and mitochondria in live cells using a femtosecond laser nanoscissor. Mech Chem Biosyst 2005; 2(1):17-25.
13. Kumar S, Maxwell IZ, Heisterkamp A, Polte TR, Lele TP, Salanga M, Mazur E, Ingber DE. Viscoelastic retraction of single living stress fibers and its impact on cell shape, cytoskeletal organization, and extracellular matrix mechanics. Biophys J 2006; 90(10):3762-3773.
14. Tirlapur UK, Konig K. Targeted transfection by femtosecond laser. Nature 2002; 418(6895):290-291.
15. Stevenson D, Agate B, Tsampoula X, Fischer P, Brown CTA, Sibbett W, Riches A, Gunn-Moore F, Dholakia K. Femtosecond optical transfection of cells: viability and efficiency. Opt Express 2006; 14(16):7125-7133.
16. Juhasz T, Frieder H, Kurtz RM, Horvath C, Bille JF, Mourou G. Corneal refractive surgery with femtosecond lasers. Ieee J Sel Top Quant 1999; 5(4):902-910.
17. Plamann K, Aptel F, Arnold CL, Courjaud A, Crotti C, Deloison F, Druon F, Georges P, Hanna M, Legeais JM, Morin F, Mottay E, Nuzzo V, Peyrot DA, Savoldelli M. Ultrashort pulse laser surgery of the cornea and the

sclera. J Opt-Uk 2010; 12(8):-.

18. Nishimura N, Schaffer CB, Friedman B, Tsai PS, Lyden PD, Kleinfeld D. Targeted insult to subsurface cortical blood vessels using ultrashort laser pulses: three models of stroke. Nat Methods 2006; 3(2):99-108.
19. Sacconi L, O'Connor RP, Jasaitis A, Masi A, Buffelli M, Pavone FS. In vivo multiphoton nanosurgery on cortical neurons. J Biomed Opt 2007; 12(5):050502.
20. Nishimura N, Schaffer CB, Friedman B, Lyden PD, Kleinfeld D. Penetrating arterioles are a bottleneck in the perfusion of neocortex. Proc Natl Acad Sci U S A 2007; 104(1):365-370.
21. Feng G, Mellor RH, Bernstein M, Keller-Peck C, Nguyen QT, Wallace M, Nerbonne JM, Lichtman JW, Sanes JR. Imaging neuronal subsets in transgenic mice expressing multiple spectral variants of GFP. Neuron 2000; 28(1):41-51.
22. Vogel A, Noack J, Nahen K, Theisen D, Busch S, Parlitz U, Hammer DX, Noojin GD, Rockwell BA, Birngruber R. Energy balance of optical breakdown in water at nanosecond to femtosecond time scales. Appl Phys B-Lasers O 1999; 68(2):271-280.
23. Kleinfeld D, Mitra PP, Helmchen F, Denk W. Fluctuations and stimulus-induced changes in blood flow observed in individual capillaries in layers 2 through 4 of rat neocortex. Proc Natl Acad Sci U S A 1998; 95(26):15741-15746.
24. Horecker BL. The absorption spectra of hemoglobin and its derivatives in the visible and near infra-red regions. J Biol Chem 1943; 148(1):173-183.
25. Tsai PS, Friedman B, Ifarraguerri AI, Thompson BD, Lev-Ram V, Schaffer CB, Xiong Q, Tsien RY, Squier JA, Kleinfeld D. All-optical histology using

ultrashort laser pulses. Neuron 2003; 39(1):27-41.

26. Wray S, Cope M, Delpy DT, Wyatt JS, Reynolds EOR. Characterization of the near-Infrared Absorption-Spectra of Cytochrome-Aa3 and Hemoglobin for the Non-Invasive Monitoring of Cerebral Oxygenation. Biochim Biophys Acta 1988; 933(1):184-192.
27. Smith RC, Baker KS. Optical-Properties of the Clearest Natural-Waters (200-800 Nm). Appl Optics 1981; 20(2):177-184.
28. Theer P, Hasan MT, Denk W. Two-photon imaging to a depth of 1000 mu m in living brains by use of a Ti : Al2O3 regenerative amplifier. Opt Lett 2003; 28(12):1022-1024.
29. Docchio F, Sacchi CA, Marshall J. Experimental investigation of optical breakdown thresholds in ocular media under single pulse irradiation with different pulse durations. Lasers Opthalmology 1986; 1:83-93.
30. Kobat D, Durst ME, Nishimura N, Wong AW, Schaffer CB, Xu C. Deep tissue multiphoton microscopy using longer wavelength excitation. Opt Express 2009; 17(16):13354-13364.
31. Rosen AD, Frumin NV. Focal Epileptogenesis after Intra-Cortical Hemoglobin Injection. Exp Neurol 1979; 66(2):277-284.
32. Lubatschowski H, Heisterkamp A, Will F, Singh AI, Serbin J, Ostendorf A, Kermani O, Heermann R, Welling R, Ertmer W. Medical applications for ultrafast laser pulses. RIKEN Review 2003; 50:113-118.
33. Morrell F, Kanner AM, de Toledo-Morrell L, Hoeppner T, Whisler WW. Multiple subpial transection. Adv Neurol 1999; 81:259-270.
34. Kaufmann WE, Krauss GL, Uematsu S, Lesser RP. Treatment of epilepsy with multiple subpial transections: an acute histologic analysis in human subjects. Epilepsia 1996; 37(4):342-352.

35. Wyler AR, Wilkus RJ, Rostad SW, Vossler DG. Multiple subpial transections for partial seizures in sensorimotor cortex. Neurosurgery 1995; 37(6):1122-1127; discussion 1127-1128.
36. Stead M, Bower M, Brinkmann BH, Lee K, Marsh WR, Meyer FB, Litt B, Van Gompel J, Worrell GA. Microseizures and the spatiotemporal scales of human partial epilepsy. Brain 2010; 133(9):2789-2797.
37. Krishnamurthy S, Powers SK. Lasers in Neurosurgery. Laser Surg Med 1994; 15(2):126-167.

Chapter 7
Halting seizure propagation with a laser scalpel

This chapter discusses ongoing work, as of July 2011, in which we are trying to stop seizure propagation with our femtosecond laser cutting technique. This work is in collaboration with Ted Schwartz, a neurosurgeon at Cornell Weill Medical College. Nozomi Nishimura, Mingrui Zhao, and myself performed our first cutting experiment. The initial box cutting experiments were conducted with Mingrui and more recent data has been compiled with the assistance of an undergraduate, Robert Fetcho.

7.1 Focal seizures and multiple sub-pial transections

Epilepsy is a neurological disorder characterized by the chronic recurrence of seizures. This neurological disorder manifests itself when a population of cortical neurons fire in a rhythmic, hypersynchronous pattern and the generation of this behavior is fundamentally caused by an imbalance between excitatory and inhibitory activity [1]. Epilepsy types can be categorized into two major groups, which depend on the seizure onset location [2]. In generalized epilepsy, the seizure onset involves large areas of the brain, and is mostly associated with biochemical abnormalities [3]. As a result, pharmacological treatments, such as antiepileptic drugs (AED), are usually successful in treating this type of epilepsy. In contrast, partial, or focal, epilepsy is characterized by seizure onsets that initiate in a localized, discrete region of the cortex, and are usually associated with tissue malformations that are often cured with surgical treatment.

For most epileptic patients, AED therapies are often successful in controlling seizure activity. However, approximately 20% of epileptic patients

are medically intractable [4], leaving surgery as a last option, and is most effective in patients who suffer from partial epilepsy. The evolution of a seizure consists of three phases: initiation, propagation, and termination [5], and surgical intervention is aimed at either stopping the initiation altogether or halting propagation. Resective surgery involves the removal of brain tissue, and aims at stopping seizure initiation. However, because the neocortex is responsible for essential human behaviors, resective surgery can lead to the risk functional detriments.

Recent studies have observed that microseizures coalesce into clinically detectable macroseizures, suggesting that microdomains are recruited to initiate seizures [6] that propagate along cortical layers [7]. Additionally, it has been long known that neocortical processing occurs in microcolumns that are vertically organized [8]. The development of a new surgical procedure, multiple subpial transections (MST), aims to take advantage of the cortical arrangement by disrupting horizontal neural connections, while preserving vertical circuitry needed for processing information [9]. In this procedure, 5-mm spaced incisions start at the surface of the brain and span the entire cortical tissue (Figure 7.1). However, this current technique is somewhat crude, as it requires the use of a small, blunt hook to tear the cortical tissue and disrupt the neural connections [9-11]. Histological analyses of human brain tissue after the procedure noted significant pyknosis and edema surrounding the transections [10]. While this procedure has resulted in improved [11,12] and seizure-free [9,13] patients, it has also led to acute [14] and long-term [15] neurological disorders. Much of this variation can be attributed to biological differences, but also can be due to procedural inconsistencies, since the incisions are produced in an unsophisticated

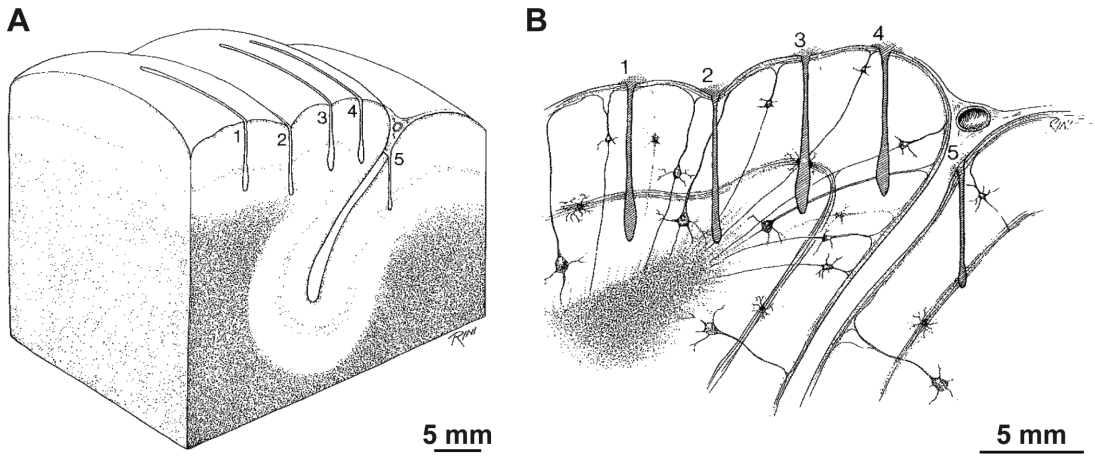

Figure 7.1 Multiple subpial transections. A) Volumetric representation of sub-pial cuts made into the brain tissue using a steel wire. **B)** Cross-sectional view of the cuts. Sup-pial transections are spaced approximately 5 mm apart. Because of the innate architecture of the brain tissue, some cuts span the entire cortex, while others are limited to the superficial layers. Reprinted with permission from [10].

manner.

In this study, we use a laser-based technique to produce sub-surface incisions in cortical tissue, in an attempt to halt seizure propagation. Near-infrared light is weakly absorbed by brain tissue [16]. However, tightly focusing a near infrared, femtosecond laser pulse into the bulk of brain tissue can produce extremely high intensities at the focus and can lead to tissue disruption [17]. Because this process is highly nonlinear, absorption of the laser energy can only occur at the focus where the intensity is the highest, resulting in laser ablation that can be confined to the focal volume [18]. With this technique, it is possible to transect deep layers of the cortex with micrometer precision [19], essentially providing a laser scalpel that can bypass overlying tissue. Here we show that producing sub-surface box incisions deep within the cortex can stop seizure propagation and present a potential new therapy for focally initiated cortical seizures.

7.2 Experimental methods

Refer to Chapter 3.5 for general surgical procedures and optical setup. We initially performed experiments in which we recorded electrophysiology and produced laser cuts under the microscope. In later experiments, multiple fully enclosed box cuts were first produced. After cuts were made, the animal was taken back into the surgery room to record electrophysiology.

Femtosecond laser cuts. For the initial cutting experiments (Figure 7.4), cuts were produced at a depth of 1200 μm and span up to a depth of 200 μm using laser energy of 20 μJ, with a translation speed of 50 μm/sec and a 50 μm cut separation.

In the next set of experiments, we produce multiple 750 μm x 750 μm enclosed boxes at depths of 800 μm up to 150 μm below the brain surface (layers II-IV), with each cut separated by 10 μm (Figure 7.2A). Custom Matlab code was written to interface the translation stages, mechanical shutter (SH-10, Electro-Optical Products Corp.), and waveplate (05RP02-46, Newport Corp.). Box cut patterns were mapped on to two-photon images that were loaded into our custom software, which provided coordinates for cutting patterns. For each segment of the box, the translation stage would move at a speed of 50 μm/s and the shutter would open and close accordingly. At constant incident laser energy, the intensity at the focus increases exponentially with decreasing depth. Therefore, a rotating waveplate was synced with the position of the z-stage, to attenuate and maintain constant laser energy at the focus as the laser focus translated towards the brain surface.

Mapping the surface vasculature. Two-photon images of the cortical vasculature were obtained to locate optimal locations for box cuts. Maps provide locations of large vessels (mainly large viens) that would affect the ability to produce fully enclosed cuts. For example, Figure 7.3 shows a two-photon image of the fluorescently labeled surface vasculature and traversing across the image is a large vein. In this experiment, the box cuts were made just below the vein.

Epileptogenesis. Seizures were induced by injecting a potassium channel blocker, 4-AP (Sigma), through a glass microelectrode. Approximately 0.5 μl of 25 mM concentration was injected using a Nanoject II (3-000-204, Drummond Scientific) at a depth of ~350 μm below the cortical surface.

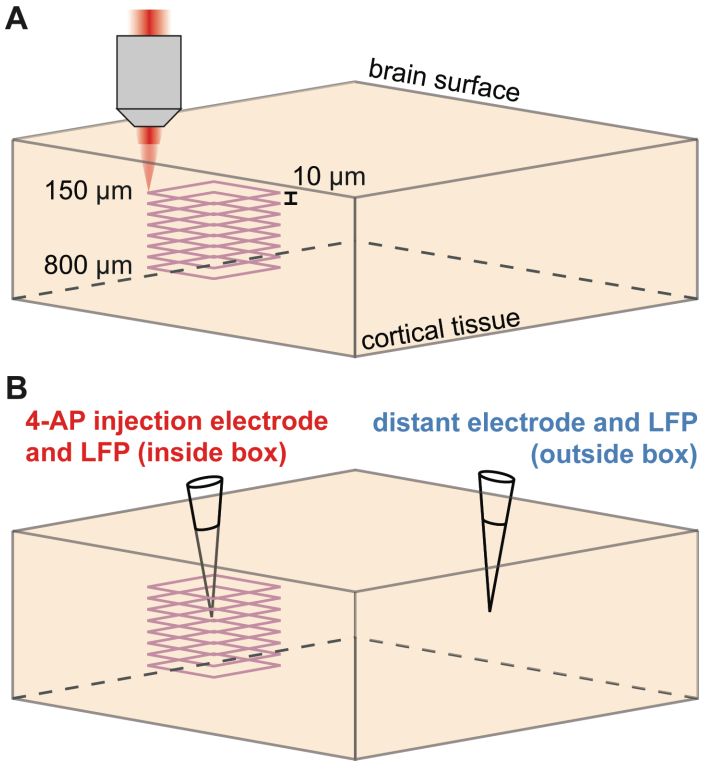

Figure 7.2 Schematic of sub-surface box cuts and electrode placement. A) Multiple box cuts, 750 x 750 μm, are spaced by 10 μm and span the depths of 800 to 150 μm. **B)** After the cuts are made, the animal is removed from the microscope to allow for electrode implantation. The 4-AP electrode in placed inside the box while the distant electrode is implanted outside the box. Both electrodes record electrophyisiology.

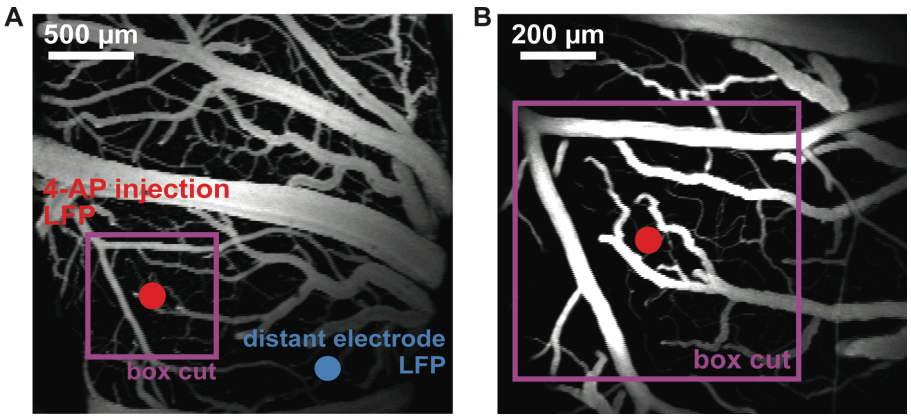

Figure 7.3 ***In vivo*** **mapping of box cuts.** Two photon image projections of the fluorescently vasculature at **A)** high and **B)** low magnification. Purple box represents the location of the box cuts. The red and blue dots represent the 4-AP injection electrode and the distant electrode, respectively.

Seizure activity was easily distinguishable when compared to baseline activity. In most cases, seizure activity was preceded by a distinctive hyperpolarizing spike, followed by prolonged high frequency and high amplitude depolarizations (Figure 7.4B and 7.5) [20].

Electrophysiology and data acquisition. After the cuts were produced, two electrodes were implanted into the cortex to inject 4-AP and record LFP. The electrode placed in the box was back-filled with 4-AP, allowing us to induce focal seizures inside the box and simultaneously record LFP. The second electrode, back-filled with saline, was placed outside the box, generally 1-2 mm away from an edge of the box to record LFP (Figure 6.3B). Both electrodes were implanted using micromanipulators (MLN-33 and MMN-33, Narishige) to a depth of ~350 μm.

Generated local field potentials were amplified by 1000, and filtered with a low and high pass filter of 10 Hz and 1 kHz, respectively (ISO-80, World Precision Instruments). Signals were acquired at a rate of 2 kHz with an A/D DAQ board (DT9834 16-4-16, Data Translation) and written to a text file using custom Matlab (Mathworks) code.

Once both electrodes were implanted, a large custom-built Faraday cage was placed over the experimental setup to block out any potential interference from other RF signals. Baseline data was acquired for 5 minutes prior to injection of 4-AP. For most experiments, reliable seizures were sustained for approximately one hour. A small pool of ACSF was placed on the brain surface to prevent the tissue from drying.

Data analysis and statistics. For propagation analysis, we determined

whether or not a seizure propagated to the distant electrode. In order for the activity to be classified as a seizure, it must possess epileptogenetic properties that were previously described (i.e. initial spike followed by prolonged high frequency, high amplitude spikes). Using the set criteria, we characterized the presence of seizure activity by performing binary analyses (Figure 7.8). For power analysis, time points for each seizure onset and termination were determined. The distinctive hyperpolarizing spike was used as the seizure initiation. Seizure termination was not as clear, and was determined as the point where large LFP spikes disappeared and electrophysiology returned to baseline. Seizure LFP signals, in the time period of interest, were squared and integrated over the time period, giving the total power of the seizure. The same analysis was performed on the LFP signals from the second electrode, with the same time frame. Comparison was conducted using a paired t-test (Figure 7.8). *P*-values less than 0.05 were considered significant.

Post-mortem histology. At the conclusion of each experiment, animals were euthanized and were perfused with 150 ml PBS followed by 150 ml 4% (wt/vol) paraformaldehyde in PBS. Brains were extracted and post-fixed in 4% paraformaldehyde for at least 24 hours. Brains were then cryoprotected using 30% (wt/vol) sucrose in PBS followed by 60% sucrose in PBS with 1% Triton X-100 (vol/vol) (T8787, Sigma), to help prevent shrinkage of the brain tissue [20, [21]]. For cryosectioning, the brain embedded in a cryomold with Optimal Cutting Temperature Compound (O.C.T. Compound, Tissue-Tek) and was allowed to freeze in the cryostat's peltier. Brains were either cut coronally or transversely, into 30-μm thick sections with a cryostat (HM 550 Microm, Thermo Scientific). Slices were then stained with 3,30 -

diaminobenzidine (DAB) (SK-4100, Vector Labs) to detect red blood cells and H&E to view tissue structure. Slides were imaged and examined using an upright microscope (BX41 with DP70 camera, Olympus).

7.3 Results

We used 2PEF to map the surface vasculature to aid in determining the most appropriate location for the box cuts. We then used femtosecond laser ablation to produce sub-surface cuts in the brain to determine if such cuts could stop seizure propagation. Multiple fully enclosed box cuts were produced through layer IV up and to layer II of the cortex. To test the effectiveness of the cuts, two electrodes were implanted into the brain; one was placed in the box and the other outside the box (distant electrode). A seizure-inducing drug, 4-aminopyridine (4-AP), was injected below the brain surface and in the confines of the cuts. We recorded electrophysiology from both electrodes to determine if seizures initiating inside the box propagated to the distant electrode.

7.3.1 Single line cuts alter seizure dynamics

We initially performed experiments in which electrophysiology was recorded and line cuts were produced under the microscope (Figure 7.4). However, space constraints presented challenges in logistics and cut geometry, so in the initial experiments, we were limited to making line cuts. In this experiment we inserted two electrodes into the brain; one electrode injected 4-AP and recorded LFP, and the distant electrode (relative to the seizure focus) recorded LFP (Figure 7.4A). 4-AP was then was injected and we recorded baseline seizure activity. We then produced a wall of cuts that went

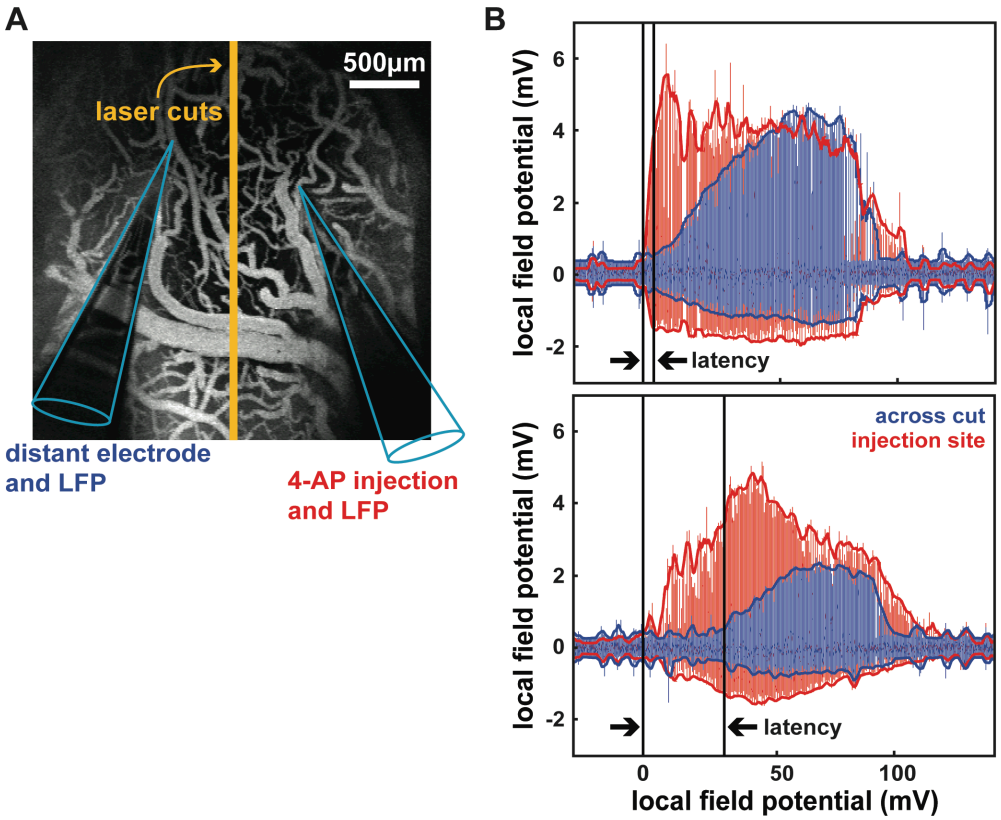

Figure 7.4 Sub-surface cuts alter seizure propagation A) Two-photon image projection of fluorescently labeled vasculature. Dark shadows outlined in blue represent the location of the electrode implantation. The yellow line indicates the locations of the cuts that spanned the depths of 1200 to 200 μm, with 50 μm spacing in between each cut, essentially forming a wall between the two electrodes **B)** LFP recordings at the injection site and across the cut. At baseline, the seizures initiated at the same time. However, after the cuts were made, seizure initiation was delayed at the distant electrode.

from 1200 μm below the brain surface to 200 μm below the brain surface, with each cut separated by 50 μm. Seizures were able to propagate across the cuts, but the onset at the distant electrode was delayed compared to baseline measurements (Figure 7.2B).

7.3.2 Box cuts halt seizure propagation

To determine the effectiveness of the cuts, electrophysiology was recorded from both inside and outside of the cut box. In sham experiments, seizures were detected at the distant electrode almost instantaneously after seizures initiated at the injection site (Figure 7.5A). However in animals with box cuts, seizures did not propagate to the distant electrode (Figure 7.5B). Overall, 100% of seizures in sham experiments propagated to the distant electrode. In contrast, seizures did not propagate when a cut box was present (Figure 7.6). The quantification of LFP power inside and outside the box, for the same time period, was used as a metric to distinguish and verify that seizure activity did not propagate outside the box. The power inside the box (0.41 mV^2-sec ± 0.17; mean ± standard deviation) was significantly greater ($p<0.0001$) than the power recorded at the distant electrode (0.17 mV^2-sec ± 0.05) (Figure 7.7).

7.3.3 Histological verification of box cuts

Brain slices were histologically stained to verify the cuts were being produced below the brain surface. Transverse sections show that box cuts were indeed produced, while coronal sections show the edges of the box cuts (Figure 7.8). In the coronal view, the cell density surrounding cuts is high relative to the tissue far from the cuts, indicating that tissue is being compressed surrounding the laser incisions.

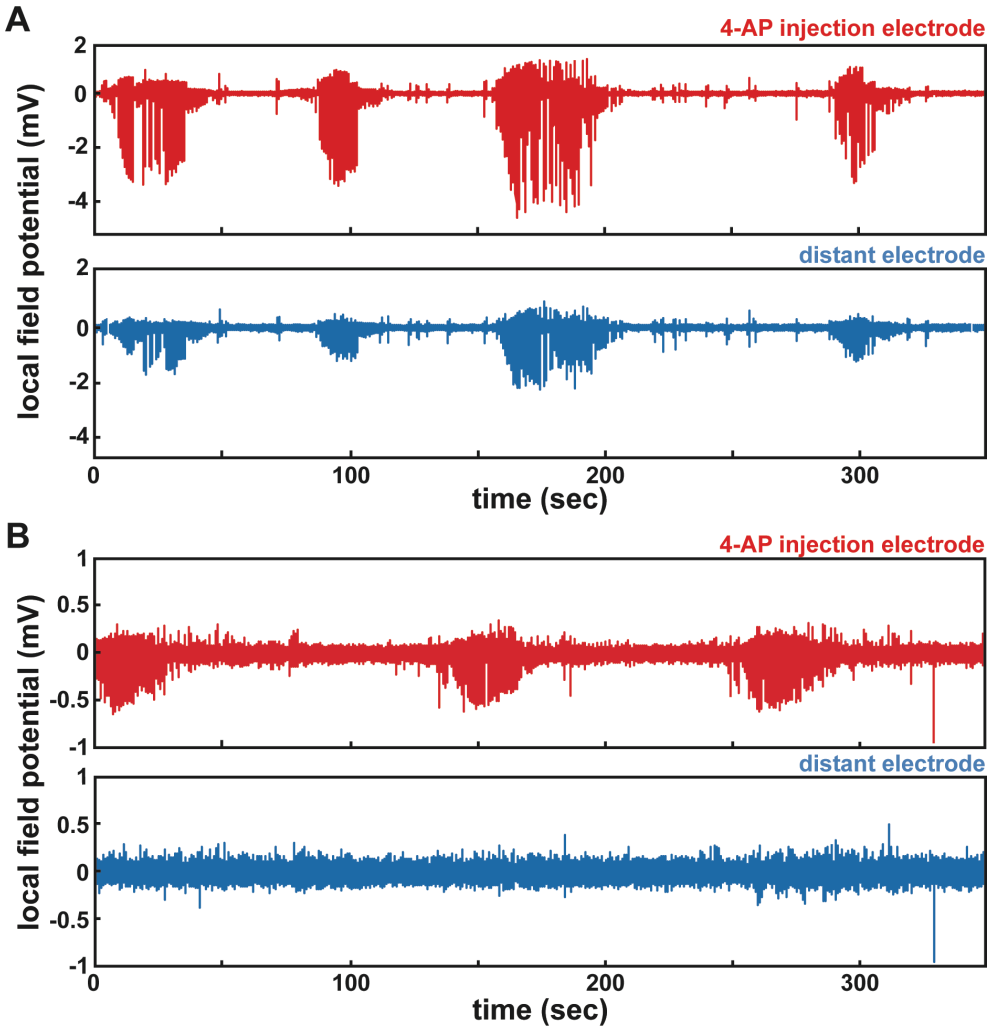

Figure 7.5 Box cuts halt seizure propagation. A) Baseline LFP of seizure propagation. Note that when seizures initiate at the focus they propagate to the distant electrode almost simultaneously. **B)** LFP recordings after producing the box cuts. Seizures that initiate at the focus do not propagate outside the box.

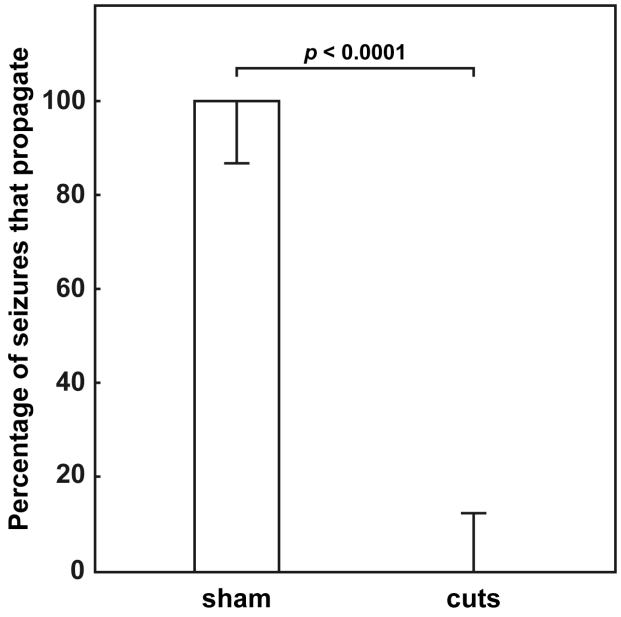

Figure 7.6 Zero percent of seizures propagate after box cuts. Bar plot of the percentage of seizure that propagate for the sham and cut conditions. Error bars were calculated using binomial response statistics and significance was calculated with a binomial comparisons test.

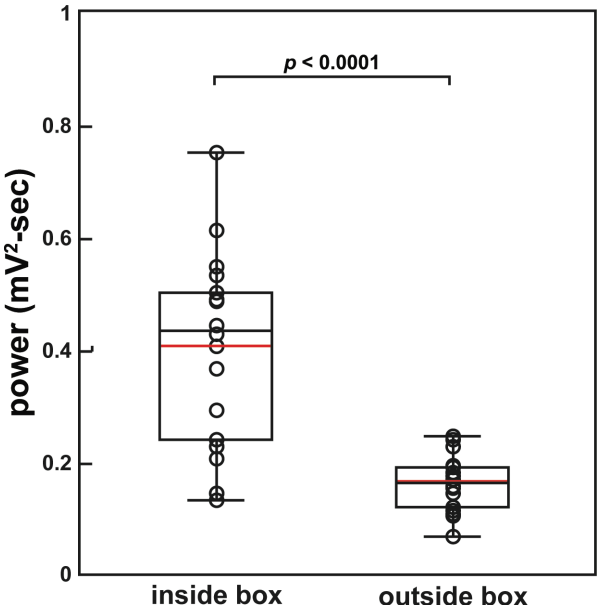

Figure 7.7 Power analysis of LFP. Power boxplot of seizure LFP inside the box and outside the box, for the same time interval. Red and black lines within the boxes represent the mean and median, respectively. Circle represent individual data points. Significance was determined by performing a paired t-test.

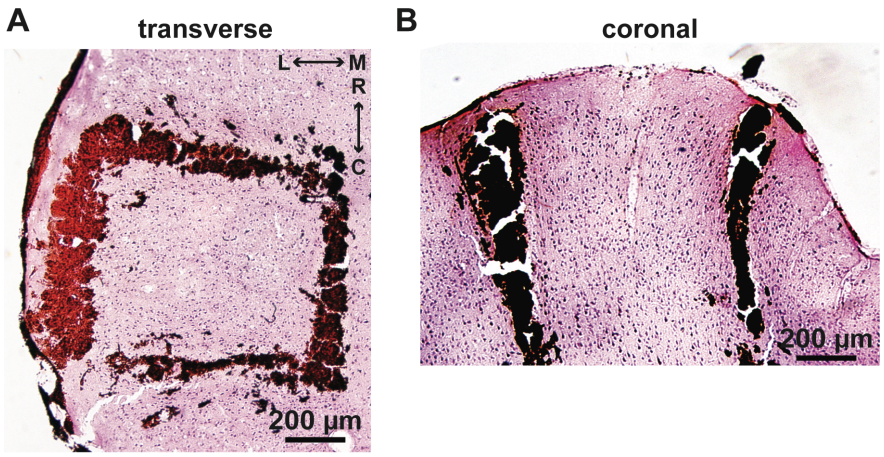

Figure 7.8 Histological verification of box cuts. A) Transverse and **B)** coronal sections of brain slices stained with H&E and DAB.

7.4 Discussion

In this study, laser-based techniques were used to produce sub-surface incisions in cortical tissue, thereby severing neural connections and in effect, disrupting seizure propagation pathways. Initial experiments indicated that sub-surface laser based incisions could alter seizure propagation, but did not completely stop seizures from propagating across the cuts (Figure 7.4). We then produced sub-surface box cuts and implanted electrodes within the box and outside the box to induce seizures and record electrophysiology (Figure 7.2). We found that seizures still initiated inside the box, but did not propagate beyond the cuts to the distant (Figure 7.5). Histological stains verified the presence of the incisions (Figure 7.8). Further quantitative analyses verify that seizure activity did not propagate to the distant electrode (Figure 7.6 and 7.7). These results reveal the potential application of laser-based therapy for treating focally initiated cortical epilepsy.

Femtosecond laser ablation enables precise and controlled sub-surface cutting of cortical tissue. In this study, we use femtosecond laser ablation to produce subsurface cuts that can acutely halt seizure propagation. These incisions are significantly smaller than cuts produced with subpial hooks used during the MST procedure, which led to tissue damage of ~2-3 mm on both sides of the transection [10]. Previous studies have shown that cut widths produced using femtosecond laser ablation can be produced on the order of tens of micrometers, with little collateral damage surrounding the cut [19]. In this study, histological images from these experiments show widening of the cuts as it nears the surface, which is most likely attributed to the calibration between the waveplate and z-stage, and the high laser energies that were

being used. In these experiments we used energies that are approximately four times the energy for optical breakdown of brain tissue. This was done to make certain that cuts overlapped and to compensate for laser attenuation. First, overlapping cuts ensure that there was no intact tissue between cuts, as this may potentially provide a route for seizure propagation. This could have been achieved in two ways: smaller increments between cuts or increasing the laser energy to make bigger cuts. In these experiments cutting a 750 μm x 750 μm box, separated by 10 μm, at a translation speed of 50 μm/s would take approximately 65 min. Stepping in smaller increments increases the time the rodent is under the microscope and potentially affects the animal's physiology. The second reason for using a high energy is to compensate for energy attenuation due to surface vessels. For example, if a large vein were to obscure the path of the focused light, the laser energy will be attenuated due to absorption and light scattering by red blood cells [22]. In order to compensate for this potential loss, cuts are performed with high laser energies. However, the use of such high energies possesses drawbacks. The deposition of high-energy laser pulses not only ionizes the material inside the focal volume, but also leads to the formation of a cavitation bubble that can produce mechanical disruption of tissue the beyond focal region [18]. Long-term studies are needed to investigate the morphological and tissue pathologies that result from these laser-based cuts.

Recording of electrophysiology and producing the laser incisions under the microscope would be ideal. However, with the implantation of the seizure-inducing electrode, it would not have been possible to produce fully enclosed boxes, as the electrode would obstruct the cutting path. Therefore we produced fully enclosed box cuts and performed electrophysiology out from

under the microscope where the logistics of implanting both electrodes were not as difficult.

Potential chronic effects. While we show that femtosecond laser-based cuts can acutely stop seizure propagation, chronic studies of these incisions will ultimately determine the overall efficacy of the sub-surface incisions. These laser-based cuts lead to disruption of the blood brain barrier and parenchymal hemorrhage, which have been associated with the acute development of seizures. [23],[24]. However, the late development of seizures after brain injury has also been observed clinically and is associated with the remodeling of neural connections that make the tissue more susceptible to seizure [23,25]. Inflammatory response due to injury can lead to the formation of glial scar, and in effect, prevent the formation of new networks [26]. In histological analysis of tissue that underwent the MST procedure, patients that formed glial scars were seizure free or had greater than 95% reduction in seizure frequency [10]. Long-term studies of the effects of these laser-based cuts need to be further investigated.

Clinical implementation. This technique provides a much more controlled and precise method for severing neural connections when compared to the mechanical-based method in MST. One of the main advantages of this laser-based method is that tissue below the brain surface can be targeted [19]. For example, if the epileptic focus was located deep within the cortex, our ablation technique can target that specfic location without affecting the overlying tissue. With MST, however, incisions must start at the brain surface to reach targeted tissue below the brain surface, and cause unwanted collateral

damage. The ability to target sub-surface tissues provides a distinct advantage over mechanical techniques, but inherent to most optical techniques is the limit on the penetration depth. Because brain tissue scatters light, the amount of energy deposited at the focus exponentially decreases with increasing depths [27]. At 800 nm, the theoretical cutting limit is approximately 2-mm. Longer wavelength light sources have longer scattering lengths which leads to less scattering. Using a light 1300 nm light source can theoretically allow cuts up to 4.8 mm [19]. Clinical implementation will not only require technical development of stable lasers, but also much more thorough investigations of the long-term effects of laser-based cuts. Nonetheless, these data provide a bright outlook on the potential application of laser-based techniques in the neurosurgical field.

References

1. Treiman DM. GABAergic mechanisms in epilepsy. Epilepsia 2001; 42:8-12.
2. Benbadis SR. Epileptic seizures and syndromes. Neurol Clin 2001; 19(2):251-270.
3. Lowenstein DH. *Seizures and epilspsy* in Fauci AS. Harrison's principles of internal medicine. New York: McGraw-Hill. 2008. pg 2498-2512.
4. National-Institutes-of-Health Consensus Development Conference Statement - Surgery for Epilepsy March 19-21, 1990. Epilepsia 1990; 31(6):806-812.
5. Pinto DJ, Patrick SL, Huang WC, Connors BW. Initiation, propagation, and termination of epileptiform actiity in rodetn neocotex in vitro involve distinct mechanisms. J Neurosci 2005; 25:8131-8140.
6. Schevon CA, Ng SK, Cappell J, Goodman RR, McKhann G, Wazari A, Branner A, Sosunov A, Schroeder CE, Emerson RG. Microphysiology of epileptiform activity in human neocortex. J Clin Neurophsyiol 2008; 25:321-330.
7. Telfian AE, Connors BW. Layer-specific pathways for the horizontal propagation of epileptiorm discharges in neocortex. Epilepsia 1998; 39(7):700-708.
8. Mountcastle VB. The columnar organization of the neocortex. Brain 1997; 120:701–722.
9. Morrell F, Whisler WW, Bleck TP. Multiple subpial transections: a new approach to the surgical treatment of focal epilepsy. J Neurosurg 1989; 70:231-239.
10. Kaufmann WE, Krauss GL, Uematsu S, Lesser RP. Treatment of epilepsy with multiple subpial transections: an acute histologic analysis in human

subjects. Epilepsia 1996; 37(4):342-352.

11. Hufnagel A, Zentner J, Fernandez G, Wolf HK, Schramm J, Elger CE. Multiple subpial transection for control of epileptic seizures: Effectiveness and safety. Epilepsia 1997; 38(6):678-688.
12. Sawhney IMS, Robertson IJA, Polkey CE, Binnie CD, Elwes RDC. Multiple Subpial Transection - a Review of 21 Cases. J Neurol Neurosur Ps 1995; 58(3):344-349.
13. Blount JP, Langburt W, Otsubo H, Chitoku S, Ochi A, Weiss S, Snead OC, Rutka JT. Multiple subpial transections in the treatment of pediatric epilepsy. Journal of Neurosurgery 2004; 100(2):118-124.
14. Devinsky O, Perrine K, Vazquez B, Luciano DJ, Dogali M. Multiple Subpial Transections in the Language Cortex. Brain 1994; 117:255-265.
15. Schramm J, Aliashkevich AF, Grunwald T. Multiple subpial transections: outcome and complications in 20 patients who did not undergo resection. Journal of Neurosurgery 2002; 97(1):39-47.
16. Strangman G, Boas DA, Sutton JP. Non-invasive neuroimaging using near-infrared light. Biol Psychiat 2002; 52(7):679-693.
17. Nishimura N, Schaffer CB, Friedman B, Tsai PS, Lyden PD, Kleinfeld D. Targeted insult to subsurface cortical blood vessels using ultrashort laser pulses: three models of stroke. Nat Methods 2006; 3(2):99-108.
18. Vogel A, Noack J, Huttman G, Paltauf G. Mechanisms of femtosecond laser nanosurgery of cells and tissues. Appl Phys B-Lasers O 2005; 81(8):1015-1047.
19. Nguyen J, Ferdman J, Zhao M, Huland D, Saqqa S, Ma J, Nishimura N, Schwartz TH, Schaffer CB. Sub-surface, micrometer-scale incisions produced in rodent cortex using tightly-focused femtosecond laser pulses.

Lasers Surg Med 2011; 43(5):382-391.

20. Bahar S, Suh M, Zhao MR, Schwartz TH. Intrinsic optical signal imaging of neocortical seizures: the 'epileptic dip'. Neuroreport 2006; 17(5):499-503.
21. Tsai PS, Kaufhold JP, Blinder P, Friedman B, Drew PJ, Karten HJ, Lyden PD, Kleinfeld D. Correlations of neuronal and microvascular densities in murine cortex revealed by direct counting and colocalization of nuclei and vessels. Journal of Neuroscience 2009; 29(46):14553-14570.
22. Horecker BL. The absorption spectra of hemoglobin and its derivatives in the visible and near infra-red regions. J Biol Chem 1943; 148(1):173-183.
23. Herman ST. Epilepsy after brain insult - Targeting epileptogenesis. Neurology 2002; 59(9):S21-S26.
24. Faught E, Peters D, Bartolucci A, Moore L, Miller PC. Seizures after Primary Intracerebral Hemorrhage. Neurology 1989; 39(8):1089-1093.
25. Dichter MA. Basic mechanisms of epilepsy: Targets for therapeutic intervention. Epilepsia 1997; 38:S2-S6.
26. Silver J, Miller JH. Regeneration beyond the glial scar. Nat Rev Neurosci 2004; 5(2):146-156.
27. Helmchen F, Denk W. Deep tissue two-photon microscopy. Nat Methods 2005; 2(12):932-940.

Chapter 8
Glass welding

This chapter diverges from the biological theme of the previous chapters. In this section we use femtosecond laser pulses to fuse two microscope coverslips by forming a weld at the unexposed interface. We noted optical induced by the weld and characterized weld diameters as a function of different laser and experimental parameters. Tensile tests were conducted on the samples to determine its fracture stress and we demonstrated the fabrication and sealing of a microfluidic device with our welding technique. This work was in collaboration with Alan Arai, from IMRA America Inc.

8.1 Femtosecond laser pulses as a point source of heat

Tightly focusing femtosecond laser pulses into the bulk of a transparent material can lead to nonlinear deposition of energy within the focal volume without significant material modification above or below [1-4]. At high repetition rates on the order of MHz, consecutive pulses can be deposited within the focal volume faster than the time for the energy from the preceding pulse to diffuse out of the focal region, leading to the accumulation of thermal energy [5]. Therefore, nonlinear absorption of high-repetition rate femtosecond laser pulses can function as a point source of heat located within the bulk of transparent materials. If a sufficient number of pulses are deposited, the buildup of heat can lead to melted regions much greater than the focal volume. After laser irradiation, the melted glass rapidly cools and resolidifies, leading to changes in its density and refractive index [6]. By translating the focus through the sample, variations in the refractive index have been used as optical waveguides [7]. However, in this study, we utilize

the point source of heat to produce welds at the unexposed interface between two pieces of glass [8].

Laser-based techniques to weld glass have been widely used, but are often limited to areas with exposed edges or interfaces. Some welds can be formed internally, but this requires the use of another material, such as a light-absorbing thermoplastic. However, in some applications, such as microfluidics, it would be advantageous to internally fuse together two pieces of glass. Pulse durations on the order of picoseconds have been used for glass micromachining, but it has been shown that femtosecond laser pulses lead to better confinement of the energy deposition, and therefore more precise micromachining [9,10]. In one of the first femtosecond laser-based welding studies, Tamaki *et al*. used a 1-kHz pulse train to fuse two pieces of silica at the unexposed interface [11]. However, at this repetition rate, heat is not able to accumulate within the focal volume and therefore not able to melt glass beyond the focal region. Additionally, because of the low repetition rate, these experiments were limited to translation speeds of 5 μm/s. In subsequent work, high repetition rates of laser pulse trains have been used to produce welds between two pieces of glass. One of the key questions that ultimately arise from these studies is how well these welds are able to withstand loads. Previous studies have subjected welds to a number of tests [12-14] and find that the functional strength of the weld largely depends on the type of fracture test.

In this current study, we investigate welds generated at the unexposed interface between two pieces of borosilicate glass using a high repetition, femtosecond laser pulse train. Optical images confirm that we were able to produce welds internally located between the glass samples. For a wide

variety of laser parameters, we find that the weld is significantly larger than the focal volume. As expected, weld diameters increased with increasing laser energies and decreasing translation speeds, which is in agreement with a thermal accumulation mechanism. Lastly, we conducted tensile tests to determine the fracture strength of the welds and interestingly observe that samples produced using smaller energies were stronger than those generated with larger energies.

8.2 Experimental methods

Producing femtosecond laser-based welds. We use 170-μm thick coverslips approximately 24 by 50 mm in size made from Corning 0211, a zinc-doped borosilicate glass. The glass samples are cleaned with methanol and lens paper. Two pieces are then placed on top of each other and pressed togehter until Newton rings disappear, indicating a minimal gap between the two pieces of glass. The adhered glass samples are then placed on a three-axis translation stage and a train of 350-fs duration, 1045-nm wavelength laser pulses (FCPA μJewel D-400, IMRA America, Inc.) was focused at the interface between the two pieces of glass using a 0.55 NA aspheric microscope objective (5722BH, New Focus, Inc.) (Figure 8.1A). The sample was leveled on the translation stage so the laser focus remained at the glass interface when the sample was translated. The samples were then translated across the focus, forming a weld at the glass interface (Figure 8.2B). The repetition rate of the laser was varied from 0.1 to 5 MHz, the energy was varied from 60 nJ to 2 μJ, and the translation speed varied from 100 μm/s to 100 mm/s. Samples used for imaging had multiple welds, while samples used for fracture testing had individual welds with lengths that were either 5, 10, or 15 mm.

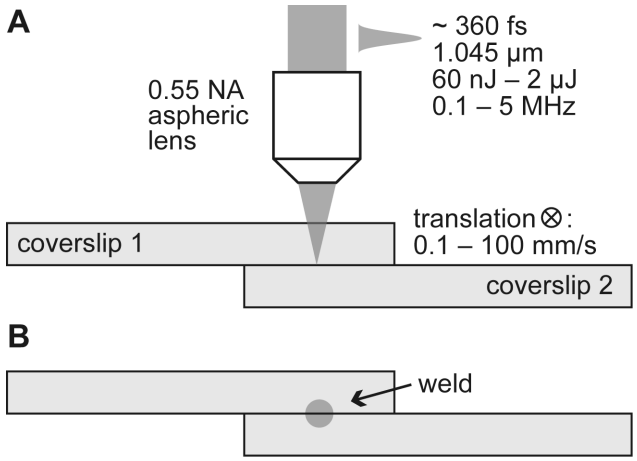

Figure 8.1 Schematic of femtosecond laser welding of glass. A) Nonlinear absorption of tightly-focused femtosecond laser pulses deposits energy in the focal volume, located at the interface between two pieces of glass. Because of the high repetition rate, energy is deposited at a rated faster that it can diffuse out of the focal volume. To form a cylindrical weld, the sample is translated perpendicular to the propagation direction of the laser beam so that the laser focus stays at the interface between the two materials. **B)** Glass on either side of the interface melts, leading to fusion of the two materials when they cool.

Weld strength. Tensile tests were conducted on each sample to determine its failure stress. Custom aluminum adapters were designed to mount the sample to an existing tensile apparatus (EnduraTEC ELectroForce 3200, BOSE Corp.). The top and bottom exterior faces of the sample were glued to the adapters and allowed to set. The setup was then submerged under water to mitigate the effects of stiction between the two coverslips to test only the weld. The mounted sample was then placed in the tensile machine, ensuring the applied tension lined up axially with the weld. Tensile tests were displacement controlled, straining at a rate of 1 μm/s. A fixed force transducer detected the load applied on the sample (Figure. 8.6).

8.3 Results

In this investigation, we used high-repetition rate, femtosecond laser pulses to form welds at the unexposed interface between two coverslips. Optical images showed changes in the index of refraction at the weld and the regions surrounding it. We then characterized the weld diameter as a function of laser energy, translation speed, and repetition rate of the femtosecond laser pulse train. Tensile tests were conducted to determine the fracture stress of the welds. We then discuss the utility of femtosecond laser welding by showcasing a microfluidic device constructed using femtosecond laser ablation and welding.

8.3.1 Induced optical changes in glass

Optical imaging reveals small refractive index changes in the weld regions (Figure 8.2A), resembling the appearance of optical waveguides written into this glass with high repetition rate trains of femtosecond laser pulses [3].

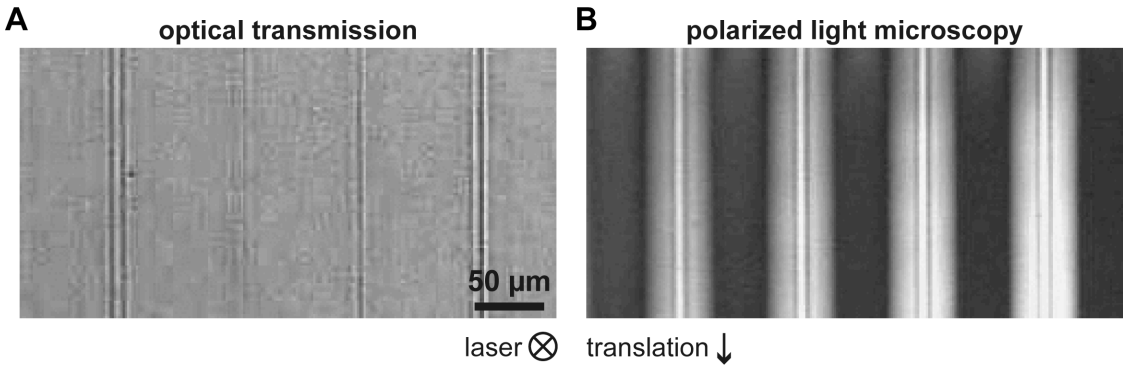

Figure 8.2 Top-view images of femtosecond laser welds. A) White-light transmission and **B)** polarization microscope images of a series of welds formed between two 170-µm thick pieces of Corning 0211 glass using a 1-MHz train of 550-nJ, 350-fs, 1045-nm laser pulses focused with a 0.55 NA lens while the sample was translated at 10 mm/s perpendicular to the incident direction of the laser beam. The direction of propagation of the laser pulse train and the translation direction are indicated. Note the high contrast in polarization image, likely due to strong birefringence in the weld.

Polarization microscopy shows that the welds are highly birefringent (Figure 8.2B) perhaps indicating trapped stresses.

Samples with a series of welds were scribed with a diamond scribe and fractured. In regions near where the welds were present, the fracture plane tended to go through both pieces of glass at the same location, while there is likely to be a "ledge" in regions far from the welds. It is likely that the welds tended to provide a path for the fracture to propagate from one piece of glass to the other, leading to fracture in the same plane. The fractured glass samples were imaged with optical transmission, optical reflection, and scanning electron microscopy (SEM) (Figure 8.3). Transmission images revealed refractive index changes in the weld region that resemble those associated with the formation of optical waveguides (Figs. 8.3A and 8.3B). Under optical reflection (Figure 8.3C) and SEM (Figure 8.3D) imaging, the interface between the two pieces of glass is gone in the weld region, but clearly visible outside the weld region, indicating fusion of the two pieces of glass in the weld region. We measured the transmission of 350 fs, 1045 nm wavelength laser pulses focused into Corning 0211 glass with a 0.49 NA aspheric objective at 100 kHz and 1 MHz, as a function of laser energy. The damage threshold for both repetition rates was seen to occur between energies of 50 to 90 nJ (Figure 8.4).

8.3.2 Parameters influencing weld diameter

Welds were produced using 350 fs, 1045 nm wavelength laser pulses focused with a 0.55 NA aspheric objective with repetition rates ranging from 0.1 to 5 MHz. Samples were translated at speeds of 0.2, 1, 5, 25, and 125 mm/s with energies varying between 64 nJ to 2.1 μJ. There was an overall trend showing increased weld diameter with increasing repetition rates. Expectedly,

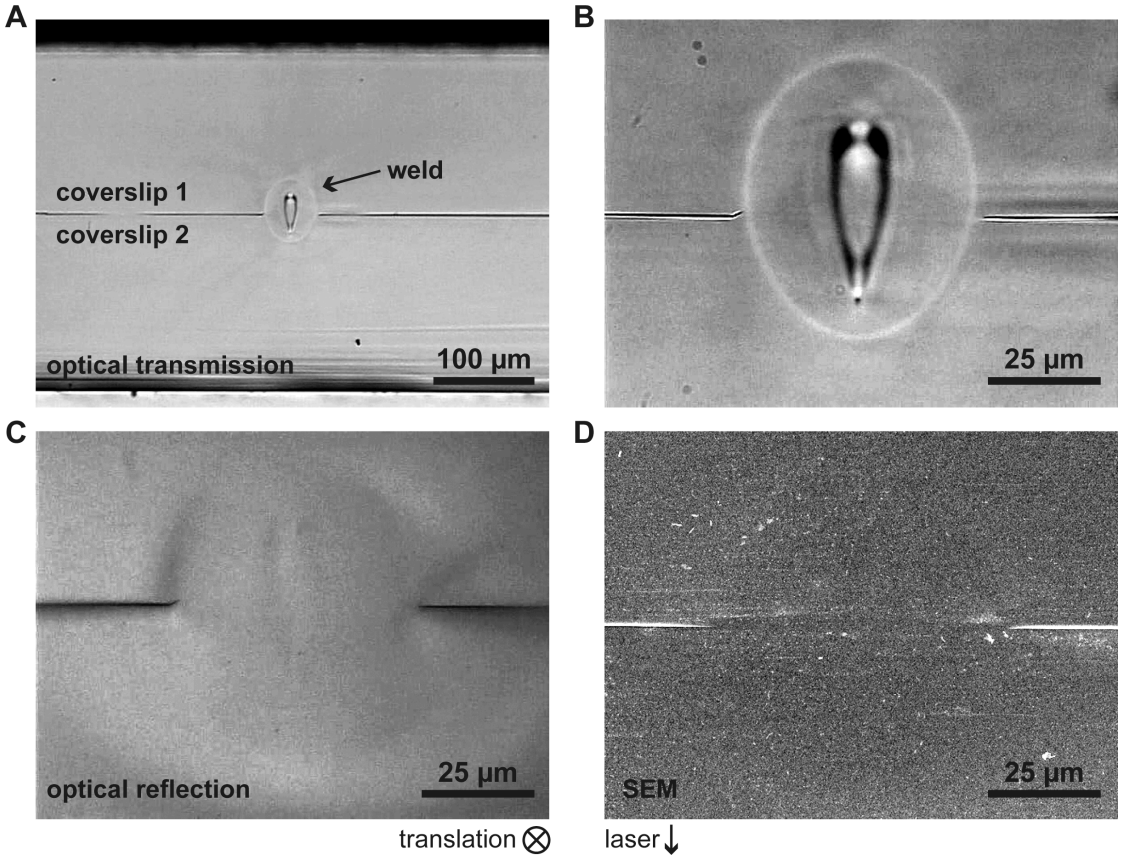
A
coverslip 1
coverslip 2
weld
optical transmission
100 µm
B
25 µm
C
optical reflection
25 µm
translation ⊗
D
SEM
25 µm
laser ↓

Figure 8.3

Figure 8.3 Side-view images of a femtosecond laser weld. A) and **B)** White light transmission images of a weld formed between two 170-μm thick pieces of Corning 0211 glass using a 1-MHz train of 550-nJ, 350-fs, 1045-nm laser pulses focused with a 0.55 NA lens while the sample was translated at 10 mm/s perpendicular to the incident direction of the laser beam. After forming several welds, the sample was scribed with a diamond and fractured perpendicular to the weld lines enabling edge-on imaging of the weld. Refractive index differences in the weld region are evident from the transmission images. **C)** Optical reflection image of the same weld in *A* and *B*. **D)** SEM imaging of the same weld in *A*–*C*. The sample was coated with 80 nm of gold before being placed in the SEM. The images in *C* and *D* show the interface between the pieces of glass is eliminated in the weld region. The direction and propagation of the laser pulse train and translation direction are indicated.

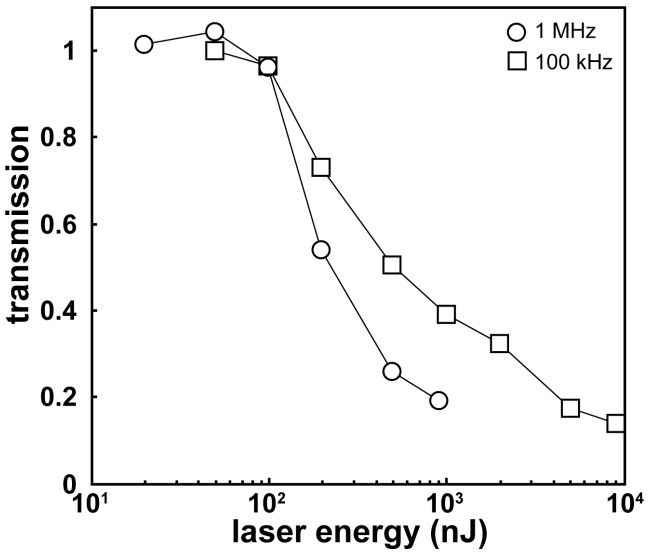

Figure 8.4 Transmission of laser energy. Transmission of 350 fs, 1045 nm wavelength laser pulses focused with a 0.49 NA aspheric objective into Corning 0211 glass as a function of laser energy, for two different repetition

weld diameter also grew with increasing laser energy, within each repetition rate. The largest welds were produced with a pulse energy of ~250 nJ, at a repetition rate of 2.5 MHz, and translated at the slowest speed (Figure 8.5).

8.3.3 Fracture strength of welds

Fracture strengths of the welds were determined by conducting tensile tests on the welded sample (Figure 8.6). A typical load profile as a function of time is shown in Figure 8.7A. Note that the peak of the profile is the point of failure. The failure stress of each sample was calculated by dividing the peak force, calculated from the load, by the cross-sectional area of the weld that was perpendicular to the load direction. Samples generated with the largest energies were observed to be the weakest, with an average failure stress of 2.5 MPa ± 1.6 MPa (mean ± standard deviation), whereas samples with the smallest welds were seen to be the strongest, with an average failure stress of 7.2 MPa ± 5.9 MPa. Welds produced with an energy of 550 nJ had an average failure stress of 3.6 MPa ± 2.4 MPa. While there is not a significant difference between the samples, there is a weak trend indicating that higher energies produce weaker welds ($p < 0.11$, Cuzick's trend test).

8.3.4 SEM images of fractured welds

SEM images revealed varying fracture behavior for welds produced at different energies. Welds produced at lower laser energies (280 and 550 nJ) tended to fractured within the welds, whereas welds produced higher laser energies (853 nJ) appeared to fracture at the interface between the weld and native glass (Figure 8.8).

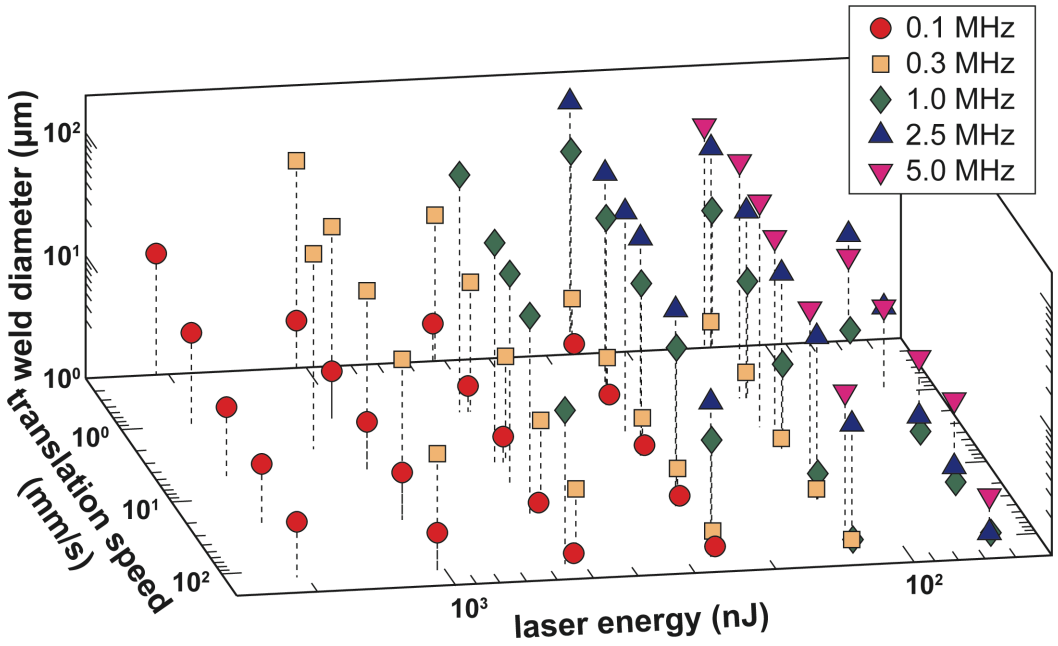

Figure 8.5 Weld diameter dependence on machining parameters. Plot of weld diameter as a function of laser energy and translation speed, for various repetition rates. In all cases, 350 fs, 1045 nm, wavelength laser pulse train was focused with a 0.55 NA lens.

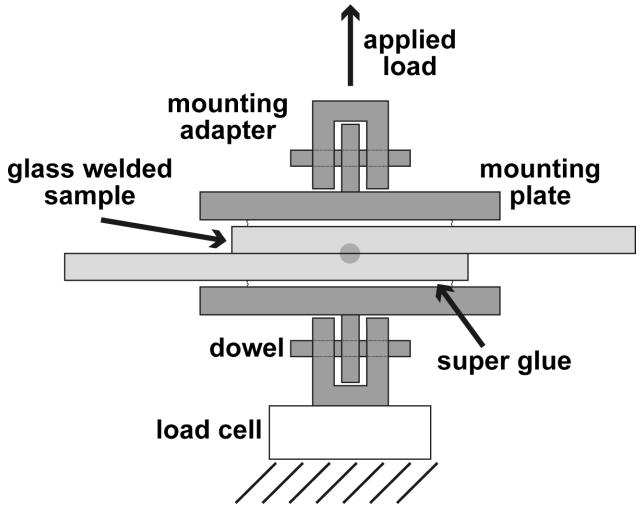

Figure 8.6 Experimental setup for tensile tests. Samples are glued in between a custom designed mounting plates that allow for tensile testing. The apparatus is then fixed to mounting adapters using dowels, with one end attached to a load cell while the other end applies the load. All mounting apparatuses and dowels are made from aluminum.

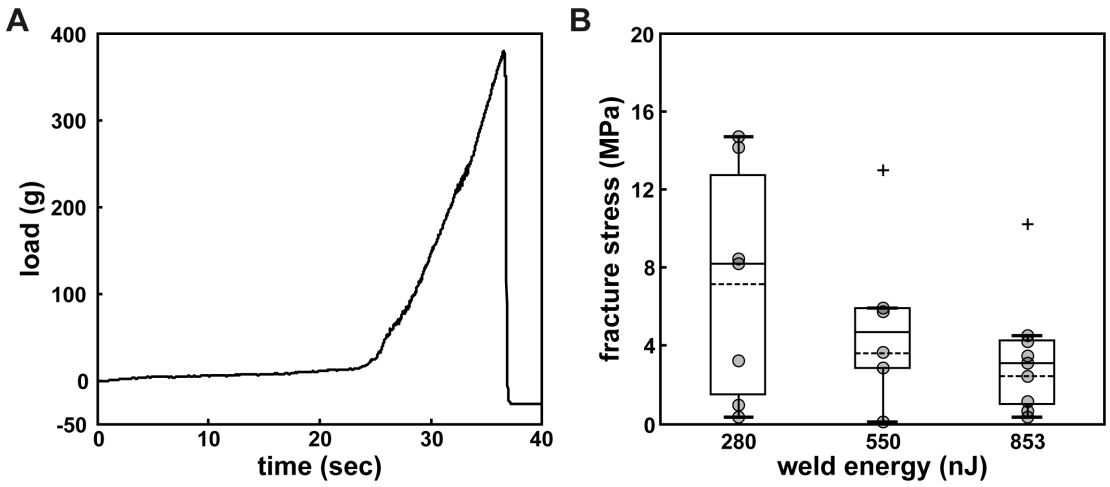

Figure 8.7 Loading profile and weld failure stress. A) Plot of applied load versus time for a weld formed at energy 550 nJ in Corning 0211 glass. Peak values of the load profile were taken as the fracture load. **B**) Boxplot of fracture stress as a function of weld energy. Stress values were calculated by taking the peak fracture load divided by the top-view cross-sectional area. We note a trend that shows welds produced at higher energies fracture at lower stress ($p < 0.07$). Circles represent individual data points and crosshairs indicate statistical outliers. Solid and dashed lines represent the median and mean, respectively.

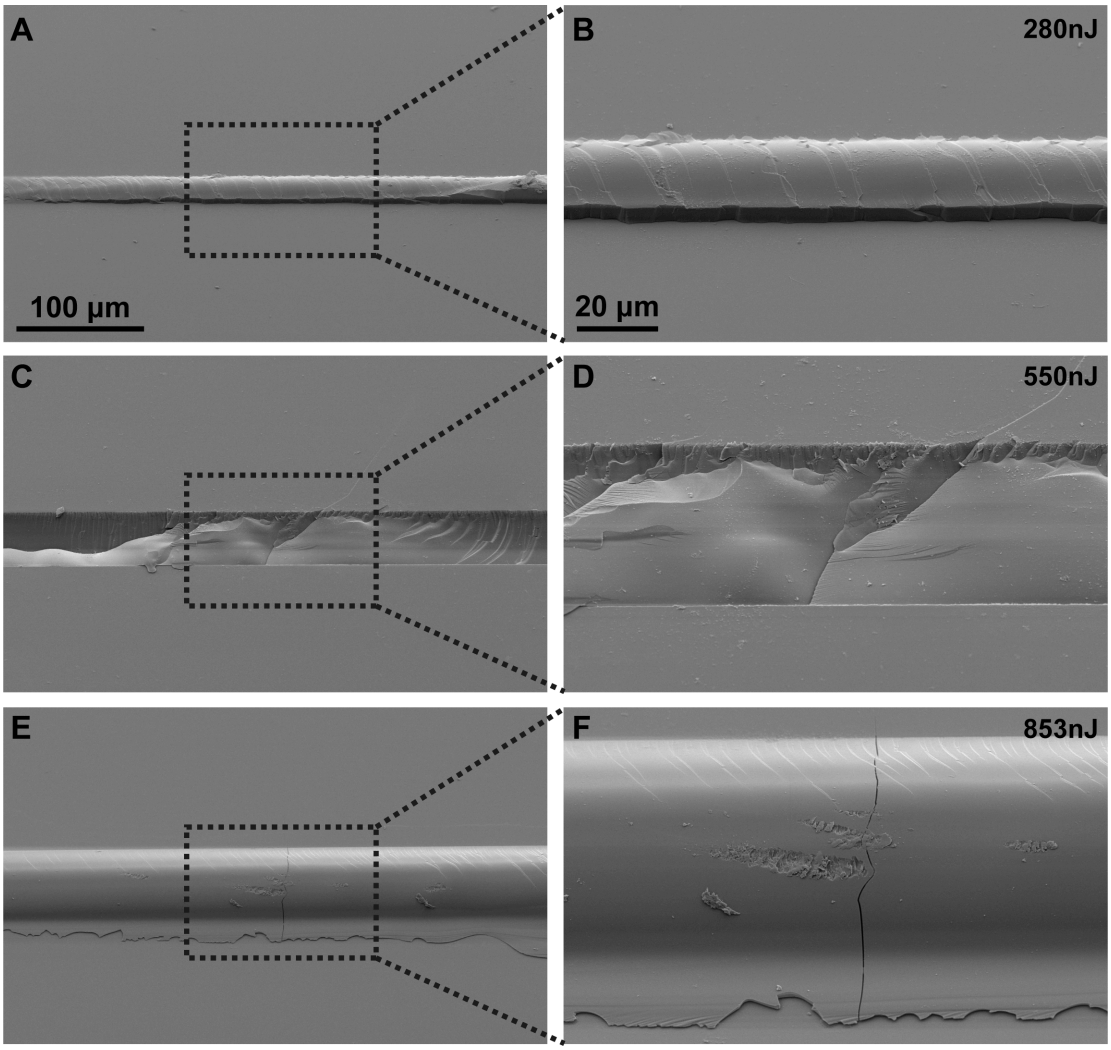

Figure 8.8 SEM images of fractured welds. generated using a 1-MHz train of 1045 nm, 350 fs laser pulse with energies of **(A** and **B)** 280 nJ, **(C** and **D)** 550 nJ, and **(E** and **F)** 853 nJ. In all cases, the laser was focused using a 0.55 NA lens and samples were translated at 10 mm/s.

8.4 Discussion

We examined optical and mechanical properties of welds produced at the unexposed interface between two coverslips, using a high-repetition, femtosecond laser pulse train. Optical microscopy of the samples shows the welds induced refractive index changes in the glass and SEM images reveals a fused region in between the two pieces of glass (Figure 8.2 and 8.3). We characterized weld diameter as a function of translation speed, laser energy and repetition rates (Figure 8.5). Furthermore, we conducted tensile tests to determine its fracture strength (Figure 8.7), with SEM images indicating different failure modes (Figure 8.8).

Microfluidic devices have emerged as a powerful tool in fields that spans an incredibly wide spectrum of fields [15]. Much of this can be attributed to the development of fabrication techniques, such as soft lithography [16]. In this technique, relief patterns are produced on the surface of elastomers, such as poly(dimethyl) siloxane (PDMS), using a master mold. While this technique is efficient and relatively low-cost, there are some inherent limitations. For instance, if the aspect ratio, the ratio between the height and the width, of the feature is too high or too low, it can cause the PDMS to deform and lead to defects in the microstructures. PDMS relief features are limited to aspect ratios between 0.2 and 2. Femtosecond laser ablation provides a unique, high-precision micromachining tool that allows for the removal of material on the surface or in bulk, enabling extremely high aspect ratios in PDMS as high as 800:1 [17]. Tightly focusing high-energy femtosecond laser pulses into transparent materials, such as glass, can drive nonlinear absorption of the laser energy at the focus, leading to ablation that is three-dimensionally confined to the focal volume and thus allowing for micromachining of

microfluidic channels [18,19]. One concern with this method is the removal of debris during the micromachining process. To mitigate this issue, liquid and ultrasound agitation has helped facilitate the sufficient removal of debris [20]. It is worth noting that this technique is inherently low throughput, and is impractical for producing large-scale microfluidic systems.

Here, we produce an all-glass microfluidic device, where channels were produced using femtosecond laser ablation, and sealed with a welded coverslip (Figure 8.9). Channels were formed into a glass microscope slide (Corning 2947) with a 50-kHz train of 10-μJ, 450-fs, 1045-nm laser pulses, focused with a 25-mm singlet lens. The translation speed of the sample through the focus was 80 mm/s, with 5-um raster overlap. After the channels were formed, the slide was placed in an ultrasonic bath and cleaned with acetone. Previous groups have used a glass coverslip to seal PDMS devices [17], or vice versa [21]. To seal our device we welded a coverslip (Corning 0211) to the top of the microscope slide, using the same laser parameters cited earlier in this study. Two source basins were also formed into the glass slide (not shown), but were not covered. Two drops of food coloring, blue and yellow, were simultaneously dropped into the basins, where capillary action pulled the liquids through the channel, where they subsequently mixed downstream of the T-junction (Figure 8.9). This microfluidic example showcases the utility of femtosecond lasers in not only micromachining channels, but also sealing devices with glass welds.

We characterize the strength of our welds by performing tensile tests on the fused samples. We interestingly observe that welds produced with higher energies, fracture at lower stresses. To possibly explain this, a recent study investigated the strain distribution in regions surrounding the molten volume.

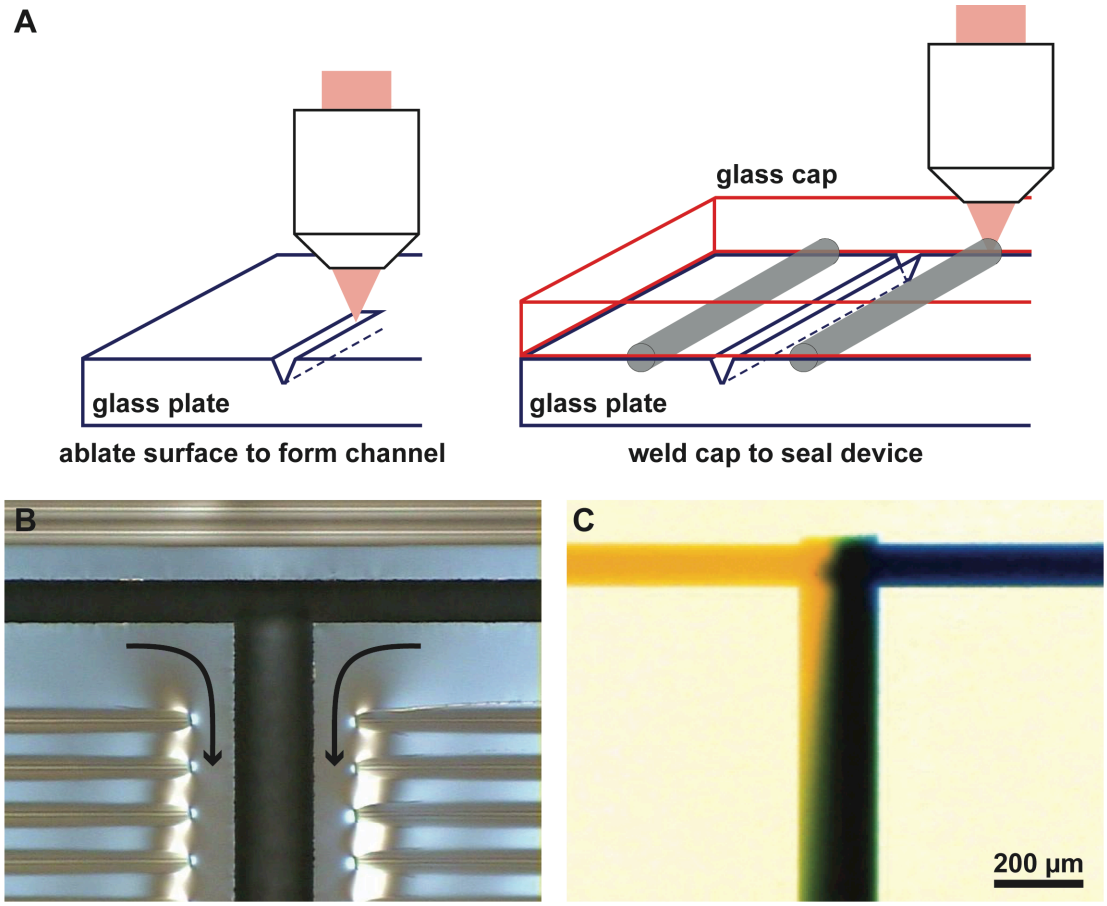
A
glass plate
ablate surface to form channel
glass cap
glass plate
weld cap to seal device
B
C
200 µm

Figure 8.9

Figure 8.9 Fabrication of microfluidic femtosecond laser pulses. A) Schematic of femtosecond laser ablation and welding procedure to produce a microfluidic device. A femtosecond laser is tightly focused on the surface of the glass to ablate a channel using a 10-μJ, 450 fs, pulse train at 50 kHz, focused using a 25 mm singlet lens, with the sample translated at 80 mm/s. A glass cap is then welded on top of the channel to seal the device using a 550-nJ, 360 fs pulse train at 1 MHz, focused using a 0.55 NA aspheric lens, with the sample translated at 10 mm/s. **B)** Polarize light microscopy of the microfluidic device. Note the T-shaped channel and the welds on the side of the channel used to seal the device. (c) While-light transmission image of mixing between yellow and blue dye. Arrows indicate direction of flow in the channel.

The authors noted that as energy is being deposited, the pressure wave emanating from the focus [22], compresses the molten glass, causing the viscosity of the outer regions to decrease. This decrease in viscosity leads to viscoelastic deformation of the glass, which is strongly dependent on the relative viscosities due to the temperature distribution from the photoexcited region, and claim that the heat-induced modification should be produced at the outermost boundary. After irradiation ceases, the molten glass rapidly cools and therefore, traps strain in these deformed regions [23]. This would imply that welds produced with higher laser energies would have higher trapped strain in the outermost regions, and therefore more susceptible to failure, which we observed in our study. Richter *et al.* performed failures tests on fused samples that contained continuous or spot-welds. Samples with continuous lines failed at lower stresses when compared to samples with spot-welds when molten areas were equal [13]. This is most likely attributed to larger amounts of trapped stress along the length of the continuous welds. To mitigate the effects of trapped stress, the samples can undergo stress and volume relaxation through the annealing process [24]. Watanabe *et al.*, observed over a factor of two increase in weld strength, as well as increased light transmittance through the weld, after annealing welded samples [25].

There have been several studies that have characterized the strength of glass welds. In our study, our samples undergo tensile test, which is a good measure of how well the fused coverslips are joined together. Tamaki *et al.* performed similar tests and found similar stress fracture values [12]. Shear testing of welded samples is more likely to characterize mechanical properties of the actual weld, as the native glass is pushing against weld [14], as opposed to pulling away in a tensile test [12]. Table 8.1 summarizes studies that have

investigated weld strength using different fracture tests and highlights the idea that characterization of weld strength should be conducted depending on the application. For instance, if a welded sample was to be exposed to flexural strain, a 3-pt bending test is most appropriate for characterizing its failure stress [13]. Or if a microfluidic device were to be sealed with a welded coverslip, a tensile test on the sample would be most appropriate to determine how much internal pressure the device can withstand. Together, these studies showcase the versatility of the femtosecond welding. If the ultimate goal is to produce the strongest weld, further fracture tests that anneal the welded samples should produce more positive results.

Table 8.1 Weld failure stresses for different glasses and fracture tests

Reference	Experiment parameters	Glass type	Fracture test	Failure stress (MPa)
current study	1 MHz 1045 nm 350 fs 280, 550, 853nJ NA: 0.55 10 mm/s	Corning 0211 borosilicate	tensile	7.2 ± 5.9 (280 nJ) 3.6 ± 2.4 (550 nJ) 2.5 ±1.6 (853 nJ)
Tamaki [12]	500 kHz 1558 nm 947 fs 800 nJ NA: 0.4 0.01, 0.02 mm/s	non-alkali alumino silicate	tensile	9.87 (0.01 mm/s) 6.81 (0.02 mm/s)
Richter [13]	2.3-9.4 MHz 515 nm 550 fs 100-160nJ NA: 0.1-0.4 0.02-3.33 mm/s	fused silica	3-pt bending	25 (lines of welds) 54 (spot welds)
Cvecek [14]	1 MHz 1064 nm 10 ps 2, 3 µJ NA: 0.55 20 mm/s	D263T borosilicate (3 µJ) BF33 borosilicate (2 µJ)	shear	55 ± 33 (D263T) 92 ± 72 (BF33)

Values in *Experiment parameters* represent (from top down): laser repetition rate, laser wavelength, pulse duration, pulse energy, numerical aperture of the focusing lens, and the translation speed used to form the weld.

References

1. Du D, Liu X, Korn G, Squier J, Mourou G. Laser-Induced Breakdown by Impact Ionization in Sio2 with Pulse Widths from 7 Ns to 150 Fs. Appl Phys Lett 1994; 64(23):3071-3073.
2. Glezer EN, Mazur E. Ultrafast-laser driven micro-explosions in transparent materials. Appl Phys Lett 1997; 71(7):882-884.
3. Schaffer CB, Brodeur A, Garcia JF, Mazur E. Micromachining bulk glass by use of femtosecond laser pulses with nanojoule energy. Opt Lett 2001; 26(2):93-95.
4. Gattass RR, Mazur E. Femtosecond laser micromachining in transparent materials. Nat Photonics 2008; 2(4):219-225.
5. Schaffer CB, Garcia JF, Mazur E. Bulk heating of transparent materials using a high-repetition-rate femtosecond laser. Appl Phys a-Mater 2003; 76(3):351-354.
6. Schaffer CB, Brodeur A, Mazur E. Laser-induced breakdown and damage in bulk transparent materials induced by tightly focused femtosecond laser pulses. Meas Sci Technol 2001; 12(11):1784-1794.
7. Davis KM, Miura K, Sugimoto N, Hirao K. Writing waveguides in glass with a femtosecond laser. Opt Lett 1996; 21(21):1729-1731.
8. Bovatsek J, Arai A, Schaffer CB. Three-dimensional micromachining inside transparent materials using femtosecond laser pulses:
   new applications. CLEO/QELS and PhAST Technical Digest 2006; CThEE6:1-2.
9. Chichkov BN, Momma C, Nolte S, vonAlvensleben F, Tunnermann A. Femtosecond, picosecond and nanosecond laser ablation of solids. Appl Phys a-Mater 1996; 63(2):109-115.

10. Liu X, Du D, Mourou G. Laser ablation and micromachining with ultrashort laser pulses. Ieee J Quantum Elect 1997; 33(10):1706-1716.
11. Tamaki T, Watanabe W, Nishii J, Itoh K. Welding of transparent materials using femtosecond laser pulses. Jpn J Appl Phys 2 2005; 44(20-23):L687-L689.
12. Tamaki T, Watanabe W, Itoh K. Laser micro-welding of transparent materials by a localized heat accumulation effect using a femtosecond fiber laser at 1558 nm. Opt Express 2006; 14(22):10460-10468.
13. Richter S, Doring S, Tunnermann A, Nolte S. Bonding of glass with femtosecond laser pulses at high repetition rates. Appl Phys a-Mater 2011; 103(2):257-261.
14. Cvecek K, Miyamoto I, Strauss J, Wolf M, Frick T, Schmidt M. Sample preparation method for glass welding by ultrashort laser pulses yields higher seam strength. Appl Optics 2011; 50(13):1941-1944.
15. Whitesides GM. The origins and the future of microfluidics. Nature 2006; 442(7101):368-373.
16. Xia YN, Whitesides GM. Soft lithography. Annu Rev Mater Sci 1998; 28:153-184.
17. Kim TN, Campbell K, Groisman A, Kleinfeld D, Schaffer CB. Femtosecond laser-drilled capillary integrated into a microfluidic device. Appl Phys Lett 2005; 86(20):-.
18. Li Y, Itoh K, Watanabe W, Yamada K, Kuroda D, Nishii J, Jiang YY. Three-dimensional hole drilling of silica glass from the rear surface with femtosecond laser pulses. Opt Lett 2001; 26(23):1912-1914.
19. Marcinkevicius A, Juodkazis S, Watanabe M, Miwa M, Matsuo S, Misawa H, Nishii J. Femtosecond laser-assisted three-dimensional

microfabrication in silica. Opt Lett 2001; 26(5):277-279.

20. Hwang DJ, Choi TY, Grigoropoulos CP. Liquid-assisted femtosecond laser drilling of straight and three-dimensional microchannels in glass. Appl Phys a-Mater 2004; 79(3):605-612.
21. Giridhar MS, Seong K, Schulzgen A, Khulbe P, Peyghambarian N, Mansuripur M. Femtosecond pulsed laser micromachining of glass substrates with application to microfluidic devices. Appl Optics 2004; 43(23):4584-4589.
22. Schaffer CB, Nishimura N, Glezer EN, Kim AMT, Mazur E. Dynamics of femtosecond laser-induced breakdown in water from femtoseconds to microseconds. Opt Express 2002; 10(3):196-203.
23. Shimizu M, Sakakura M, Ohnishi M, Shimotsuma Y, Nakaya T, Miura K, Hirao K. Mechanism of heat-modification inside a glass after irradiation with high-repetition rate femtosecond laser pulses. J Appl Phys 2010; 108(7):073533-1-10.
24. Gardon R, Narayana.Os. Stress and Volume Relaxation in Annealing Flat Glass. J Am Ceram Soc 1970; 53(7):380-385.
25. Watanabe W, Onda S, Tamaki T, Itoh K. Direct joining of glass substrates by 1 kHz femtosecond laser pulses. Appl Phys B-Lasers O 2007; 87(1):85-89.

Chapter 9

Grade K-12 module: Fluorescence and collateral transport

One of the activities I enjoyed most during my Ph.D. was working with Jackie and her students from Eagle Hill Middle School, a suburb of Syracuse, NY. For some reason, they always seemed to notice when I would wear new clothes, glasses, or shoes. But I digress…Jackie was awesome, the students were wonderful, and I had a blast helping them with their labs and introducing them to aspects of my research. This chapter presents an activity that Jackie, Chris, and I developed, that is part of a larger curriculum. The specific goal of this activity was to introduce fluorescence and collateral transport to the students. To bring cohesiveness between the two subjects, we had the students use a maple leaf to study what happens to transport when collateral pathways are and are not present after an injury. We then translated this idea over to the human cerebral vasculature and discussed some our research that was being conducted in our lab. The writing style in this chapter diverges from the rest of the chapters as it is meant to help motivate and guide middle school teachers to replicate this activity in their classroom.

9.1 Introduction

Most middle and high school students understand that blood flow to the brain is crucial for normal function as it supplies nutrients and removes wastes from the tissue. A disruption to this system, such as a stroke (i.e. when a vessel becomes blocked or ruptures), can lead to severe brain disorders. However, it turns out that certain parts of the brain vasculature are designed to help cope with *small* vessel injuries (small strokes) in order to help maintain normal blood flow. Small strokes differ from large strokes in that when they

occur, the person exhibits no immediate neurological deficits. In other words, the person is asymptomatic. In contrast, when a large stroke occurs, the person will usually show clinical symptoms, such as motor deficiencies, paralysis, and headache. While most people are familiar with the effects of large strokes, small strokes are actually fives times more prevalent [1]

Surface arterial vessels, responsible for delivering blood to the brain, form a net-like system, or redundant loops on the brain surface (Figure 1A). If a vessel becomes blocked (ischemic stroke), this loopy architecture helps maintain blood flow (Figure 1B), and therefore, minimizes the pathological effects following a vascular injury [2]. Like the human vasculature, leaves possess a network of veins that allows for transportation of nutrients and removal of waste products. While there may be multiple large veins stemming across a leaf, closer examination reveal that, in most leaves, a network of much smaller veins exists that form loops and connections between the large veins. Similar to the human system, these collateral loops help maintain nutrient transport should the leaf sustain an injury produced by, for instance, a leaf-eating insect.

We present an inquiry-based activity that was recently taught to a seventh-grade class. In this activity, students will use optical techniques to investigate transport in a leaf during "healthy" conditions and after it suffers an injury or a small "stroke." To initiate this activity, students will first learn about fluorescence, a powerful technique widely used in the scientific field. If a fluorophore absorbs a photon at the appropriate wavelength, the molecule can be excited from its ground state to a high-energy state. At this unstable state, the molecule will relax to its ground state by losing energy in the form of an emitted photon at a wavelength *longer* than the excitation light. Therefore, we

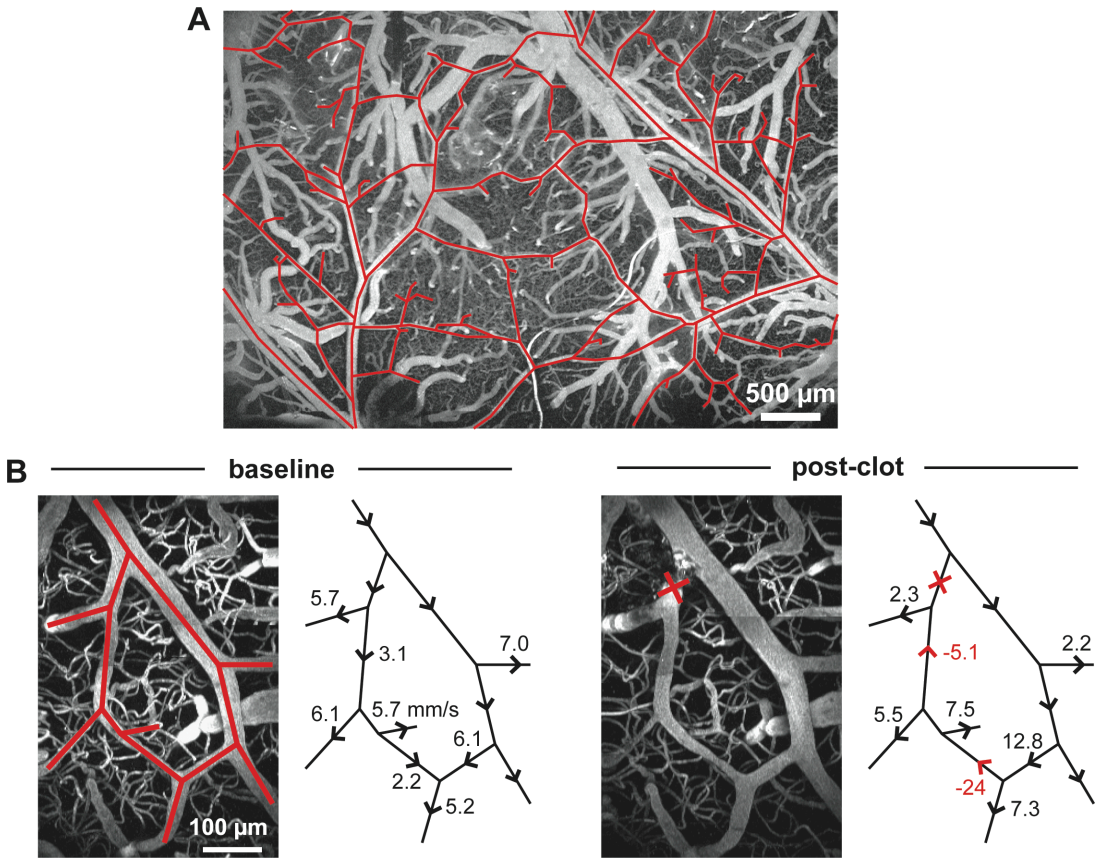
A
500 µm
B
baseline
post-clot
100 µm
5.7
3.1
7.0
6.1
5.7 mm/s
6.1
2.2
5.2
2.3
-5.1
2.2
5.5
7.5
12.8
-24
7.3

Figure 9.1

Figure 9.1 Loops in surface arterial network provide collateral flow. A) Fluorescence image of the brain vasculature in a live, anesthetized rat. Surface arterioles (outlined in red) form a net-like system on the brain surface. **B)** Case study highlighting the importance of vascular loops following a vessel occlusion. For baseline and post-clot examples, the left panels are magnified fluorescence images of the surface vasculature, with an arterial network outlined. Right panels show the network schematics with blood flow speeds in the vessels of interest, with arrows indicating direction of blood flow. Note that after optochemically inducing a clot (red X under post-clot), blood flow does not stop, but is maintained through the reversal of flow in two vessels (red arrows and values). These redundant loops help support collateral flow and minimize the pathological effects associated with a blocked vessel [2].

can briefly describe fluorescence as the emission of light from a substance that has absorbed light of a different color (Nikon, Olympus, and Zeiss are microscope vendors that provide excellent fluorescence tutorials on their websites). Using this technique, students will use the leaf's veins as a model of the arterial network on the brain surface. By visualizing its "vasculature" they will observe how collateral loops help maintain transport after an injury. By conducting these experiments, students will strengthen their understanding of scientific inquiry, including further development of their ability to generate and test hypotheses., because the students are exposed to a widely used imaging technique, the lessons provide a perfect segue into research that is currently being conducted in the scientific field.

9.2 Teacher preparation

Most chemicals for this activity will need to be purchased prior to the activity. A list of materials and vendors, as well as concentrations for all solutions can be found in Table 1. We recommend making large volumes (~50ml) of Fluorescein and Rhodamine B, from which teachers can place ~1 ml aliquots into microcentrifuge tubes. For Nile Red, teachers should add a droplet of the stock solution (Nile Red in acetone) to the ~1 ml aliquots of vegetable oil. The solutions should last for a very long time as long as they are stored in a dark place. Many of the solutions require a small amount of solute. If teachers do not have the appropriate measuring equipment, solution volumes can be scaled up. Because Nile Red is a bit more complicated to prepare, Fluorescein and Rhodamine B will be adequate for both lessons. A reference for the activities can be found at: *climb.bme.cornell.edu/invisible.php*.

Table 9.1 List of materials

Lesson 1	Lesson 2
• Fluorescein dye* (3 mg in 50 ml of H_20) • Rhodamine B dye* (1 mg in 50 ml of H_20) • Nile Red dye* i. 500 µg of Nile Red in 1 ml of acetone (stock), mix well ii. place 30 µl of stock into 1 ml of vegetable oil, shake • LED lights* (red, orange, yellow, green, blue) • microcentrifuge tubes*	• Rhodamine B dye • Maple leaves • Yellow cutoff filter* • Green filter* • Green LED • One-hole puncher

*These are items most likely need to be purchased. Below is listing of vendors and item numbers.
Fluorescein: *Sigma-Aldrich*, item number: 46955-100G-F
Rhodamine B: *Sigmal-Aldrich*, item number: R6626-25G
Nile Red: *Sigmal-Aldrich*, item number: N3013-100MG
Yellow longpass filter: *Thorlabs*, item number: FGL90S (allows light wavelengths above 590 nm to pass)
Green shortpass filter: *Thorlabs*, item number: FES0550 (allows light wavelengths up to 550 nm to pass)
Microcentrifuge tubes: *Fisher Scientific*, item number: 02-682-558
LED lights: LED arrays can be purchased online. If you are interested in building your own circuits go to ***climb.cornell.edu/insivible.php.*** A link "Seeing the invisible.pdf" will provide instructions.

9.3 Lessons

We split this activity into two separate lessons, with students working in groups of three or four. In the first experiment, fluorescence was introduced to the students (~30 minutes). In the second experiment, they apply fluorescence techniques to help visualize the leaf's transport network and understand the significance of collateral loops (~1 hour).

9.3.1 Fluorescence

For the first part of this lesson, we recommend teachers briefly discuss the protocol for making the dyes. Each group should receive a set of microcentrifuge tubes containing each dye, including a tube containing water to serve as a control, and set of LEDs. Each LED should be place far enough apart such that the excitation paths do not overlap. When students are ready, tubes should be placed a couple of inches away from the light source (Figure 2). When we implemented this activity, the students were simply handed the fluorescent dyes and the LED lights, with no instructions. They naturally turned on the all LEDs and moved the samples in front of them to see what would happen. "Cool" was the most commonly used word to describe their observations. After several minutes, the students realized that certain dyes "turned" to different color when placed in front of specific LEDs. At this point we had the students stop what they were doing in order to discuss their observations and give a short (~5 min) lecture on fluorescence. After this, we asked the students to make a chart (Table 2) and record the emission color if the dye was fluorescent.

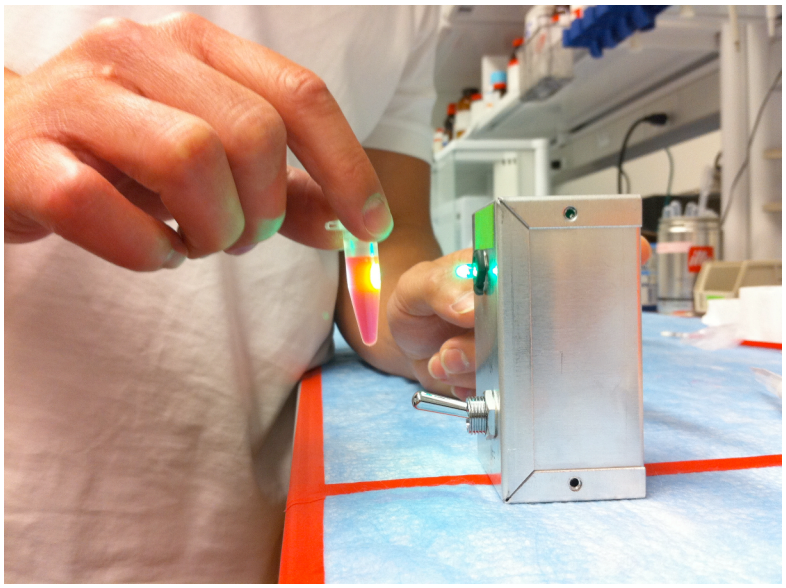

Figure 9.2 Setup for fluorescence experiment. When testing different combinations of dyes and illumination light, students should place the tubes a couple inches away from the LED. In this example, Rhodamine B fluoresces yellow when illuminated with green light.

Table 9.2 Color of emitted light for each LED color

		Color of excitation light				
		Red	Orange	Yellow	Green	Blue
Sample	Rhodamine B	DNF	DNF	DNF	yellow	DNF
	Fluorescein	DNF	DNF	DNF	DNF	green
	Nile Red	DNF	DNF	DNF	yellow	yellow - orange
	Water (control)	DNF	DNF	DNF	DNF	DNF

DNF = does not fluorescence

9.3.2 Collateral transport in a leaf

Since the students are using leaves to model the cerebral vasculature, we suggest some discussion about the role of blood flow to the brain, which makes this activity a perfect supplement to a module on the cardiovascular system. We also discussed pathologic consequences of strokes, which segued into some of the biomedical research that our lab is conducting. While this is not necessary, it is crucial that the idea of redundant networks be introduced. Schaffer *et al.* is a open access article that will serve as a great resource for this activity [2].

To start this activity, teachers will need to obtain quite a number of maples leaves, depending on the number of groups. Each group will need at least three leaves, one for each condition (control, normal, and injury), with each stem cut at the halfway point between the base of the leaf and the end of the stem. To "injure" the leaf, use a hole punch to take out a small portion of the leaf. We suggest doing this towards the base of the leaf, over one of the major veins (see injury in Figure 4). Place the stems for both normal and injured leaves into the Rhodamine B solution overnight, prior to the day of the experiment.

When everything is ready, darken the room as much as possible and have the students arrange the optical setup shown in Figure 3A. The circular green filter should be placed above the green LED. This helps block any remnants of yellow light coming from the green light, so as to not confuse this yellow light from the yellow fluorescent light emitted by Rhodamine B. When imaging the leaf, students should look through the filter (red glass). First, the students should investigate the control leaf that did not take up Rhodamine B. Unfortunately, nothing exciting will happen because there is no dye in the

veins. However, the point of this leaf is to emphasize the concept of control experiments during scientific investigations. After testing the control leaf, they should switch to the normal leaf and repeat the imaging process. The students should record observations and even make drawings of what they see. After this, we suggest the teacher ask the students what happens to the transport of nutrients when the leaf gets injured. We had the students draw out their hypothesis. The two most popular hypotheses were: (1) transport of the dye would stop at the injury or (2) transport of the dye would travel around the injury. The student then proceeded to image the injured leaves. Again, the students should record their observations and answer questions about the role of redundancies in transport networks.

We would like to make a note of some minor issues we experienced. We placed the stems in the dye on the day of the experiments, and found that about half the leaves took up the dye. Therefore, we recommend submerging the stems for both normal and injured leaves overnight, and use more leaves than needed.

9.4 Expected results and discussion

For lesson one the emission colors for each dye and illumination light is summarized in Table 2. In lesson two, the veins in the control leaf should not fluoresce since stems were not submerged in Rhodamine B (Figure 3B). As expected, normal leaves fluoresced, with large veins easily noticeable. Students will have to look closely to see the fluorescence from the smaller, collateral veins (Figure 3C). Because of these collateral loops, the dye should be able to diffuse around the injury and label the downstream veins. Therefore, students should see fluorescence past the injury.

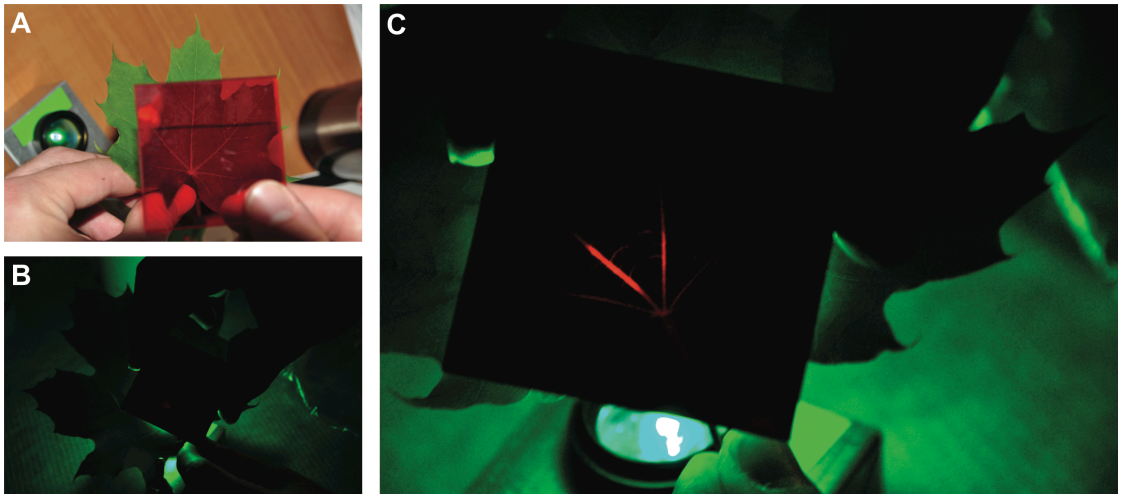

Figure 9.3 Optical setup for leaf experiment. A) To make the leaf's veins fluoresce, the green filter needs to be placed above the LED, with the leaf placed a few inches above filter. This will allow the light to illuminate a large portion of the leaf's vein network. The last component needed is the yellow filter, which allows only the fluorescent yellow light to pass through. **B)** Illumination of a leaf, in which its stem was not placed in the Rhodamine B dye. Because of this, the veins did not fluoresce. **C)** Illumination of a leaf that took up Rhodamine B dye. Note two large fluorescent veins. While it may be difficult to see, there are smaller fluorescent veins, which form a connection between the two large veins.

Collateral pathways play a significant role in maintaining normal transport after an injury. For transport networks that do no possess such architectures, downstream areas are greatly affected. For instance, the ginkgo leaf has many veins running across the leaf, but connections between them do not exist. Therefore, if a leaf-eating bug ate a small section, downstream areas past the injury will not receive nutrients and eventually die (teachers can use Figure 4 as a discussion question to gauge the students' understanding of the significance of collateral pathways). In rodent models of small stroke, the vascular topology, or the architectural makeup, plays a large role in how blood flow changes following a small stroke. Our lab has conducted a number of studies investigating the effects of small stroke [2,3,4], and serve as a great resource if the teacher wishes to expand on this activity

9.5 Safety concerns

There are a several safety issues that should be addressed. The Hazardous Materials Identification System has given Flourescein and Rhodamine B a health hazard of two (out of four), which states, "Temporary or minor injury may occur." The microcentrifuge tubes listed in Table 1 have a screw cap and as a further precaution, teachers can place a couple drops of superglue on the threads before screwing the cap on to minimize potential exposure. The flammability and reactivity hazard for both chemicals is zero. Nile Red has a zero hazard rating for health, flammability, and reactivity. Acetone has a health hazard, flammability, and reactivity rating of two, three, and zero respectively. Teachers should always wear gloves when working with these chemicals.

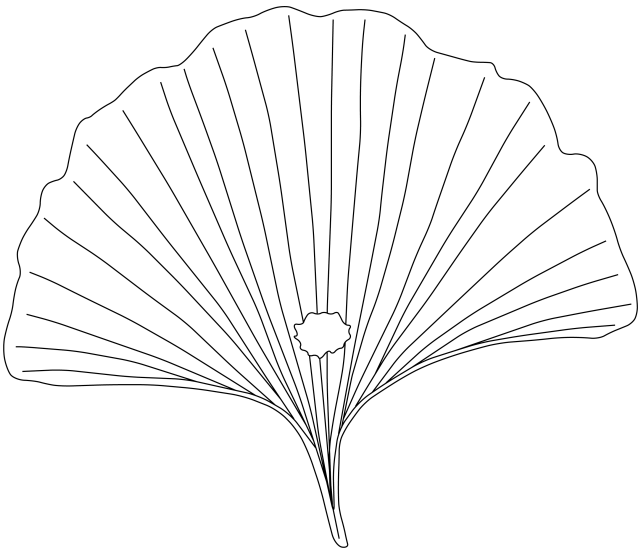

Figure 9.4 Extension activity using the gingko leaf. This is a simple cartoon of a ginko leaf and it main purpose is to provide contrast, in regards to the network architecture, to the maple leaf. Ginko leaves do not have collateral pathways that connect the large veins. One way to really test the students' understanding the activity is ask them what happens if a bug feasts on a gingo leaf. Can nutrients be transported downstream of the injury like the maple

9.6 Extension activities

Fluorescence imaging is commonly used to visualize specific structures inside of cells. In order to do this, fluorescently-tagged antibodies with specific chemical affinities are incubated with cells, allowing them to bind to the structure of interest. The cells are then illuminated with the appropriate light exciting the fluorophores, providing the location or quantity of the structures of interest. This quick activity uses a 15 ml centrifuge tube (search "15 ml centrifuge tubes" on Amazon.com), as a cell, water as its cytoplasm, and oil droplets as its organelles. One milliliter of oil is added to each tube containing ~5 ml of water. A droplet of the Nile Red stock solution is added, and the tube is then sealed. From the previous experiments, the students should recall two things: (1) what color light makes Nile Red fluoresce and (2) Nile Red dissolves only in lipid-based solvents. After rocking the tube back and forth, the students should illuminate the tube with the appropriate light and observe that only the oil beads fluoresce. While the tube is a crude model of the cell, the goal of this experiment is to highlight the powerfulness of fluorescence imaging, as it offers a colorful and bright window into biology.

9.8 Conclusions

This activity was designed to be hands-on and extremely interactive, and as a result the students really enjoyed it. Not only were the lessons inquiry-based, but in completing the activities, the students were able to learn about research techniques and used them to answer a biologically and clinically relevant question about network transport following an injury, such as a small stroke. The combination of lights, and dyes, injuring leaves, and cerebral vascular diseases should get students excited about the activity.

References

1. Vermeer SE, Koudstaal PJ, Oudkerk M, Hofman A, Breteler MM. Prevalence and risk factors of silent brain infarcts in the population-based Rotterdam Scan Study. Stroke 2002; 33(1):21-25.
2. Schaffer CB, Friedman B, Nishimura N, Schroeder LF, Tsai PS, Ebner FF, Lyden PD, Kleinfeld D. Two-photon imaging of cortical surface microvessels reveals a robust redistribution in blood flow after vascular occlusion. Plos Biol 2006; 4(2):258-270.
3. Nishimura N, Schaffer CB, Friedman B, Lyden PD, Kleinfeld D. Penetrating arterioles are a bottleneck in the perfusion of neocortex. Proc Natl Acad Sci U S A 2007; 104(1):365-370.
4. Nguyen J, Nishimura N, Fetcho RN, Iadecola C, Schaffer CB. Occlusion of cortical ascending venules causes blood flow decreases, reversals in flow direction, and vessel dilation in upstream capillaries. *Journal of Cerebral Blood Flow and Metabolism*, 2011.

Chapter 10
Conclusions and the future…

Nonlinear microscopies and femtosecond laser ablation are well suited for *in vivo* investigations of the brain, and its use in the scientific community is continuing to grow. The ability to look deep inside the brain and alter its normal state will provide many answers, but will also spawn many more questions. This thesis showcased the application of nonlinear optical techniques and answered several questions, but many still remain open.

The stroke investigation provided an in-depth analysis of vessel-by-vessel changes after a venule occlusion. The decrease in blood flow in the upstream capillaries was not unexpected, as previous studies have shown more regional changes associated with the microcirculation. Perhaps the more interesting result was how important the vascular topology is in determining the impact of blood flow following a vessel injury. The ratio between penetrating arterioles and ascending venules appeared to dictate the blood flow impact, but this would allude to the idea that the severity of a small stroke is simply dependent on the number of inlets and outlets. Further *in vivo* studies and computational models will hopefully develop a more complete story on the importance of the vascular architecture.

Characterizing the tissue pathology associated with venule strokes would have significantly strengthened the study. One method would be to utilize fluorescent probes that are two-photon excitable. For instance, David Boas and company has recently developed a two-photon excitable oxygenation probe. Thus changes in oxygenation in vessels surrounding the clot can be quantified. *In vivo* labeling of neural bodies that provide functional information can be used to study any detriments after the stroke. More

classical techniques such as immunohistology provide some technical issues, as the magic slices have proven difficult to find. However, it seems the lab is becoming more proficient with histological analyses, and it would only seem natural to study the long effect of small stroke not just in venules, but other vessels throughout the cortical vascular hierarchy. Chronic studies would contribute greatly to our understanding of the effects these venule strokes. For instance, one of the subtler, but interesting, results from the acute investigation was the presence of flow reversal. It would be interesting to study the pathological progression of endothelial dysfunction *in vivo*, as previous studies have demonstrated these cells are sensitive to changes in shear stress directionality, and magnitude. Furthermore, the development of transgenic mice will enable studies that investigate multiple responses (dendrites, microglia, αβ plaques) following not just venule occlusions, but other cerebral insults.

The ability to target sub-surface structures in the bulk of brain tissue provides a unique tool to conduct experiments with a backwards-engineering approach. For instance, the lab has discussed targeting and ablating individual pyramidal neurons in YFP mice, and monitor the changes in dendritic processes and nearby cells. Targeting other single cells such as smooth muscle cells or astrocytes will provided functional insights. This technique provides the unique ability to perform very high precision and localized targeted ablation. However, translating this capability enables transections in brain as well, essentially producing a laser scalpel. In our study in which we were able to acutely stop seizure propagation, we produced cuts between layer II and IV. Further experiments should investigate the efficacy stopping seizure propagation, or initiation, by producing cuts in specific layers, in addition to

testing different cut geometries. Other studies of interest would be to investigate seizure propagation dynamics by imaging the activity of fluorescently labeled neural bodies, and how these dynamics change following cuts produced with femtosecond laser pulses. In a similar strategy, this cutting technique can be applied to the study of neurovascular and metabolic during pre-ictal and ictal phases. One interesting result from the study was the observation of pre-ictal vasoconstriction in surface arterioles in regions surrounding the seizure focus, which also showed decreases in metabolic activity. Similar studies that investigate the same responses, but with cuts that separate the focus and surround, would shed light on the interplay between the two regions.

In a study that diverged from the biological field, we used femtosecond laser pulses to weld two microscope glass coverslips together. From the literature, it appears that one of the main goals is to produce stronger welds, or joint, strengths. An early study annealed welded glass samples to relieve much of the trapped strain surrounding the weld, and suggests that this technique should help in obtaining higher weld strengths.

Nonlinear optical techniques enable the extremely novel studies as it provides the ability to see deep within biological structures and deposit energy in bulk media. One primary advantage of using nonlinear imaging techniques for *in vivo* studies is the ability to monitor dynamic changes real time, over an extended period of time. This capability has revolutionized the biological field, and will continue to do so as new laser sources, transgenic mice, and fluorophores are developed.